

# UNIVERSITÀ DEGLI STUDI DI PADOVA

Dipartimento di Fisica e Astronomia “Galileo Galilei”  
Master Degree in Astrophysics and Cosmology

Final dissertation

**Hydrodynamical simulations of massive stars**

**collisions**

Thesis supervisor

PD. Giuliano Iorio

Thesis co-supervisors

Prof. Michela Mapelli

PhD. Erika Korb

Candidate

Juan Manuel

Pacheco Arias

Academic Year 2022/23

**Table of contents**

<b>Introduction</b>	<b>8</b>
<b>1 Pair-instability, black holes and collisions</b>	<b>10</b>
1.1 Pair-instability mass gap . . . . .	10
1.2 Black holes in the pair-instability mass gap . . . . .	12
1.3 Stellar collisions . . . . .	15
1.4 Objective . . . . .	18
<b>2 Hydrodynamics simulations and entropy criteria</b>	<b>19</b>
2.1 PARSEC and MESA: stellar profiles . . . . .	19
2.1.1 PARSEC: the PAdova and TRieste Stellar Evolution Code . . . . .	20
2.1.2 MESA: Modules for Experiments in Stellar Astrophysics . . . . .	22
2.2 STARSMASHER: collision simulations . . . . .	26
2.2.1 SPH astrophysical hydrodynamics scheme . . . . .	26
2.2.2 STARSMASHER prescriptions . . . . .	33
2.2.3 Simulation population . . . . .	36
2.3 Entropy sorting . . . . .	48
<b>3 Results</b>	<b>50</b>
3.1 Cumulative mass profiles and bound mass . . . . .	51
3.2 Rotational evolution of the remnant . . . . .	58
3.3 Hydrodynamics Vs Entropy . . . . .	62
3.4 Recommendations and perspectives . . . . .	74
<b>4 Conclusions</b>	<b>76</b>
<b>References</b>	<b>78</b>
<b>Appendix</b>	<b>91</b>

## List of figures

1.1	<i>Initial-final mass function of non-rotating primordial stars (<math>Z = 0</math>)</i>	11
1.2	<i>Mass of the primary black hole (<math>m_1</math>) vs mass of the secondary black hole (<math>m_2</math>) of merging binary black holes</i>	13
1.3	<i>Simulated stellar collision scenario in a young stellar cluster, for the formation of a massive binary back hole merger</i>	14
1.4	<i>MESA hydrogen and helium profiles of two pre-merger stars and their merger products</i>	16
1.5	<i>SPLASH visualization of a 3D hydrodynamical collision of two massive stars</i>	17
2.1	<i>PARSEC hydrogen and helium profiles of four pre-merger stars</i>	21
2.2	<i>MESA hydrogen, helium, and carbon profiles of some of the pre-merger stars, at different evolutionary stages</i>	25
2.3	<i>Schematic view of the SPH kernel convolution</i>	28
2.4	<i>STARSMASHER relaxation simulation for the MS + 2 Myr PARSEC profile of <math>42 M_\odot</math></i>	37
2.5	<i>STARSMASHER relaxation simulation for the CHeB PARSEC profile of <math>58 M_\odot</math></i>	38
2.6	<i>STARSMASHER relaxation simulation for the ZAMS MESA profile of <math>40 M_\odot</math></i>	39
2.7	<i>STARSMASHER relaxation simulation for the TAMS MESA profile of <math>60 M_\odot</math></i>	40
2.8	<i><b>Renzo et al. (2020)</b>: STARSMASHER collision simulation between the MS and TAMS PARSEC profiles of <math>42 M_\odot</math> and <math>58 M_\odot</math> respectively</i>	41
2.9	<i><b>60 TAMS vs 40 ZAMS</b>: STARSMASHER collision simulation between the ZAMS and TAMS MESA profiles of <math>40 M_\odot</math> and <math>60 M_\odot</math> respectively</i>	42
2.10	<i><b>Half Resolution</b>: STARSMASHER collision simulation between the MS and CHeB low resolution PARSEC profiles of <math>42 M_\odot</math> and <math>58 M_\odot</math> respectively</i>	42
2.11	<i><b>+ 2 Myr</b>: STARSMASHER collision simulation between the MS + 2Myr and CHeB PARSEC profiles of <math>42 M_\odot</math> and <math>58 M_\odot</math> respectively</i>	43
2.12	<i><b><math>v_\infty = 10 \text{ km/s}</math></b>: STARSMASHER collision simulation between the MS and CHeB PARSEC profiles of <math>42 M_\odot</math> and <math>58 M_\odot</math> respectively</i>	43
2.13	<i><b><math>v_\infty = 100 \text{ km/s}</math></b>: STARSMASHER collision simulation between the MS and CHeB PARSEC profiles of <math>42 M_\odot</math> and <math>58 M_\odot</math> respectively</i>	44
2.14	<i><b><math>v_\infty = 500 \text{ km/s}</math></b>: STARSMASHER collision simulation between the MS and CHeB PARSEC profiles of <math>42 M_\odot</math> and <math>58 M_\odot</math> respectively</i>	44
2.15	<i><b><math>b = 0.1 R_\odot</math></b>: STARSMASHER collision simulation between the MS and CHeB PARSEC profiles of <math>42 M_\odot</math> and <math>58 M_\odot</math> respectively</i>	45
2.16	<i><b><math>b = 1 R_\odot</math></b>: STARSMASHER collision simulation between the MS and CHeB PARSEC profiles of <math>42 M_\odot</math> and <math>58 M_\odot</math> respectively</i>	45

2.17 <b><math>b = 3 R_\odot</math></b> : STARSMASHER collision simulation between the MS and CHeB PARSEC profiles of $42 M_\odot$ and $58 M_\odot$ respectively. . . . .	46
2.18 <b><math>b = 10 R_\odot</math></b> : STARSMASHER collision simulation between the MS and CHeB PARSEC profiles of $42 M_\odot$ and $58 M_\odot$ respectively. . . . .	46
3.1 Time evolution of the total, bound, and unbound mass profiles for the Renzo, et al. (2020), + 2 Myr and Half Resolution simulations. . . . .	52
3.2 Time evolution of the total bound, and unbound mass profiles for the $b = 0.1 R_\odot$ , $b = 1 R_\odot$ and $b = 3 R_\odot$ simulations. . . . .	53
3.3 Time evolution of the total bound, and unbound mass profiles for the $v_\infty = 10 \text{ km/s}$ , $v_\infty = 100 \text{ km/s}$ and $v_\infty = 500 \text{ km/s}$ simulations. . . . .	54
3.4 Time evolution of the unbound mass percentage for all the STARSMASHER collision simulations. . . . .	55
3.5 Expected semi-analytical mass loss in the stellar collisional scenario Vs computed mass loss by the STARSMASHER simulation scheme. . . . .	57
3.6 Construction of the coordinate system aligned with the spin axis of the remnant star, and its subsequent change to a cylindrical coordinate system. . . . .	59
3.7 Time evolution of the mean velocity components of all SPH particles involved in the collision simulations. . . . .	60
3.8 Time evolution of the standard deviation for each velocity component of all SPH particles involved in the collision simulations. . . . .	61
3.9 Comparison of impact instants between a non-radial collision ( $b = 1 R_\odot$ ) and a radial collision ( $v_\infty = 500 \text{ km/s}$ ). . . . .	62
3.10 Radial profiles of the main stellar properties for the remnant star of the Renzo, et al (2020) collision simulation. . . . .	63
3.11 Radial profiles of the main stellar properties for the remnant star of the Half Resolution collision simulation. . . . .	64
3.12 Radial profiles of the main stellar properties for the remnant star of the + 2 Myr collision simulation. . . . .	65
3.13 Radial profiles of the main stellar properties for the remnant star of the $b = 0.1 R_\odot$ collision simulation. . . . .	66
3.14 Radial profiles of the main stellar properties for the remnant star of the $b = 1 R_\odot$ collision simulation. . . . .	67
3.15 Radial profiles of the main stellar properties for the remnant star of the $b = 3 R_\odot$ collision simulation. . . . .	68
3.16 Radial profiles of the main stellar properties for the remnant star of the $v_\infty = 10 \text{ km/s}$ collision simulation. . . . .	69
3.17 Radial profiles of the main stellar properties for the remnant star of the $v_\infty = 100 \text{ km/s}$ collision simulation. . . . .	70
3.18 Radial profiles of the main stellar properties for the remnant star of the $v_\infty = 500 \text{ km/s}$ collision simulation. . . . .	71
3.19 Entropic variable profile, along the cumulative mass coordinate, of each STARSMASHER collision simulation remnant star. . . . .	73
4.1 STARSMASHER relaxation simulation for the MS PARSEC profile of $42 M_\odot$ . .	91

4.2 <i>STARSMASHER relaxation simulation for the TAMS PARSEC profile of <math>58 M_{\odot}</math>.</i>	92
4.3 <i>STARSMASHER low resolution relaxation simulation for the CHeB PARSEC profile of <math>58 M_{\odot}</math>.</i>	93

**List of tables**

2.1	<i>Description of the main parameters encoded in STARSMASHER for the single star relaxation routine.</i>	34
2.2	<i>Default values of the main parameters encoded in STARSMASHER for the single star relaxation routine.</i>	35
2.3	<i>Description of the main parameters encoded in STARSMASHER for the collisional routine.</i>	36
2.4	<i>Default values of the main parameters encoded in STARSMASHER for the collisional routine.</i>	36
3.1	<i>Final percentage of unbound mass, and predicted remnant mass, for each of the simulated STARSMASHER collisions.</i>	56
3.2	<i>Final percentage of unbound mass, and predicted remnant mass, for each of the simulated STARSMASHER collisions.</i>	74

## List of acronyms

1. Stellar evolutionary stages:

- (a) *ZAMS: Zero Age Main Sequence.*
- (b) *MS: Main Sequence.*
- (c) *TAMS: Terminal Age Main Sequence.*
- (d) *CHeB: Core Helium Burning.*
- (e) *CCB: Core Carbon Burning.*
- (f) *RSG: Red Super Giant.*
- (g) *WR: Wolf-Rayet.*

2. Stellar ends:

- (a) *CC: Core-Collapse.*
- (b) *PISN: Pair Instability SuperNova.*
- (c) *PPISN: Pulsation Pair Instability SuperNovae.*

3. Galactic objects:

- (a) *AGN: Active Galactic Nucleus.*
- (b) *NCOs: Nuclear Cluster Objects.*
- (c) *SC: Stellar Cluster.*

4. Astrophysical terms:

- (a) *CO: Carbon-Oxygen.*
- (b) *PI: Pair Instability.*
- (c) *GWs: Gravitational Waves.*
- (d) *HR: Hertzsprung-Russell.*

5. Hydrodynamical terms:

- (a) *EOS: Equation Of State.*
- (b) *MLT: Mixing Length Theory.*
- (c) *SPH: Smoothed Particle Hydrodynamics.*
- (d) *AV: Artificial Viscosity.*

## Abstract

**TITLE:** Hydrodynamical simulations of massive stars collisions

**AUTHOR:** Juan Manuel Pacheco Arias

**KEYWORDS:** Gravitational waves, Pair-instability supernovae, Massive stars, Collisions.

### DESCRIPTION:

Since the detection of gravitational waves traveling through our universe, a new field of astrophysics has opened up, and with it many hypotheses and theoretical predictions have been put to the test. This is the case of the pair-instability mass gap ( $\sim 60$  and  $\sim 120 M_{\odot}$ ). Gravitational wave signals have been detected whose primary and secondary black holes fall within the mass range where it was previously thought unthinkable that they could exist as a product of stellar evolution. Different mechanisms could explain these observations, among which the gravitational collapse of a particular type of remnant from a collision between two predecessor stars stands out. Multiple studies support this hypothesis, however, it is necessary to determine the incidence of the collision parameters on the main characteristics of the post-coalescence star, especially to corroborate that its final mass and chemical composition made it a suitable remnant to produce these special black holes. To achieve this goal, the hydrodynamical simulations of stellar collisions are a perfect tool.

In this thesis, we have analyzed a set of simulations produced with the smoothed particle hydrodynamics code STARSMASHER. This set explores different configurations of mass, radius, stellar evolution time, velocity at infinity, and impact parameter for the two colliding stars. We have been able to analyze the temporal evolution of the percentage of unbound mass for all cases, obtaining that collisions produce a range of mass loss between 9.7% and 19.3%, with the impact parameter being the most influential value in the increase of this percentage. We have also visualized that the relaxation of the final remnant occurs quite quickly after the impact as long as the collision is radial. In the case of non-radial collisions, the relaxation of the post-coalescence star is much more complex, since it is altered by successive collisions between the cores of the two primary stars. We also found that non-radial collisions are the only ones that result in a remnant with tangential rotational velocity, a fact that would favor the chemical enrichment of its constituent layers and modify its subsequent evolution.

Finally, the semi-analytical process of stellar remnant construction from the entropy sorting algorithm was applied and compared with hydrodynamical collision simulations, proving that it succeeds in reproducing the structure of post-collision stars for different configurations. In addition, for the first time in this work, a new method for the determination of the amount of mass lost after the impact from the entropic profile is proposed. This methodology can reduce the computational time needed for the exploration of the parameter space of massive star collisions, allowing a breakthrough in the quantification of this formation channel as a generator of black holes in the pair-instability mass gap.

## Introduction

The classical theory of stellar evolution predicts that stars with a mass greater than  $60 M_{\odot}$  and less than about  $120 M_{\odot}$  will end their lives without leaving any remnant. This is explained by the fact that after the creation of its CO core, the conditions inside the star are such that thermal energy is used to generate electron-positron pairs. This phenomenon drastically decreases the radiation pressure and breaks the hydrostatic equilibrium, which is followed by a rapid gravitational collapse of the star and finally a thermonuclear explosion (pulsation instability supernova). This is the reason why there are no expected black holes in the pair-instability mass gap (Heger & Woosley, 2002; Tanikawa, Susa, Yoshida, Trani, & Kinugawa, 2021). However, after the detection of gravitational waves, this paradigm is undergoing major changes. Today there is a signal recorded by the LIGO-Virgo collaboration, whose extracted parameters point to the existence of black holes of mass  $\sim 85 M_{\odot}$  and  $\sim 66 M_{\odot}$  (GW190521). In addition, there are four other candidates with at least one of their black holes within the forbidden mass range (GW190403\_051519, GW190426\_190642, GW200220\_061928, and GW200129\_114245) (Abbott et al., 2020a; Nitz et al., 2021).

There are many possible explanations for this discrepancy. The first is to recognize that the limits of the pair-instability mass gap are fuzzy since they come from results with high uncertainties in the modeling of massive star evolution (Croon, McDermott, & Sakstein, 2020). The second hypothesis considers that these black holes come from the hierarchical collision of previous black holes that fulfill the mass gap instability criterion (Mapelli, Bouffanais, Santoliquido, Arca Sedda, & Artale, 2022). Finally, there is a third way to explain this, the stellar evolution of a very particular type of star generated from the collision between two progenitor stars (Di Carlo et al., 2019). This is the path that we explore throughout the development of this thesis.

Studies have shown that, in principle, massive stars with a low-mass CO core that have a huge envelope can avoid the pair-instability zone and evolve to collapse directly into a black hole. This special type of star can be produced by the collision of two massive stars, one evolved with a low-mass CO core and a main sequence one. Simulations and dynamical analysis pointed out that this type of collision could be triggered in young massive clusters, and the expected mass of the final remnant black hole is not very different from the sum of the masses of both primary stars (Di Carlo et al., 2019). However, it is still not very clear how the various parameters involved in the collision of two massive stars can greatly modify the final characteristics of the resulting one. Some studies have analyzed the stellar evolution of the expected final star to verify that it would indeed collapse into a black hole in the prohibited mass range (Renzo, Cantiello, Metzger, & Jiang, 2020), and others have explored hydrodynamical simulation of stellar collisions but without including the specific parameters needed in this case (Glebbeek, Gaburov, Portegies Zwart, & Pols, 2013).

Some studies addressed this problem by directly simulating the collision of two primary stars that meet the necessary characteristics to generate a star that avoids the pair-instability zone. This simulation was carried out using the STARSSMASHER code with the smoothed particle hydrodynamics technique and assuming a radial collision. The results obtained showed that the remnant only lost about 12% of the sum of the initial masses and its chemical composition meets the conditions described for a direct collapse to a black hole (Ballone et al., 2023; Costa, Ballone, Mapelli, & Bressan, 2022). The objective of this thesis was to explore other types of collisions by varying the parameters involved to characterize the impact they have on the characteristics of the post-coalescing star. The results obtained indicate that non-radial collisions can increase the percentage of unbound mass after the impact by up to 6% and that remnants with a mixed chemical composition could be generated as a result of the appearance of tangential velocity. The other parameters within the collisions do not generate a greater change concerning what was analyzed in previous work.

Finally, some authors have proposed an alternative process for the construction of stellar remnants from the hydrodynamic particles that model the stars before the collision. This methodology was presented by J. C. Lombardi Jr, Warren, Rasio, Sills, and Warren (2002) and Gaburov, Lombardi Jr, and Portegies Zwart (2008), and is based on the buoyancy of the elements within a fluid according to Archimedes' principle. The idea is to generate the post-collisional star from the layered arrangement of the primary particles, increasing their entropy from the center outwards. This semi-analytic process was applied and compared, in this thesis, with the results of the complete hydrodynamic simulations, proving that it succeeds in reproducing the structure of the post-collisional stars in all cases where the evolutionary state of the parent stars is clearly differentiated. This result is in agreement with Glebbeek et al. (2013) and Ballone et al. (2023), and allows us to propose a new scenario in which the exploration of the parameter space of stellar collisions can be carried out in a much faster and more efficient way. In support of the above, a new method for the determination of the amount of mass lost after direct impact, using the entropic remnant profile, is proposed in this work.

The first chapter of this thesis presents the theoretical framework necessary to understand the tension resulting from the detection of black holes in the pair-instability mass gap. There we show how collisions between massive stars are a plausible explanation for this problem. The second chapter presents the methodology used for the study of stellar collisions through hydrodynamical simulations with the systematic variation of the parameters involved. The population of stellar profiles used in this study is also described. The operation and physical principles behind the entropy sorting algorithm are described in detail. The third chapter presents the results obtained, quantifying the incidence of the collisional parameters on the percentage of mass lost and on the rotational dynamics of the remnant star, as well as the direct comparison between what is predicted by the hydrodynamical simulations and the pseudo-analytical approach of entropy sorting. Finally, the fourth chapter describes the conclusions obtained with this methodology and lists some key aspects to be considered for future proposed works. This work is properly documented, and its analysis codes are compiled and presented in a Github repository.\*.

---

\*[https://github.com/JuanManuelPacheco/Stars\\_Collisions](https://github.com/JuanManuelPacheco/Stars_Collisions)

## 1. Pair-instability, black holes and collisions

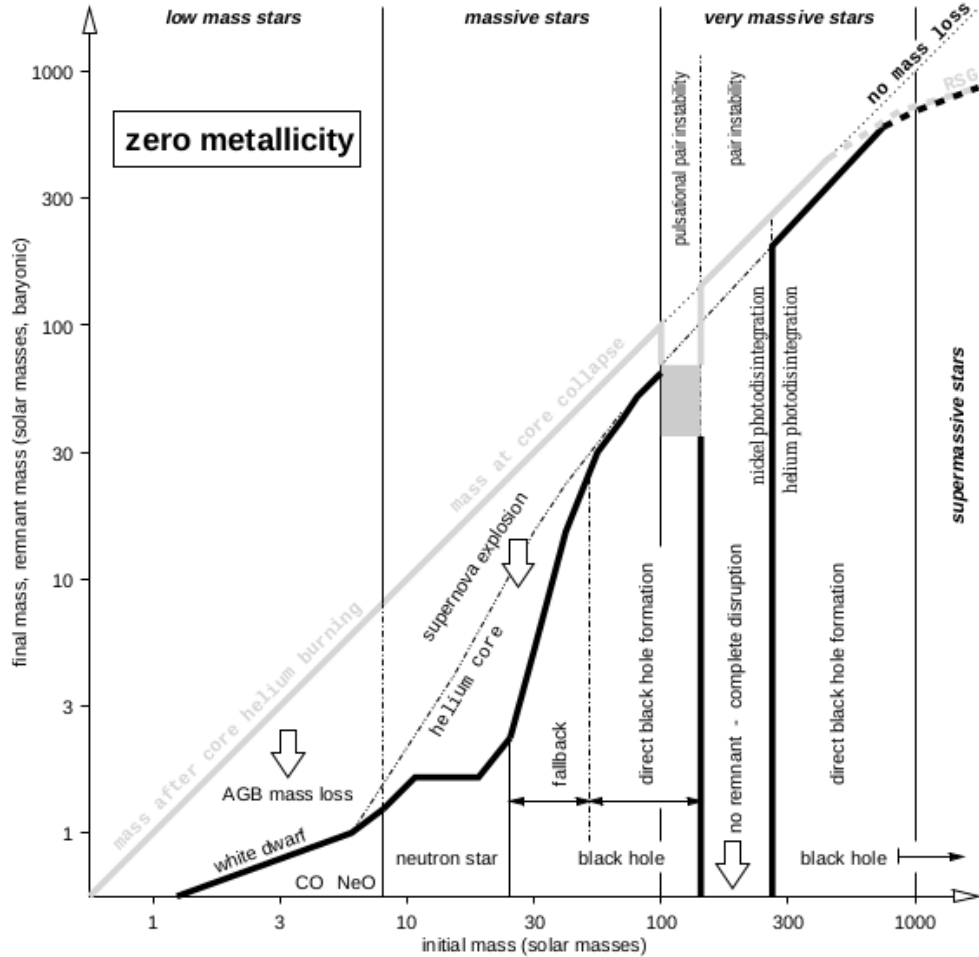
This chapter describes the origin of the problem due to the existence of black holes in the pair-instability region, followed by an exposition of the main alternative solutions discussed in the literature. For this, the traditional theory of stellar evolution for massive stars is described, deepening in why, as a result of the spontaneous generation of electron-positron pairs in their nuclei, it is not expected that stars with masses higher than  $\sim 60 M_{\odot}$  and lower than  $\sim 120 M_{\odot}$  end their lives generating compact remnant objects.

Subsequently, it is shown how the detection of gravitational waves has shaken this paradigm, revealing that there are signals resulting from the merger between two black holes that inhabit the pair-instability mass gap. Then, the different solutions proposed to alleviate this tension are analyzed as a motivation for the methodology followed in this work. These solutions explore dynamical formation channels, like the hierarchical collision of black holes or direct stellar collisions, and the complex physics that determines the limits of the pair-instability zone for massive stars.

After, the problem studied in this thesis is introduced: How do the parameters involved in the collision of two massive stars affect the final characteristics of the resulting one? Can such a remnant star collapse into a black hole of mass between  $\sim 60$  and  $\sim 120 M_{\odot}$ ? This is to relieve the tension by making use of one of the dynamic channels of formation of such pair-instability black holes, a solution that has many arguments in its favor and whose parameter exploration has never been carried out in detail. Finally, this chapter concludes with the objectives that motivate this thesis.

### 1.1 Pair-instability mass gap

Stellar evolution models predict multiple fates for massive stars ( $M > 8 M_{\odot}$ ) depending on stellar properties such as mass, metallicity, angular momentum, etc (see figure 1.1). In the case of slow-rotating metal-poor massive stars, the conditions in the core, at the end of the carbon burning phase, are expected to be perfect for the efficient production of electron-positron pairs (Fraley, 1968; Rakavy & Shaviv, 1967). This process reduces the internal radiation pressure of the star leading to a gravitational collapse that triggers a thermonuclear explosion known as a pair-instability supernova (PISN). This supernova is so violent that all stellar layers are completely disrupted after it and the star ends its life leaving no remnant (Barkat, Rakavy, & Sack, 1967; Bond, Arnett, & Carr, 1984).

**Figure 1.1***Initial-final mass function of non-rotating primordial stars ( $Z = 0$ ).*

Note. The x-axis gives the initial stellar mass. The y-axis gives both the final mass of the collapsed remnant (thick black curve) and the mass of the star when the event begins that produces that remnant (e.g., mass loss in AGB stars, supernova explosion for those stars that make a neutron star, etc.; thick gray curve). Four regimes of initial mass are distinguished: low-mass stars below  $\sim 10 M_{\odot}$  that end as white dwarfs; massive stars between  $\sim 10$  and  $\sim 100 M_{\odot}$ ; very massive stars between  $\sim 100$  and  $\sim 1000 M_{\odot}$ ; and supermassive stars (arbitrarily).\*

The pair-instability (PI) scenario affects massive stars with a carbon-oxygen (CO) core with density between  $\sim 10^2$  and  $\sim 10^6 g \cdot cm^{-3}$  and temperature over  $6 \cdot 10^8 K$  (Barkat et al., 1967; Bond et al., 1984). To reach those conditions the proper rotation of the star needs to be small to not increase the size of the nucleus, and there needs to be a lack of metals in the stellar structure to reduce the mass loss by stellar winds. This process is very sensitive to the final mass of the core and in some cases the nuclear flashes after the thermonuclear explosion are not sufficiently energetic to disrupt the entire star, leading to the pulsational pair-instability supernovae (PPISN)

\* Taken from: (Heger & Woosley, 2002)

scenario. In this case, a series of pulsations occur where the core contracts, ignites burning, expands and cools, then contracts and ignites burning again until the final disruption occurs (Leung, Nomoto, & Blinnikov, 2019; Marchant et al., 2019; Rahman, Janka, Stockinger, & Woosley, 2022; S. Woosley, 2017; S. E. Woosley, Blinnikov, & Heger, 2007).

Combining the PISN and PPISN fates, stellar evolution models are capable to predict a mass gap in the mass spectrum of black holes. The needed characteristics at the CO core to ensure disruption can be translated into lower and upper bounds for the mass of massive star remnants. Following this line of reasoning we expect an absence of black holes with masses between  $\sim 60$  and  $\sim 120 M_{\odot}$  in our Universe. This regime is known as the PI mass gap (Belczynski et al., 2016; Farmer, Renzo, de Mink, Marchant, & Justham, 2019; Heger & Woosley, 2002; Marchant & Moriya, 2020; Mehta et al., 2022; Renzo et al., 2020; Spera & Mapelli, 2017; Stevenson et al., 2019; Tanikawa et al., 2021; Vigna-Gómez, Justham, Mandel, De Mink, & Podsiadlowski, 2019).

## 1.2 Black holes in the pair-instability mass gap

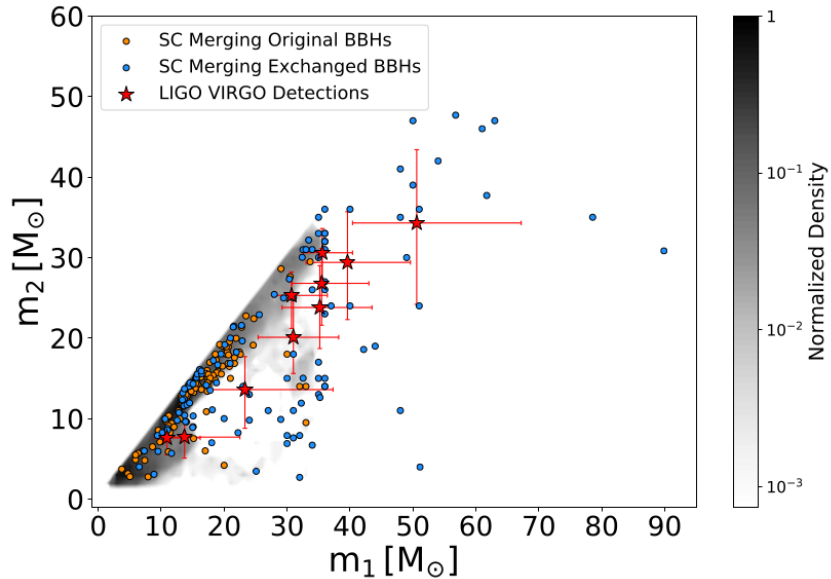
The PI mass gap is one of the stellar evolution predictions that have been tested since the detection of gravitational waves (GWs). The signals from compact object mergers, detected by the LIGO-Virgo collaboration, are challenging many theoretical frameworks in astrophysics and cosmology, lightening the understanding of our Universe. The binary black hole merger event GW190521, detected during the third observing run, is one of those examples. The parameter estimation protocol stated that the masses of the black holes responsible for that GW were  $M_1 = 85^{+21}_{-14} M_{\odot}$  for the primary and  $M_2 = 66^{+17}_{-18} M_{\odot}$  for the secondary, both of them lie inside the PI mass gap (Abbott et al., 2020a, 2020b). In addition to this event there are other fourth candidates with at least one of the merging black holes filling the PI mass gap: GW190403\_051519, GW190426\_190642, GW200220\_061928 (Abbott et al., 2021a, 2021b) and GW200129\_114245 (Nitz et al., 2021).

The unexpected detection of black holes with masses greater than  $60 M_{\odot}$  and lower than  $120 M_{\odot}$  needs an explanation to be contrasted against the traditional PI scenario. The first possibility to be explored are the uncertainties inside massive stellar evolution models, that can lead to wrong estimations for the boundaries of the PI mass gap. One of the alternatives to displace the mass limits to higher values consists of coupling, to the Standard Model, new light particles that can act as an additional source of energy loss in the cores of metal-poor massive stars, dramatically altering their evolution by suppressing the mass loss due to pulsations in the PI regime (Croon et al., 2020). A second option is to explore the uncertainties in the  $^{12}\text{C}(\alpha, \gamma)^{12}\text{O}$  reaction rate. This reaction rate determines the relative fractions of carbon and oxygen in the core at the end of helium burning, and altering it can lead to the suppression of electron–positron pairs production or the appearance of the dredge-up effect (Costa et al., 2021; Farmer, Renzo, de Mink, Fishbach, & Justham, 2020). A lot of authors have also proven that the PI mass gap is sensitive to phenomena like the presence of core overshooting and stellar wind physics (Vink, Higgins, Sander, & Sabhahit, 2021), or the evolution of stars in detached binaries, rotation, and hyper-Eddington accretion after black hole birth (S. Woosley & Heger, 2021). Finally, there exists a way to populate the PI mass gap with the remnants of super-kilonovae produced by the core collapse of rapidly rotating massive stars (Siegel et al., 2022).

Apart from arguments based on stellar properties, systems like GW190521 can be explained using dynamic interactions. This path explores the possibility of building up black holes in the PI mass gap by hierarchical mergers that can occur often in the densest regions of star clusters. This scenario can be distinguished from the stellar evolution formation channel by detecting the prints of previous mergers in the measurements of the effective spin of black hole binaries. (Antonini, Gieles, & Gualandris, 2019; Arca-Sedda et al., 2021; Coleman Miller & Hamilton, 2002; Fishbach, Holz, & Farr, 2017; Fragione, Loeb, & Rasio, 2020; Gerosa & Berti, 2017; Mapelli et al., 2022, 2021; Rizzuto et al., 2022; Rodriguez et al., 2019; Sedda, Mapelli, Benacquista, & Spera, 2021; Sedda, Mapelli, Spera, Benacquista, & Giacobbo, 2020). Direct dynamical encounters can be efficiently enhanced in the accretion disc of an active galactic nucleus (AGN). In this environment, the dynamical heating of cusp stars increases the velocity dispersion of the nuclear cluster objects (NCOs). This phenomenon, combined with the gas damping, circularizes the NCOs orbits increasing its collision cross-section in favor of the hierarchical merging hypothesis (Bartos, Kocsis, Haiman, & Márka, 2017; McKernan, Ford, Lyra, & Perets, 2012; McKernan et al., 2018; Stone, Metzger, & Haiman, 2017; Tagawa, Haiman, & Kocsis, 2020; Tagawa et al., 2021; Yang et al., 2019).

**Figure 1.2**

*Mass of the primary black hole ( $m_1$ ) vs mass of the secondary black hole ( $m_2$ ) of merging binary black holes.*



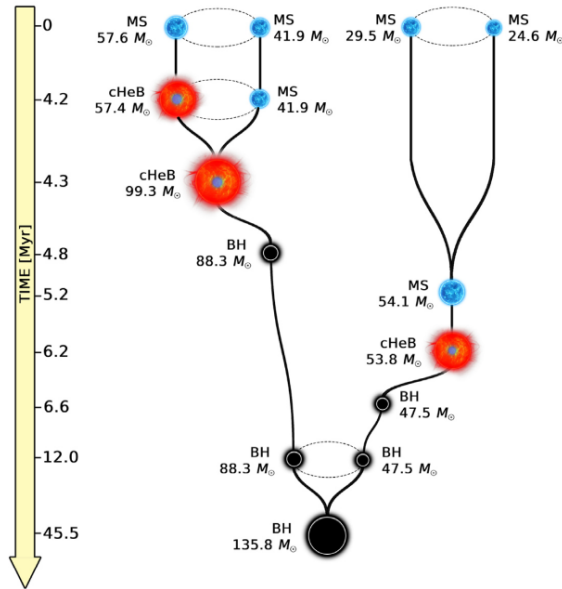
*Note.* Filled contours (with grey color map): isolated binaries; orange circles: binary black holes which form from exchanged binaries in SC simulations; blue circles: merging binary black holes which form from original binaries in SC simulations; red stars with error bars: LIGO–Virgo detections of black hole mergers.\*

\*Taken from: (Di Carlo et al., 2019)

Finally, not only direct encounters of formed black holes can populate the PI mass gap. The collision between two massive stars in a young stellar cluster (SC) can lead to the generation of a remnant star capable to skip the PI region during its evolution, directly collapsing into a black hole with a mass of more than  $60 M_{\odot}$  (see figure 1.3) (Di Carlo et al., 2019; Di Carlo, Mapelli, Bouffanais, et al., 2020; Di Carlo, Mapelli, Giacobbo, et al., 2020). Simulations that combine direct N-BODY calculations with population synthesis codes have shown that the presence of close encounters and dynamical exchanges triggers the formation and the merger of massive binary black holes in young SC (see figure 1.2). Stellar mergers are facilitated by the perturbation of a binary star, affecting its orbital properties and increasing the probability of a collision. Some massive stars even undergo runaway collisions, where they can go through multiple mergers over a short amount of time. This formation channel is strongly affected by metallicity, where metal-rich SC have a dramatic suppression on the mass of massive stars due to the presence of stellar winds (Ballone et al., 2023; Banerjee, 2022; Di Carlo et al., 2019; Di Carlo, Mapelli, Bouffanais, et al., 2020; Di Carlo, Mapelli, Giacobbo, et al., 2020; Kremer et al., 2020; Rastello et al., 2021; Rizzato et al., 2021; Spera et al., 2019).

**Figure 1.3**

*Simulated stellar collision scenario in a young stellar cluster, for the formation of a massive binary back hole merger.*



*Note.* This figure corresponds to the evolution of the most massive binary black hole merger in the set of simulations produced using the direct summation N-BODY code NBODY 6 ++ GPU coupled with the population synthesis code MOBSE described in Di Carlo, Mapelli, Giacobbo, et al. (2020). Blue stars represent main sequence stars (with label MS); red stars with a blue core represent core helium-burning stars (label cHeB); black circles represent black holes (label BH). The mass of each object is shown next to them. The time axis and the size of the objects are not to scale. The primary BH with  $M_1 = 88.3 M_{\odot}$  lies in the pair-instability mass gap. The merging Binary black holes form because of dynamical interactions.\*

\* Taken from: (Di Carlo, Mapelli, Giacobbo, et al., 2020)

### 1.3 Stellar collisions

Not all collisions of massive stars inside SC can lead to the generation of a black hole in the PI mass gap. Very special characteristics at the core of the remnant star are needed to prevent the efficient generation of electron-positron pairs. Some authors have proven that the production of an exotic star from the collision of a Core Helium Burning star (CHeB) ( $\sim 58M_{\odot}$ ) and a massive Main Sequence (MS) ( $\sim 42M_{\odot}$ ) can directly collapse into a black hole in the forbidden mass range (Ballone et al., 2023; Costa et al., 2022; Di Carlo et al., 2019; Di Carlo, Mapelli, Bouffanais, et al., 2020; Di Carlo, Mapelli, Giacobbo, et al., 2020; Renzo et al., 2020). This scenario is extremely sensible to substantial modifications of the nucleus of the remnant and the density and chemical composition of the envelope after the impact, facing several challenges.

The first challenge is to retain sufficient mass during the stellar encounter. The envelope of very massive stars is loosely bound and can be easily stripped by violent collisional environments, dramatically increasing the mass-loss rate during the merger. Radiation transport can also affect the mass budget in the case of very luminous stars (Renzo et al., 2020). The next challenge is to maintain the core mass below the PI regime. The thermodynamical properties of a stellar collision between stars at similar evolutionary stages would lead to the merger of both stellar cores (Gaburov et al., 2008; Glebbeek et al., 2013; J. C. Lombardi Jr et al., 2002). This phenomenon, combined with the rotational mixing produced by the angular momentum transference during the dynamical encounter (Maeder & Meynet, 2000), pushes the remnant core mass into the PI region.

The subsequent evolution of the post-merger star is also crucial to ensure this black hole formation channel. The large mass loss due to line-driven wind needs to be suppressed by surface magnetic fields (Belczynski et al., 2020) or prevented by a low metallicity envelope (Farrell et al., 2021). A massive remnant with high angular momentum can experience centrifugally driven mass loss (Heger, Langer, & Woosley, 2000; Langer, 1998; Zhao & Fuller, 2020), and merger products are suitable environments to produce luminous blue variable eruptions (Aghakhanloo, Murphy, Smith, & Hložek, 2017; Justham, Podsiadlowski, & Vink, 2014) and to experience eruptive mass loss (Jiang et al., 2018).

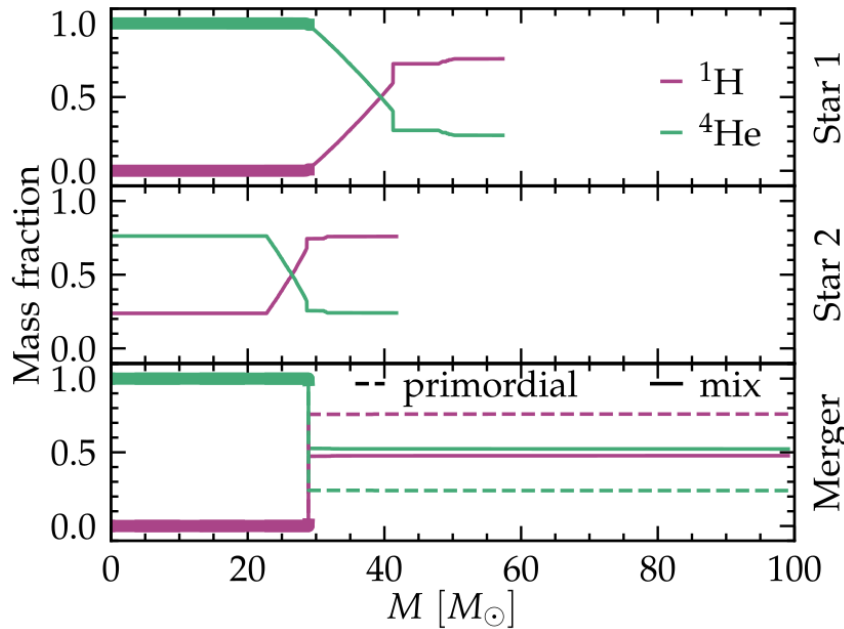
At the end of the stellar evolution, and during black hole formation, the remnant star will experience more mass loss due to neutrino emission and the emergence of unbound layers after propagating shocks (Di Carlo, Mapelli, Giacobbo, et al., 2020; Fernández, Quataert, Kashiyama, & Coughlin, 2018; Lovegrove & Woosley, 2013; Nadezhin, 1980). Finally, if all of these challenges are overcome and a black hole is formed in the PI mass gap, it needs to be dynamically coupled with a companion, merge and emit a GW capable of being detected using the LIGO-Virgo interferometers. This process is favored by the large mass of the black holes involved in this hypothesis Di Carlo et al. (2019); Di Carlo, Mapelli, Bouffanais, et al. (2020); Di Carlo, Mapelli, Giacobbo, et al. (2020); Kremer et al. (2020); Spera et al. (2019).

The stellar collision formation channel has been studied following two simulation paths. The first studies computed the stellar structures before and after the merger using the stellar evolution code MESA (Paxton et al., 2010, 2019). In this methodology the direct collision process is never simulated, instead of that the envelope of the primary star (CHeB or Terminal Age Main Sequence

(TAMS) of  $\sim 58M_{\odot}$ ) is enriched by the homogeneous addition of mass from the secondary star (MS of  $\sim 42M_{\odot}$ ), and the nucleus of the most evolved star is assumed to be the core of the remnant (see figure 1.4) (Di Carlo et al., 2019; Renzo et al., 2020). This assumption is supported by the buoyancy effect responsible for the redistribution of fluids out of equilibrium, based on the thermodynamical properties of the stellar gas involved in this type of collision (this principle and its operation are described in detail in the section 2.3) (Gaburov et al., 2008; Glebbeek et al., 2013). The subsequent evolution determined by MESA states that the exotic merger product tends to be helium-rich and spends most of its remaining lifetime within regions of instabilities in the Hertzsprung–Russell (HR) diagram. The mass loss estimations ensure that this star will retain enough mass to generate a black hole in the PI regime after core-collapse (CC), concluding that this scenario will be able to overcome some of the previously described challenges (Renzo et al., 2020). However, this methodology does not account for some key parameters like the mass loss at the time of the merger, the resulting core structure without the thermodynamic assumption, and the mass loss at CC, making it difficult to confirm the viability of this formation channel by following these models (Ballone et al., 2023; Costa et al., 2022; Renzo et al., 2020).

**Figure 1.4**

*MESA hydrogen and helium profiles of two pre-merger stars and their merger products.*



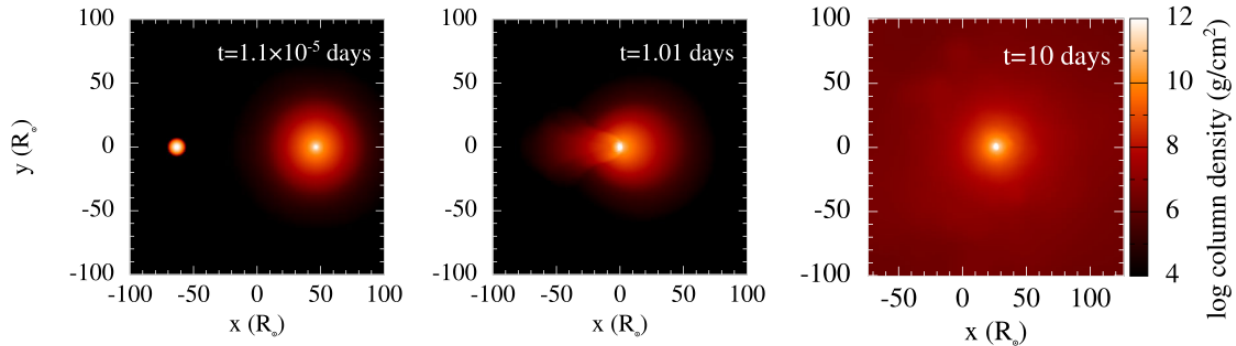
*Note.* The pre-collision stars are the top and middle panels, and the merger products are the bottom panel. In the bottom panel, solid lines indicate the envelope composition for the mixed model where both stars fully mix at merger time. The dashed lines indicate the envelope composition for the primordial model where the remnant layers are built assuming that the lowest entropy ones sink to the bottom. Both models have by construction the same core structure of the most massive star pre-merger (thicker lines). The least massive Star 2 is too young to have a well-defined helium core.\*

\* Taken from: (Renzo et al., 2020)

The only way to account for the precise mass loss at the collision, and to determine the actual stellar structure in the post-merger star, is to perform a 3D hydrodynamical simulation of the direct encounter. This is the second way to study the stellar collision scenario using simulations. The idea is to mix stellar evolutionary codes like PARSEC (Bressan et al., 2012; Costa, Girardi, Bressan, Chen, et al., 2019; Costa, Girardi, Bressan, Marigo, et al., 2019) and MESA, with smoothed-particle hydrodynamics codes suited for the simulation of star collisions, like STARSMASHER (Gaburov, Lombardi, & Zwart, 2010). Using this methodology the computation of the stellar structures before and after the collision is still performed by stellar codes, but in the middle STARSMASHER will receive the 1D profiles of the primary and secondary stars, will transform them into 3D stars that will collide following the orbital parameters of stars in young SC (see figure 1.5), and will form the remnant star for which its subsequent evolution will be computed again by stellar evolutionary codes (Ballone et al., 2023; Costa et al., 2022).

**Figure 1.5**

*SPLASH visualization of a 3D hydrodynamical collision of two massive stars.*



*Note.* Column mass density maps for one hydrodynamical simulation, at the beginning (left-hand panel), at the time of the collision (central panel), and at the end of the simulation (i.e. after 10 days of evolution; right-hand panel). Initially, the two stars are at a distance of  $110R_{\odot}$ . As the two stars move on their radial orbit, the secondary enters the much larger envelope of the primary, forming a long cometary tail, and gets disrupted when reaching the inner parts of the CHeB star, after one day of evolution. At the end of the simulation, the stellar remnant relaxes to a much larger envelope, generated by the inflation of the outer layers of the primary star.\*

The hybrid model described in the previous paragraph can lead to more precise constraints on the needed characteristics for the two massive stars involved in the formation of a black hole in the PI mass gap. Some authors found that a head-on collision can remove up to 12% of the initial mass. Hydrodynamical simulations also showed that the MS star can mix with the core of the primary star, changing the inner chemical composition of the remnant, contrary to the expected thermodynamical recombination of the gas (Ballone et al., 2023). In this specific scenario, the exotic post-collision star evolved through all the stellar burning phases until CC. Before CC, the merger product was a blue supergiant star with a total mass loss of  $\sim 1M_{\odot}$  due to stellar winds and neutrino emission (Costa et al., 2022). The final black hole mass founded by Ballone et al. (2023) and Costa et al. (2022) is  $\sim 87M_{\odot}$ , this example confirms that the collision scenario can

\* Taken from: (Ballone et al., 2023)

populate the PI regime provided that the sum of the initial mass remains within the mass gap after dynamical losses. Although hydrodynamical simulations can quantify in greater detail the effects of the collision between two massive stars, some key parameters within this scenario have not been explored yet. This is a consequence of the high computational cost of this type of simulation.

## 1.4 Objective

The goal of this master thesis is to follow the hybrid methodology, proposed by [Ballone et al. \(2023\)](#) and [Costa et al. \(2022\)](#), to explore other types of stellar collisions. The idea is to vary the evolutionary stages of both stars before the encounter and the orbital parameters of the collision, identifying the influence they have on the post-coalescing stellar structure. Finally, the parameter space of the stellar collisions formation channel is expected to be explored in more detail throughout this thesis thanks to the generation and analysis of a set of stellar profiles and hydrodynamical collisions, concluding with the necessary characteristics to populate the PI mass gap with black holes generated through the encounter of massive stars in young SC.

## 2. Hydrodynamical simulations and entropy criteria

Stellar collisions are an extremely complex process, whose time scale and spatial resolution are so small that direct observations of such events on the sky are not possible today. This means that the only possibility to explore and analyze their dynamics is by making use of computational simulations. In particular, hydrodynamical simulations of stellar collisions allow detailed three-dimensional tracking of the dynamics of the particles that make up the stars involved, which allows us to determine the final characteristics of the remnant and how they vary as the collisional parameters change.

Despite its enormous advantages, the hydrodynamical simulation process of stellar collisions has a high computational cost, a fact that complicates an efficient exploration of the parameter space for this process and limits its study. For this reason, semi-analytical approaches have emerged in the literature to reduce the cost of hydrodynamical simulations by assuming that the collision between the two stars meets a series of requirements. One of these approaches proposes to regroup the particles that make up each star as their entropy increases, managing to build the remnant star from the two initial ones without the need to make a detailed follow-up of the entire collision and thus drastically reducing the time employed.

This chapter presents the population of stellar collision simulations produced using the STARS-MASHER hydrodynamical simulation code, generated from some of the profiles obtained with PARSEC and MESA stellar evolution codes. The range of parameters explored and the reason for each of the values selected to produce the sample is also described. Finally, the entropy ordering process is explained in detail as an alternative to the hydrodynamical simulation.

### 2.1 PARSEC and MESA: stellar profiles

PARSEC and MESA are stellar evolutionary codes, that compute the evolutionary tracks for stars by solving the coupled stellar evolution equations using advanced numerical techniques. These two codes are among the most widely used by the astrophysical community and are therefore very well-tested and properly documented. Each code is different from the others, not only in the micro and macro physics implemented in their routines but also in their computational structure.

### 2.1.1 PARSEC: the PAdova and TRieste Stellar Evolution Code

#### Micro and macro-physics

PARSEC is the result of a thorough revision and update of previous codes used at the University of Padova (Bertelli, Bressan, Chiosi, Fagotto, & Nasi, 1994; Bertelli, Girardi, Marigo, & Nasi, 2008; Bertelli, Nasi, Girardi, & Marigo, 2009; Bressan, Fagotto, Bertelli, & Chiosi, 1993; Girardi, Bressan, Bertelli, & Chiosi, 2000; Marigo, Girardi, Chiosi, & Wood, 2001). Among the physical models incorporated in this code, the following stand out (Bressan et al., 2012; Costa, Girardi, Bressan, Chen, et al., 2019; Costa, Girardi, Bressan, Marigo, et al., 2019). The calculation of the pre-main sequence phase evolution. The detailed description of the absorption properties of matter in the gas using static tables of Rosseland mean opacities  $\kappa_R(\rho, T)$  in different temperature regimes:

- Low-temperature regime opacities ( $3.2 \leq \log(T/K) \leq 4.1$ ) are computed using the *ÆSOPUS* tool (Marigo & Aringer, 2009).
- High-temperature regime opacities ( $4.2 \leq \log(T/K) \leq 8.7$ ) are provided by the Opacity Project At Livermore (OPAL) team (Iglesias & Rogers, 1996).
- Middle-temperature regime opacities ( $4.0 < \log(T/K) < 4.1$ ) are produced by linear interpolation between the ones derived from OPAL and *ÆSOPUS*.

The computation of the Equation of State (EOS) by making use of the FREEEOS<sup>\*</sup> Fortran library and by the interpolation of pre-computing tables. This calculation is performed by accounting for H, He, C, N, O, Ne, Na, Mg, Al, Si, P, S, Cl, Ar, Ca, Ti, Cr, Mn, Fe, and Ni. The implementation of a nuclear network that consists of the p–p chains, the CNO tri-cycle, the Ne–Na and Mg–Al chains, and the most important  $\alpha$ -capture reactions, solving for the abundance of 30 chemical species. Energy losses by electron neutrinos are included from Munakata, Kohyama, and Itoh (1985) and Itoh and Kohyama (1983), and for plasma neutrinos by the fitting formulae provided by Haft, Raffelt, and Weiss (1993).

The complex modeling of convection is implemented following the Schwarzschild criterion, accounting for overshoot from the convective core, overshoot in the convective envelope, breathing pulses, temperature gradient in the convective region, and finally the presence of diffusive convection, where the elements in the turbulent regions are mixed by solving a system of diffusion equations coupled with the nuclear reaction rates for each chemical element (Costa, Girardi, Bressan, Marigo, et al., 2019). The insertion of rotation is coded considering the departure from spherical geometry, modification of the stellar structure equations, and the transport of angular momentum (Costa, Girardi, Bressan, Chen, et al., 2019).

#### Prescriptions and simulated catalog

In this study, we used stellar tracks generated with version v2.0 of PARSEC, in which all the aforementioned are available. As explained in chapter 1, the first step in the simulation chain of

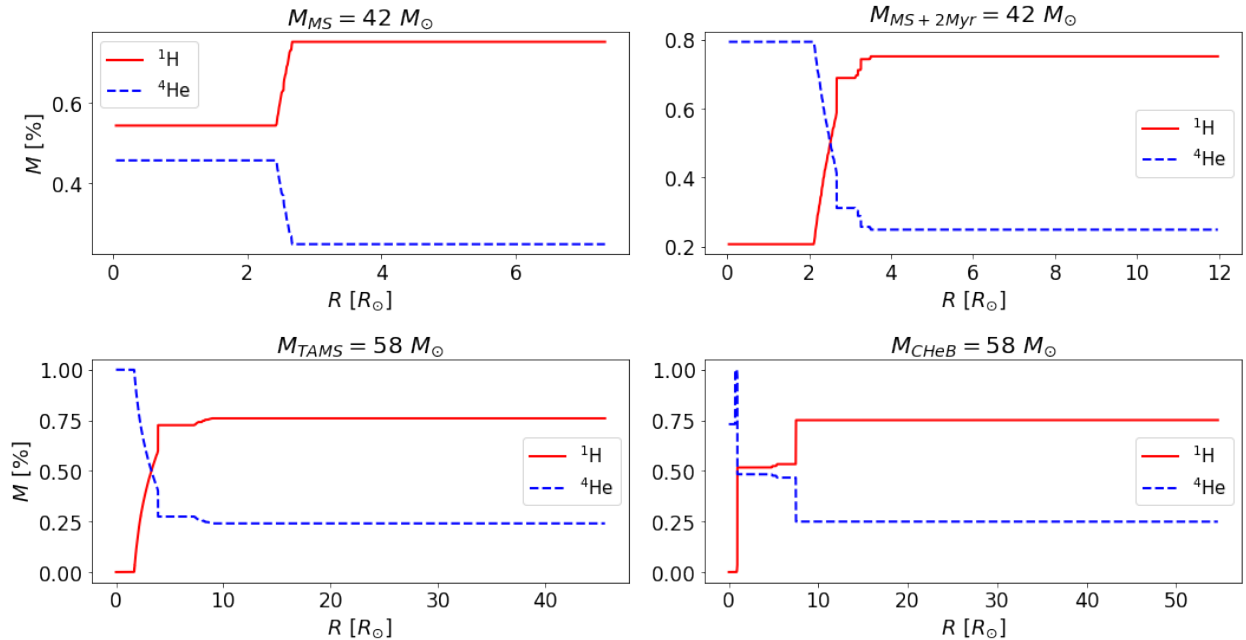
---

<sup>\*</sup> Available at: <http://freeeos.sourceforge.net/>

massive star collisions is the generation of the 1D profiles of the colliding stars using the stellar evolution codes. In our case, we generated a set of four stars with PARSEC. The first two stars have a mass of  $41.9 M_{\odot}$  ( $\sim 42 M_{\odot}$ ) and they only differ in the evolutionary stage at which we stopped the simulation. Both of them were still in the MS but the first one was stopped at an age of  $2 \text{ Myr}$  and the second was evolved  $+2 \text{ Myr}$  ( $4 \text{ Myr}$  in total). The latter two stars also have the same mass, in this case,  $57.6 M_{\odot}$  ( $\sim 58 M_{\odot}$ ), and again the difference is only the final stage, for the first one, the simulation was terminated at the TAMS, meanwhile the second one reaches the CHeB phase (see figure 2.1).

**Figure 2.1**

PARSEC hydrogen and helium profiles of four pre-merger stars.



*Note.* The  $\sim 42 M_{\odot}$  and  $\sim 58 M_{\odot}$  pre-collision stars are the top and bottom panel respectively. In the top panel, from left to right column, the profiles are at  $2 \text{ Myr}$  Main Sequence (MS) and  $4 \text{ Myr}$  Main Sequence (MS + 2 Myr). In the bottom panel, from left to right column, the profiles are at Terminal Age Main Sequence (TAMS) and Core Helium Burning (CHeB). Solid red lines indicate the mass fraction of hydrogen along the radius for each star. The dashed blue lines indicate the mass fraction of helium along the radius for each star. All models have by construction the same physics on PARSEC. The main difference between them is the core extension and composition, as well as the increase in the final radius with the increasing age, as expected from different evolutionary stages for stars of similar mass.

The prescriptions used in the code for the four stars were the same and they are fully described in Costa et al. (2021) and Costa et al. (2022). The stars were modeled as non-rotating, assuming the solar composition described in Caffau, Ludwig, Steffen, Freytag, and Bonifacio (2011), with an initial metallicity of  $Z = 0.002$  and a helium fraction of  $Y = 0.249$  (Bressan et al., 2012). The Schwarzschild criterion defined the convectively unstable borders (Strittmatter, n.d.) and the diffusion coefficients within unstable regions were computed using the mixing length theory for  $\alpha_{MLT} = 1.74$ . The overshooting region was described using the penetrative overshooting scheme presented in Maeder (1975) and Bressan, Chiosi, and Bertelli (1981) with an overshooting param-

eter  $\lambda_{ov} = 0.4$  (Costa, Girardi, Bressan, Marigo, et al., 2019). For the opacities the OPAL and  $\text{\texttt{\texttt{AESOPUS}}}$  tools were used in the high and low-temperature regimes respectively, and the conductive opacities were included following Itoh, Uchida, Sakamoto, Kohyama, and Nozawa (2008). The energy loss by electron and plasma neutrinos was accounted for using the prescriptions listed above, and two different regimes were settled for the EOS depending on the central temperature. If the condition  $\log(T/K) < 8.5$  was fulfilled, the EOS was computed using the standard procedure (interpolation of tables from FREEEOS), but if  $\log(T/K) > 8.5$  then the EOS was computed using the code presented in F. Timmes and Arnett (1999) to account for the pair creation process. The reaction rates and the Q-values, needed for the calculation of the nuclear reaction network, were taken from the JINA reaclib database (Cyburt et al., 2010). Finally, the mass-loss by stellar winds was modeled as described in Chen et al. (2015).

## 2.1.2 MESA: Modules for Experiments in Stellar Astrophysics

### Micro and macro-physics

In addition to the models produced using PARSEC, we also generated a set of 1D stellar profiles using MESA. This tool is a suite of open-source, robust, efficient, thread-safe libraries for a wide range of applications in computational stellar astrophysics (Paxton et al., 2010). Contrary to the structure of PARSEC, MESA is organized in modules that are constructed as a separate Fortran 95 library, allowing them to be used fully independently from each other and facilitating their independent development. MESA star is the module responsible for the generation and evolution of the stellar profiles solving the fully coupled structure and composition equations simultaneously, by combining many of the numerical and physics modules (Paxton et al., 2010).

The micro and macrophysics models implemented in MESA star are very wide-ranging and are in constant evolution and upgrading. They can go from the implementation of giant planet simulations, asteroseismology and the evolution of white dwarfs (Paxton et al., 2013), to the creation of modules like MESA binary, able to simulate binary systems accounting for the change of orbital angular momentum, the angular momentum loss by gravitational waves emission, the spin-orbit coupling, the magnetic braking mechanism, etc. (Paxton et al., 2015). They can model the large amplitude, self-excited, nonlinear pulsations that stars develop when they cross instability domains in the Hertzsprung-Russell (HR) diagram, using the Radial Stellar Pulsations (RSP) functionality (Paxton et al., 2019), and they can improve the implemented numerical methods by the appearance of modules like auto\_diff, that allows the automatic differentiation in MESA (Jermyn et al., 2023).

For the simulations of the stellar profiles that are interesting for this study, the physical models that stand out are the following. The calculation of the EOS is performed by the eos module using pre-processed tables of  $\rho$ - $T$ , based on the 2005 update of the OPAL EOS tables (Rogers & Nayfonov, 2002). The lower temperatures and densities are modeled using the SCVH tables (Saumon, Chabrier, & van Horn, 1995), and the overlapping region is built by ensuring a smooth transition between those two regimes. Outside the region covered by the previously described tables, especially in the high temperature and density zone proper of the electron-positron production process, the HELM (F. X. Timmes & Swesty, 2000) and PC (Potekhin, 2010) EOSs are employed. It should

be noted that in addition to this, other EOS treatments can be easily implemented in MESA, such as tables from FREEEOS, by using the `other_eos` module (Paxton et al., 2010). The generation of the opacity tables is in charge of the pre-processor `make_kap` inside the `kap` module, combining the radiative opacities and the electron conduction opacities from different approaches:

- Radiative opacities are included from Ferguson et al. (2005) for  $2.7 \leq \log(T) \leq 4.5$  and OPAL (Iglesias & Rogers, 1996) for  $3.75 \leq \log(T) \leq 8.7$ . The low-temperature opacities include the effects of molecules and grains (Paxton et al., 2010).
- Electron conduction opacities were modeled from Cassisi, Potekhin, Pietrinferni, Catelan, and Salaris (2007) in the  $-6 \leq \log(\rho) \leq 9.75$  and  $3 \leq \log(T) \leq 9$  regime. Outside this zone the Iben Jr (1975) fit to the Hubbard and Lampe (1969) electron conduction opacity is used for non-degenerate cases, and the Yakovlev and Urpin (1980) approach is used for degenerate cases (Paxton et al., 2010).

The detailed modeling of the thermonuclear and weak reactions, as part of the implementation of the nuclear network, accounts for the inclusion of more than 300 nuclear reaction rates from Caughlan and Fowler (1988) and Angulo et al. (1999) in the `rates` module. Lepton captures and  $\beta$ -decay rates for the late stages of stellar evolution are computed by the `weaklib` module, taking the tables from Fuller, Fowler, and Newman (1985), Oda, Hino, Muto, Takahara, and Sato (1994) and Langanke and Martinez-Pinedo (2000). Electron screening factors for thermonuclear reactions are included by the `screen` module using two methods: one based on Dewitt, Grabske, and Cooper (1973) and Grabske, Dewitt, Grossman, and Cooper (1973), and the second one combines Grabske et al. (1973), Alastuey and Jancovici (1978) and Itoh, Totsuji, Ichimaru, and Dewitt (1979). Energy-loss rates by neutrinos emission processes like plasmon decay, pair annihilation, bremsstrahlung, recombination, and photo-neutrinos are considered in the `neu` module by the implementation of a routine\* derived from the fitting showed in Itoh, Hayashi, Nishikawa, and Kohyama (1996). Nuclear reaction networks can be included following different paths. The `net` module routine allows computing a basic network of eight isotopes ( $^1\text{H}$ ,  $^3\text{He}$ ,  $^4\text{He}$ ,  $^{12}\text{C}$ ,  $^{14}\text{N}$ ,  $^{16}\text{O}$ ,  $^{20}\text{Ne}$  and  $^{24}\text{Mg}$ ), or extended networks accounting for hot CNO reactions,  $\alpha$ -capture chains,  $(\alpha, p)$  +  $(p, \gamma)$  reactions, and heavy-ion reactions (F. Timmes & Arnett, 1999). MESA also includes the possibility of creating a new network by listing the desired isotopes and reactions from a table of 350 reactions stored in a data file (Paxton et al., 2010). On top of that, for the case of large nuclear networks, MESA use the specialized `jina` module, based on the `netjina` package and the JINA Reaclib database (Amthor et al., 2006; Rauscher & Thielemann, 2000), combined with `weaklib` and `screen` modules.

The treatment of convection follows the implementation of the standard mixing length theory (MLT) (Cox & Giuli, 1968) in the module `m1t`. This module determines the diffusion coefficients by treating the convective mixing of elements as a diffusive process (Paxton et al., 2010). Apart from the standard model, `m1t` also includes the modified MLT proposed by Henyey, Vardya, and Bodenheimer (1965), where the convective efficiency varies with the opaqueness of the convective element, contrary to the assumptions of high optical depths and no radiative losses of the standard model (Paxton et al., 2010). The correct positioning of convective boundaries inside the simulated

---

\* [cococubed.asu.edu/code\\_pages/codes.shtml](http://cococubed.asu.edu/code_pages/codes.shtml)

star has improved thanks to the implementation of the MESA predictive mixing scheme described in Paxton et al. (2018). Hydrodynamical mixing instabilities at convective boundaries are set by the overshoot mixing diffusion coefficient computed using a parametric model (Herwig, 2000). The insertion of particle diffusion and gravitational settling is accounted for in the diffusion module, by solving Burger's equations as presented in Thoul, Bahcall, and Loeb (1993). The transport of material is computed as in Iben Jr and MacDonald (1985), and radiative levitation is neglected (Paxton et al., 2010).

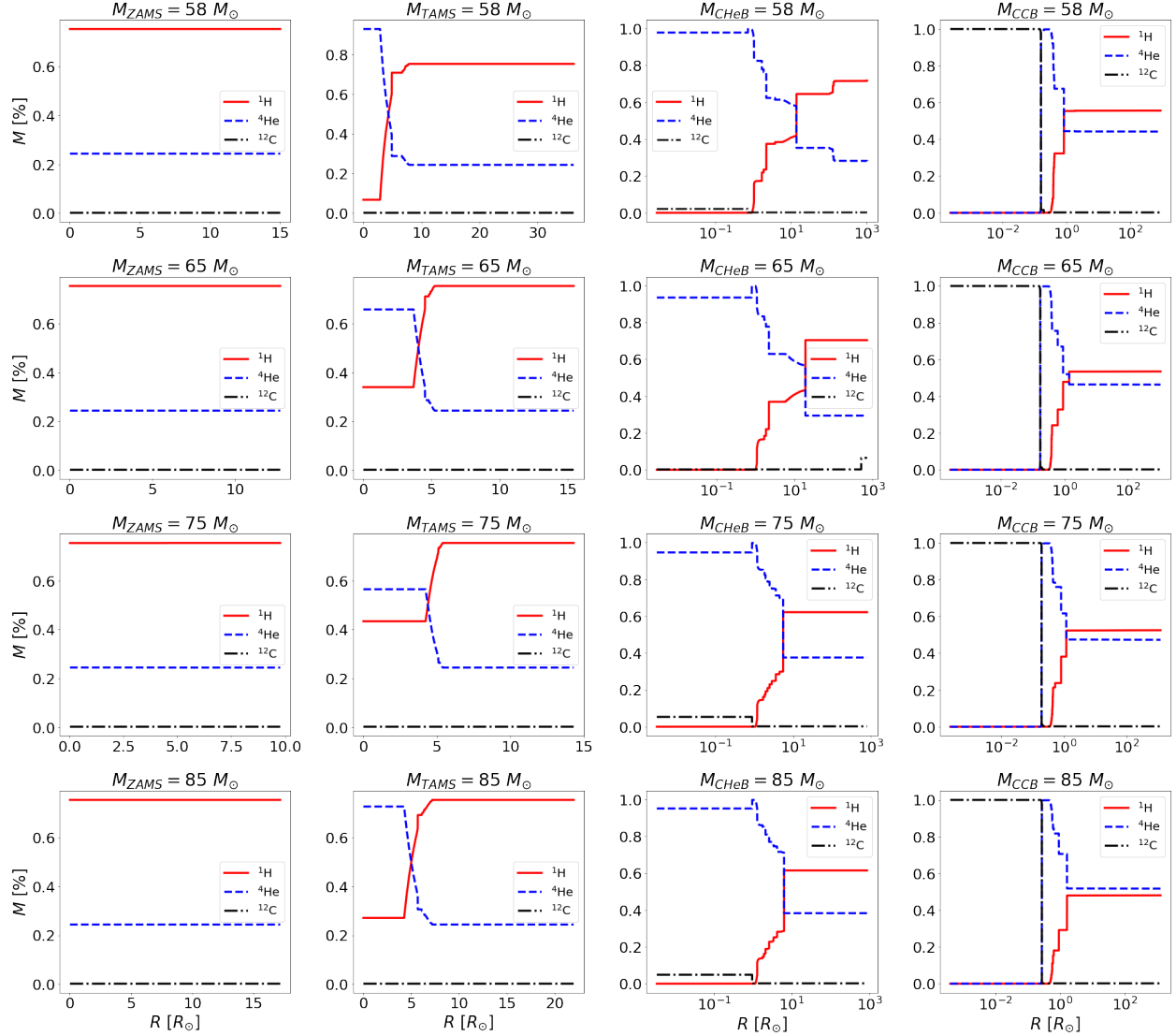
### Prescriptions and simulated catalog

For the development of this thesis, we used the MESA code version 12778, which includes all the features described above. The prescriptions for the generation of all the MESA stellar profiles analyzed in this study are based on the configurations proposed in Renzo et al. (2020) and Costa et al. (2022), two of the major references in the study of PI mass gap population via massive stellar collisions. The used EOS was a mixture between all possible tables encoded in eos (OPAL, SCVH, PTEH, HELM, and PC). The predominant radiative opacities were the ones for high-temperature (OPAL) and also some data from Ferguson et al. (2005) was used in the low-temperature scenario. The standard electron conduction opacities approach was used (Cassisi et al., 2007). For the nuclear reaction rates, there was a blend between NACRE (Angulo et al., 1999) and JINA Reaclib (Cyburt et al., 2010), including all the tables stored in the weaklib module. The screening process was taken from Chugunov, Dewitt, and Yakovlev (2007) and thermal neutrino loss rates came from the previously described routine of the neu module. The nuclear reaction network was computed using the basic  $\alpha$ -chain reaction of eight isotopes detailed in previous paragraphs.

In terms of the convection treatment, we used the Ledoux criterion to define the convective borders (Ledoux, 1947), with the diffusion coefficient  $\alpha_{MLT} = 2.0$  in the MLT framework. The artificial enhancement of the convective flux, thanks to MLT++, was also used (Paxton et al., 2015). Overshooting and thermohaline mixing were included using the schemes of Brott et al. (2011) and Farmer et al. (2016) respectively. All profiles were produced using a metallicity  $Z = 0.0002$  (Costa et al., 2022; Renzo et al., 2020). Stellar winds were included using the algorithms from Vink, de Koter, and Lamers (2001) with a correction on the solar metallicity ( $Z_\odot = 0.019$ ) recommended by Choi et al. (2016). This correction is needed to diminish the huge mass loss (up to  $5 M_\odot$ ) at the Red Super Giant (RSG) phase that is produced by the standard prescription of MESA. Following this path the stellar properties of MESA and PARSEC are consistent and comparable, however is important to clarify that there is no clear consensus on which configuration is the correct one because RSG winds are still poorly understood Choi et al. (2016); Mauron and Josselin (2011). This version of the code does not include the Eddington factor and also implements a correction on the  $\alpha$  coefficients used for the computation of Wolf-Rayet (WR) winds presented in Renzo et al. (2020), suppressing the artificial enhancing of mass loss during that phase.

**Figure 2.2**

*MESA hydrogen, helium, and carbon profiles of some of the pre-merger stars, at different evolutionary stages.*



*Note.* From top to bottom panels: pre-collision stars of  $58 M_{\odot}$ ,  $65 M_{\odot}$ ,  $75 M_{\odot}$  and  $85 M_{\odot}$  respectively. From left to right columns: pre-collision stars profiles at Zero Age Main Sequence (ZAMS), Terminal Age Main Sequence (TAMS), Core Helium Burning (CHeB), and Core Carbon Burning (CCB) respectively. Solid red lines indicate the mass fraction of hydrogen along the radius for each star. The dashed blue lines indicate the mass fraction of helium along the radius for each star. The dash-dotted black lines indicate the mass fraction of carbon along the radius for each star. All models have by construction the same physics on MESA star. The main difference between them is the core extension and composition, as well as the increase in the final radius with the increasing age, as expected from different evolutionary stages for stars of similar mass.

The MESA stellar profiles generated using this configuration span a broader range of masses and evolutionary states than the ones previously explored with PARSEC. The mass distribution ranges from  $40$  to  $90 M_{\odot}$ , simulating one star every  $5 M_{\odot}$ , except for the cases corresponding to  $42$  and

$58 M_{\odot}$  which were generated to contrast the results presented in Renzo et al. (2020) and Costa et al. (2022), as well as to compare them directly with the PARSEC profiles. Each of these simulations produced profiles in up to four different evolutionary states: Zero Age Main Sequence (ZAMS), TAMS, CHeB, and Core Carbon Burning (CCB) (see figure 2.2). The stopping conditions that defined each of the phases are  $L_{nuc}/L > 0.99$  for ZAMS, the concentration of  ${}^1\text{H} < 0.0001$  inside the core for TAMS, the concentration of  ${}^4\text{He} < 0.0001$  inside the core for CHeB and the concentration of  ${}^{12}\text{C} < 0.0001$  inside the core for CCB. The evolutionary stages selected for the generation of these profiles are determined to coincide with the analyses and results of previous studies on the problem (Ballone et al., 2023; Costa et al., 2022; Di Carlo, Mapelli, Bouffanais, et al., 2020; Renzo et al., 2020). Depending on the convergence, some stars generated fewer profiles because they did not reach the most advanced evolutionary stages. Combining all these factors, a total of 39 1D MESA stellar profiles were generated that can be used as the initial conditions for hydrodynamical simulations of massive star collisions.

## 2.2 STARSMASHER: collision simulations

The second step in the massive stellar collision simulation chain is to transform the 1D stellar profiles into a 3D hydrodynamical distribution of particles that will model the input stars. After that process the direct encounter will be computed, tracking the changes in the hydrodynamical properties of the full set of particles, and finally producing the 3D remnant star to be analyzed. STARSMASHER\* is a Smoothed Particle Hydrodynamics (SPH) code especially suited for this purpose (Gaburov, Lombardi, & Zwart, 2010). Originally named as STARCRASH (Rasio, 1991), this code has been maintained and developed by several authors until arising to its actual configuration (Faber & Rasio, 2000; Gaburov, Bédorf, & Zwart, 2010; Gaburov, Lombardi, & Zwart, 2010; J. Lombardi Jr et al., 2006; J. C. Lombardi Jr, Sills, Rasio, & Shapiro, 1999).

### 2.2.1 SPH astrophysical hydrodynamics scheme

SPH was firstly proposed by Lucy (1977) and Gingold and Monaghan (1977) to be applied into the calculation of dynamical fission instabilities in rapidly rotating stars. During the following years, it was developed in-depth and applied to multiple astrophysical problems, until it became one of the most widely used schemes in computational physics (Benz, 1990; Hernquist & Katz, 1989; Monaghan, 1992, 2005). Its range of applicability scales to all processes in the Universe that have been shaped by fluid dynamical processes, from planetary formation, through stellar dynamics and galaxy evolution (Rosswog, 2009). SPH is a Lagrangian method, meaning that is purely mesh-free. Here the fluid is represented by a finite number ( $i$ ) of particles (fluid elements), and all the hydrodynamical properties, and their derivatives, are evaluated in a coordinate system attached to them. The 'size' of those particles is determined by the smoothing length ( $h_i$ ), a purely numerical quantity that settles the local spatial resolution and is involved, directly or indirectly, in the computation of all the properties: the position ( $\mathbf{r}_i$ ), velocity ( $\mathbf{v}_i$ ), acceleration ( $\mathbf{a}_i$ ), density ( $\rho_i$ ), mass ( $m_i$ ), specific internal energy ( $u_i$ ), etc. (Gaburov, Lombardi, & Zwart, 2010).

---

\*<https://github.com/jalombar/starsmasher>

### Smoothing kernel convolution process

There are two main ways to obtain the hydrodynamics equations for fluid elements. The first option is to discretize the Lagrangian form of the Euler equations, generating an equal mass particle distribution model (J. Lombardi Jr et al., 2006). The second path is to derive the SPH equations from the variational principle, producing a non-equal mass approach (Gaburov, Lombardi, & Zwart, 2010). The current version of STARSMASHER allows both treatments and depending on the needed simulation one method can stand over the other. The equal mass particles scenario ensures the conservation of energy, linear and angular momentum, and also prevents the large fluctuations from the interaction between light and massive particles (Rosswog, 2009). However, the case of non-equal mass particles allows to resolve both, the core and the envelope of the parent stars, becoming the perfect methodology for generating massive star collision simulations (Ballone et al., 2023; Gaburov, Lombardi, & Zwart, 2010). It is important to note that this discretization process also allows the excellent preservation of all particle properties, a fact that explains much of the SPH's success (Rosswog, 2009).

In the variational derivation that is coded inside STARSMASHER, the quantity that is roughly constant for all particles is the number of neighbors ( $N_i$ ). This is because the mixing during the collision will produce a lot of numerical resolution problems if the usual constraint between density and smoothing length ( $h_i = f(\rho_i, C_i)$ ) is preserved (Gaburov, Lombardi, & Zwart, 2010). Relaxing the integer condition on  $N_i$ , the code weights each neighbor with a function  $G(r_{ij}/h_i)$  that depends on the separation between particles ( $r_{ij}$ ) (Gaburov, Lombardi, & Zwart, 2010). Following that path, the number of neighbors for a given particle  $i$  is determined by

$$N_i = \sum_j G(|\mathbf{r}_i - \mathbf{r}_j|, h_i) \equiv \sum_j G_{ij}(h_i). \quad (2.1)$$

The definition of  $G_{ij}(h_i)$  was founded empirically, ensuring that the function provides satisfactory results:

$$G(x, h) \equiv V(4h - 4|x - h|, h), \quad (2.2)$$

where  $0 \leq x < 2h$ , otherwise it is equal to zero, and

$$V(x, h) \equiv 4\pi \int_0^x x^2 W(x, h) dx. \quad (2.3)$$

Here,  $W(x, h)$  is an SPH smoothing kernel with a compact support of  $2h$  (Gaburov, Lombardi, & Zwart, 2010). In this scheme, derivatives are calculated via a kernel approximation without the need for finite differences. This trick allows to transform the partial differential equations of Lagrangian fluid dynamics into ordinary differential equations, ensuring conservation by construction (Rosswog, 2009). This approach allows to write any function  $f(\mathbf{r})$  as

$$\tilde{f}_h(\mathbf{r}) = \int f(\mathbf{r}') W(\mathbf{r} - \mathbf{r}', h) d^3 r', \quad (2.4)$$

where  $W(\mathbf{r} - \mathbf{r}', h)$  is the aforementioned smoothing kernel (or window function) and the smoothing length determines its width (see figure 2.3). In the limit of an infinitely small smoothing region, the original function must be recovered, therefore the kernel fulfill

$$\lim_{h \rightarrow 0} \tilde{f}_h(\mathbf{r}) = f(\mathbf{r}) \quad \text{and} \quad \int W(\mathbf{r} - \mathbf{r}', h) d^3 r' = 1, \quad (2.5)$$

including also the  $\delta$ -distribution property in the limit of vanishing smoothing length (Rosswog, 2009).

Equation 2.4 can be rewritten in terms of the mass density  $\rho$

$$\tilde{f}_h(\mathbf{r}) = \int \frac{f(\mathbf{r}')}{\rho(\mathbf{r}')} W(\mathbf{r} - \mathbf{r}', h) \rho(\mathbf{r}') d^3 r', \quad (2.6)$$

and replacing the integral with a sum over a set of interpolation points (particles)

$$f(\mathbf{r}) = \sum_b \frac{m_b}{\rho_b} f_b W(\mathbf{r} - \mathbf{r}_b, h), \quad (2.7)$$

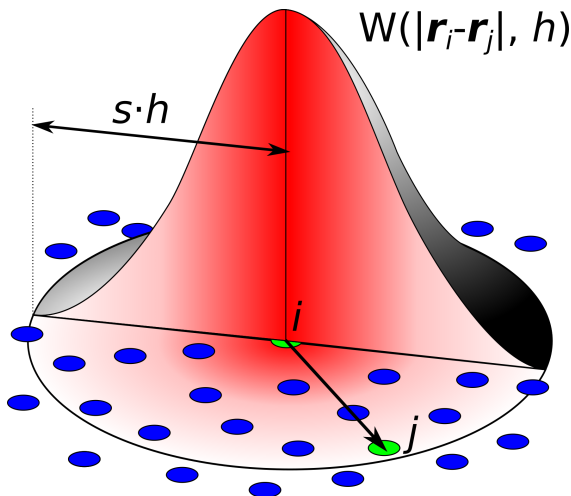
where the mass  $m_b$  comes from the  $\rho(\mathbf{r}') d^3 r'$  factor. Replacing  $f_b$  in the previous formula we can arrive to

$$\rho(\mathbf{r}) = \sum_b m_b W(\mathbf{r} - \mathbf{r}_b, h). \quad (2.8)$$

This density estimation by summing up kernel-weighted masses in the neighborhood, shows explicitly the discretization process of the SPH scheme (Rosswog, 2009).

**Figure 2.3**

Schematic view of the SPH kernel convolution.



*Note.* The blue dots represent the fluid elements in the SPH scheme.  $W(\mathbf{r}_i - \mathbf{r}_j, h)$  is the smoothing kernel, with  $h$  the smoothing length. The  $s \cdot h$  line is the visualization of the actual 'size' of each particle thanks to the convolution process.\*

---

\* Taken from Jlcercos - Own work, CC BY-SA 4.0, <https://commons.wikimedia.org/w/index.php?curid=70225405>

In the implementation used for this study, the settle kernel in STARSMASHER was the cubic spline proposed by [Monaghan and Lattanzio \(1985\)](#):

$$W(r, h) = \frac{1}{\pi h^3} \begin{cases} 1 - \frac{3}{2} \left( \frac{r}{h} \right)^2 + \frac{3}{4} \left( \frac{r}{h} \right)^3, & 0 \leq \frac{r}{h} < 1, \\ \frac{1}{4} \left( 2 - \frac{r}{h} \right)^3, & 1 \leq \frac{r}{h} < 2, \\ 0, & \frac{r}{h} \geq 2. \end{cases} \quad (2.9)$$

This kernel is spherically symmetric, allowing the exact conservation of linear and angular momentum in the computation of pressure forces, and also fulfilling the needed conditions for the computation of the gravitational force. It has continuous first and second derivatives, and the interpolation errors do not exceed  $O(h^2)$  ([Monaghan & Lattanzio, 1985](#)).

## Variational formulation

The SPH discretize Lagrangian coded in this version of STARSMASHER is

$$\mathcal{L} = \frac{1}{2} \sum_j m_j v_j^2 - \sum_j m_j u_j - \frac{1}{2} \sum_j m_j \phi_j. \quad (2.10)$$

Where,  $m_j$  is the mass of SPH particle  $j$ ,  $v_j$  and  $u_j$  its velocity and specific internal energy, respectively, and  $\phi_j$  is its gravitational potential, defined as

$$\phi_j = \sum_k m_k g(|\mathbf{r}_j - \mathbf{r}_k|, h_j) \equiv \sum_k m_k g_{jk}(h_j), \quad (2.11)$$

being  $g(x, h)$  the gravitational potential between two particles of unit mass ([Gaburov, Lombardi, & Zwart, 2010](#)). Solving the Euler-Lagrange equation for 2.10 the resulting equations of motion are

$$m_i \dot{\mathbf{v}}_i = - \sum_j m_j \left( \frac{\partial u}{\partial \rho} \right)_{s,j} \frac{d\rho_j}{d\mathbf{r}_i} - \frac{1}{2} \sum_j m_j \frac{d\phi_j}{d\mathbf{r}_i}. \quad (2.12)$$

The first term in 2.12 corresponds to the hydrodynamical force ( $m_i \mathbf{a}_{h,i}$ ) and the second term is the gravitational force ( $m_i \mathbf{a}_{g,i}$ ). The partial derivative  $(\partial u / \partial \rho)_s$  is evaluated at constant entropy.

Rewriting equation 2.8 we have a direct expression for the density

$$\rho_j = \sum_k m_k W(|\mathbf{r}_j - \mathbf{r}_k|, h_j) \equiv \sum_k m_k W_{jk}(h_j), \quad (2.13)$$

and differentiating it with respect to the position we can obtain the density gradient

$$\frac{d\rho_j}{d\mathbf{r}_i} = \sum_k m_k \nabla_i W_{ik}(h_i) \delta_{ij} + m_i \nabla_i W_{ij}(h_j) + \sum_k m_k \frac{\partial W_{jk}(h_j)}{\partial h_j} \frac{dh_j}{d\mathbf{r}_i}. \quad (2.14)$$

Deriving the expression 2.1 we obtain

$$\chi_j \frac{dh_j}{d\mathbf{r}_i} = - \sum_k \nabla_i G_{jk}(h_i) \delta_{ij} - \nabla_i G_{ij}(h_j), \quad (2.15)$$

where

$$\chi_j \equiv \sum_k \frac{\partial G_{jk}(h_j)}{\partial h_j}. \quad (2.16)$$

Combining these equations the acceleration due to pressure forces can be defined as

$$\begin{aligned} \mathbf{a}_{\text{h},i} = & - \sum_j m_j \frac{P_i}{\rho_i^2} \left[ \nabla_i W_{ij}(h_i) - \frac{\omega_i}{\chi_i m_j} \nabla_i G_{ij}(h_i) \right] \\ & - \sum_j m_j \frac{P_j}{\rho_j^2} \left[ \nabla_i W_{ij}(h_j) - \frac{\omega_j}{\chi_j m_i} \nabla_i G_{ij}(h_j) \right], \end{aligned} \quad (2.17)$$

while gravitational acceleration has the form of

$$\begin{aligned} \mathbf{a}_{\text{g},i} = & - \frac{1}{2} \sum_j m_j [\nabla_i g_{ij}(h_i) + \nabla_i g_{ij}(h_j)] + \frac{1}{2} \sum_j m_j \frac{\Psi_i}{\chi_i m_j} \nabla_i G_{ij}(h_i) \\ & + \frac{1}{2} \sum_j m_j \frac{\Psi_j}{\chi_j m_i} \nabla_i G_{ij}(h_j). \end{aligned} \quad (2.18)$$

Defining two new quantities:

$$\omega_j \equiv \sum_k m_k \frac{\partial W_{jk}(h_j)}{\partial h_j} \quad (2.19)$$

and

$$\Psi_i \equiv \sum_k m_k \frac{\partial g_{ik}(h_i)}{\partial h_i}. \quad (2.20)$$

The gravitational forces between particles are computed using direct summation on NVIDIA GPUs ([Gaburov, Lombardi, & Zwart, 2010](#)). This direct summation methodology, instead of a tree-based algorithm for gravity, increases the accuracy of the gravity calculations, particularly in terms of energy and angular momentum conservation ([Ballone et al., 2023; Gaburov, Bédorf, & Zwart, 2010](#)).

## Equation of state

The prescriptions for the EOS remained fixed and followed the implementation of [J. Lombardi Jr et al. \(2006\)](#), modeling the star as an ideal gas with the inclusion of radiation pressure support

$$P_i = \frac{\rho_i k T_i}{\mu_i} + \frac{1}{3} a T_i^4, \quad (2.21)$$

where  $\mu_i$  is the mean molecular mass of each particle,  $k$  is the Boltzmann constant and  $a$  is the radiation constant. For the temperature  $T_i$ , the code solves the quartic equation

$$u_i = \frac{3}{2} \frac{k T_i}{\mu_i} + \frac{a T_i^4}{\rho_i}, \quad (2.22)$$

by making use of the analytic solution presented in, for example, [Thiele \(1991\)](#). Knowing the temperature the pressure is obtained straightforwardly from 2.21, and the total entropy in the system ( $S$ ) can be computed by

$$S = \sum_i m_i \left[ \frac{3k}{2\mu_i} \ln \left( \frac{3}{2} \frac{kT_i}{\mu_i} \rho_i^{-2/3} \right) + \frac{4aT_i^3}{3\rho_i} \right]. \quad (2.23)$$

The rate of change of the internal energy is calculated following the approach presented in [Monaghan \(2002\)](#). The equation 2.8 is derived with respect to the time, and by making a couple of simple replacements you can get to

$$\frac{du_i}{dt} = \frac{P_i}{\rho_i^2} \sum_j m_j (\mathbf{v}_i - \mathbf{v}_j) \cdot \left[ \nabla_i W_{ij}(h_i) - \frac{\omega_i}{\chi_i m_j} \nabla_i G_{ij}(h_i) \right], \quad (2.24)$$

which guarantees the conservation of total energy and entropy in the absence of shocks ([Gaburov, Lombardi, & Zwart, 2010](#)).

## Artificial viscosity

The absence of shocks in fluid dynamics is a very strong assumption ([Rosswog, 2009](#)), especially when simulating violent environments like stellar collisions, as in the case of STARSMASHER. Because of that, the SPH scheme needs to consider in its equations the treatment and propagation of shock waves along the fluid elements. Generally speaking, there are two numerical strategies to account for that: the first possibility is to use the analytical solution of a Riemann problem between two adjacent particles, and the second option is to add pseudo-microscopic terms that create entropy at the shock front, just as physical viscosity would do, but on a numerically resolvable scale ([Rosswog, 2009](#)). The second path is known as Artificial Viscosity (AV) and is the adopted strategy inside STARSMASHER.

The goal of AV is to introduce dissipative terms into the equations, giving the shocks a thickness comparable to the spacing of the particles. After that, the solution of the differential equations will be computed just as though there were no shocks at all ([VonNeumann & Richtmyer, 1950](#)). AV often does not seek to mimic physical viscosity, but only to translate its effects from a smaller interaction scale to a resolvable one ([Rosswog, 2009](#)). However, such treatment must meet a series of requirements so that it does not introduce unphysical artifacts ([Caramana, Shashkov, & Whalen, 1998](#)). It should be always dissipative, absent in rigid and differential rotation, absent in uniform compression, it should go smoothly to zero as the compression vanishes and it should be absent for expansion. Finally, and most importantly, it must be implemented to ensure the conservation of energy, momentum, and angular momentum ([Rosswog, 2009](#)).

In this version of STARSMASHER the AV is coded following a mixed approach between [Balsara \(1995\)](#) and [Monaghan \(1997\)](#). In both cases, an artificial viscous term ( $\Pi_{ij}$ ) is defined and included in the equation 2.24. The hybrid term is

$$\Pi_{ij} = \left( \frac{P_i}{\rho_i^2} + \frac{P_j}{\rho_j^2} \right) (-\alpha \mu_{ij} + \beta \mu_{ij}^2), \quad (2.25)$$

where

$$\mu_{ij} = \frac{(\mathbf{v}_i - \mathbf{v}_j) (\mathbf{r}_i - \mathbf{r}_j)}{|\mathbf{r}_i - \mathbf{r}_j|} \frac{f_i + f_j}{c_i + c_j}, \quad (2.26)$$

for  $(\mathbf{v}_i - \mathbf{v}_j)(\mathbf{r}_i - \mathbf{r}_j) < 0$ ; otherwise  $\mu_{ij} = 0$ . Here  $\alpha = 1$ ,  $\beta = 2$ ,  $c_i$  is the sound speed at particle  $i$  and  $f_i$  is the form function for particle  $i$  defined by

$$f_i = \frac{|\nabla \cdot \mathbf{v}|_i}{|\nabla \cdot \mathbf{v}|_i + |\nabla \times \mathbf{v}|_i + \eta' c_i / h_i}, \quad (2.27)$$

with

$$(\nabla \cdot \mathbf{v})_i = \frac{1}{\rho_i} \sum_j m_j (\mathbf{v}_j - \mathbf{v}_i) \cdot \nabla_i W_{ij} (h_i), \quad (2.28)$$

and

$$(\nabla \times \mathbf{v})_i = \frac{1}{\rho_i} \sum_j m_j (\mathbf{v}_i - \mathbf{v}_j) \times \nabla_i W_{ij} (h_i). \quad (2.29)$$

The factor  $\eta' = 10^{-5}$  prevent numerical divergences (J. Lombardi Jr et al., 2006). The final form for the variation of the specific internal energy accounting for shocks is

$$\frac{du_i}{dt} = \sum_j m_j \left( \frac{P_i}{\rho_i^2} + \frac{1}{2} \Pi_{ij} \right) (\mathbf{v}_i - \mathbf{v}_j) \cdot \left[ \nabla_i W_{ij} (h_i) - \frac{\omega_i}{\chi_i m_j} \nabla_i G_{ij} (h_i) \right]. \quad (2.30)$$

### Time stepping

The integration process of the ordinary differential equations in the SPH methodology needs to find a reasonable compromise between accuracy and efficiency. Usually, computational resources should be used in the calculation of a larger number of particles to increase the resolution of the simulations, rather than in a higher-order integration scheme. Due to the fact that the evaluation of derivatives is a very expensive numerical operation, in particular for self-gravitating fluids, the idea is to minimize the number of force evaluations per time step, giving preference to low-order integrators (Rosswog, 2009). This version of STARSMASHER follows the symplectic integrator, with shared symmetrized time-steps, described in Springel (2005). The idea is to apply a modified leapfrog scheme where the shared time step is

$$\Delta t = \text{Min}_i \left[ \left( \Delta t_{1,i}^{-1} + \Delta t_{2,i}^{-1} \right)^{-1} \right], \quad (2.31)$$

and for each SPH particle  $i$

$$\Delta t_{1,i} = C_{N,1} \frac{h_i}{\text{Max} [\text{Max}_j (\kappa_{ij}), \text{Max}_j (\kappa_{ji})]}, \quad (2.32)$$

defining

$$\kappa_{ij} \equiv \left[ \left( \frac{p_i}{\rho_i^2} + \frac{1}{2} \Pi_{ij} \right) \rho_i \right]^{1/2}, \quad (2.33)$$

and

$$\Delta t_{2,i} = C_{N,2} \frac{u_i}{|\mathrm{d}u_i/\mathrm{d}t|}. \quad (2.34)$$

Here  $C_{N,1}$  goes from 0.2 to 0.3, and  $C_{N,2} = 0.05$ . The  $\mathrm{Max}_j$  function in equation 2.32 refers to the maximum of the value of its expression for all particles  $j$  that are neighbors with  $i$ . The denominator of equation 2.32 is an approximate upper limit to the signal propagation speed near particle  $i$ . The incorporation of  $\Delta t_2$  enables us to treat shocks without drastically decreasing the time-step during intervals in which the flow is subsonic (Gaburov, Lombardi, & Zwart, 2010).

## Code units

The numerical results from STARSMASHER are calculated following a unit system where  $G = M_\odot = R_\odot = 1$ , with  $G$  the Newtonian gravitational constant, and  $M_\odot$  and  $R_\odot$  the mass and radius of the Sun respectively (Gaburov, Lombardi, & Zwart, 2010). The units of time, velocity, and energy are

$$t_u = \left( \frac{R_\odot^3}{GM_\odot} \right)^{1/2} = 1594 \text{ s}, \quad (2.35)$$

$$v_u = \left( \frac{GM_\odot}{R_\odot} \right)^{1/2} = 437 \text{ km s}^{-1}, \quad (2.36)$$

$$E_u = \frac{GM_\odot^2}{R_\odot} = 3.79 \times 10^{48} \text{ erg}. \quad (2.37)$$

### 2.2.2 STARSMASHER prescriptions

As explained at the beginning of this chapter, STARSMASHER simulates stellar collisions in two steps. The first one is the transformation of the 1D profiles coming from stellar evolution codes into a 3D particle distribution following the SPH scheme. This particle distribution undergoes a relaxation routine until a stable star is obtained, which will be used as input for the next step: the simulation of the direct encounter.

#### Relaxation routine

The description and default values of the input parameters used in this study are shown in tables 2.1 and 2.2 respectively. The execution of the relaxation routines was performed for the entire set of PARSEC stellar profiles described in the subsection 2.1.1, and only for two MESA profiles selected from the set introduced in the subsection 2.1.2.

The CHeB and TAMS stars of  $58 M_\odot$  generated with PARSEC, in addition to the TAMS star of  $60 M_\odot$  from MESA, were simulated using a total amount of 799020 SPH particles. This particular number was set in order to ensure conversion of the numerical methods, while guaranteeing the spatial resolution needed to describe very massive stars.

**Table 2.1**

*Description of the main parameters encoded in STARSMASHER for the single star relaxation routine.*

Name	Description
tf	Desired final time to stop simulation
dtout	How often an output file should be dumped
n	Desired number of particles
nnopt	Controls neighbor number
nav	Artificial viscosity flag
alpha	AV coefficient for $\mu$ term
beta	AV coefficient for $\mu^2$ term
ngr	Gravity flag
nrelax	Relaxation flag
trelax	Timescale for artificial drag force
equalmass	Particle mass is proportional to $\rho^{1-\text{equalmass}}$
treloff	Time to switch from relaxation to dynamical calculation
tresplintmuoff	Time to stop resplinting the mean molecular weight
nitpot	Iterations to evaluate the potential energy
nintvar	Integration flag
ngravprocs	Number of gravity processors
qthreads	Number of GPU threads per particle
runit	Number of cm in the unit of length
munit	Number of g in unit of mass
ppn	Number of CPU cores per node
profilefile	1D stellar profile input file name
stellarevolutioncodetype	Code used for the generation of the input file

*Note.* Columns from left to right: parameter name and its general description in single star relaxation simulations.

For lighter stars in their initial evolutionary stage, the amount of needed SPH particles is reduced. That is the case of the MS and MS + 2 Myr PARSEC profiles of  $42 M_{\odot}$ , and the ZAMS star of  $40 M_{\odot}$  from MESA. The relaxation routine for this set of stellar profiles was run using a total amount of 90000 particles.

Thanks to the STARSMASHER methodology of ensuring a constant and uniform number density distribution of particles, the determination of the number of fluid elements in the simulation automatically set their masses. Due to the fact that the mass density of stars spans several orders of magnitude from their center to their atmospheres, particles with different masses can spatially sample each layer of the star in a spatially uniform way (Ballone et al., 2023). The big difference in resolution for the  $\sim 40$  and  $\sim 60 M_{\odot}$  set of simulations described above, is forced by the much wider dynamical range of mass density spanned by the heaviest and most evolved stars, in addition to their much larger radius. Finally, in terms of mass, the resolution of SPH particles ranges from  $\sim 2 \cdot 10^{-11}$  to  $\sim 7.6 M_{\odot}$  and from  $\sim 4 \cdot 10^{-7}$  to  $1.4 \cdot 10^{-2} M_{\odot}$  for the CHeB/TAMS and MS/ZAMS stars, respectively.

**Table 2.2**

*Default values of the main parameters encoded in STARSMASHER for the single star relaxation routine.*

Name	Default value
tf	200
dtout	1
n	90000 or 799020
nnopt	23 equivalent to $\sim 40$ neighbors
nav	3 to get a hybrid Balsara-Monaghan
alpha	1
beta	2
ngr	3
nrelax	1 for relaxation of single star
trelax	$10^{30}$
equalmass	0 for constant number density
treloff	1
tresplintmuoff	0
nitpot	1
nintvar	2 integration for internal energy
ngravprocs	-1
qthreads	0 to guess the best number of threads without timing
runit	$6.9599 \cdot 10^{10}$
munit	$1.9891 \cdot 10^{33}$
ppn	4
profilefile	star_PARSEC or star_MESA
stellarevolutioncodetype	0 for TWIN and 1 for PARSEC or MESA

*Note.* Columns from left to right: parameter name and its default values in single star relaxation simulations.

### Collision routine

The prescriptions for the collision simulations analyzed in this thesis are described in detail in the tables 2.3 and 2.4. Contrary to the relaxation routine, the inputs of the collisional scenario are not 1D stellar profiles but stars modeled with SPH. For the case of this study, all the previously described relaxed stars were used in the simulation of one or several stellar collisions.

In this type of calculations STARSMASHER allows not only the inclusion of numerical variables but also the incorporation of dynamical parameters, that determine the trajectories to be followed by the bodies involved in the direct encounters. Examples of such parameters are:  $\text{sep0}$  ( $d_{\text{init}}$ ),  $\text{bimpact}$  ( $b$ ) and  $\text{vinf}$  ( $v_\infty$ ). Its variations allow us to explore a wide range of possibilities without the need to obtain new star profiles and by performing the relaxation routines only once. It is important to highlight that all physical values tabulated in 2.2 and 2.4 follow the STARSMASHER system of units presented in equations 2.35, 2.36 and 2.37.

**Table 2.3**

*Description of the main parameters encoded in STARSMASHER for the collisional routine.*

Name	Description
tf	Desired final time to stop simulation
dtout	How often an output file should be dumped
nrelax	Relaxation flag
sep0	Initial separation of two stars in a collision calculation
bimpact	Impact parameter for collisions (actually is the periastron separation)
vinf	Velocity at infinity for the colliding stars
ngravprocs	Number of gravity processors
ppn	Number of CPU cores per node

*Note.* Columns from left to right: parameter name and its general description in collision simulations.

**Table 2.4**

*Default values of the main parameters encoded in STARSMASHER for the collisional routine.*

Name	Default value
tf	3000
dtout	0.5
nrelax	0 for dynamical calculation
sep0	109.36
bimpact	0
vinf	0.0005243
ngravprocs	2
ppn	16

*Note.* Columns from left to right: parameter name and its default values in collision simulations.

### 2.2.3 Simulation population

The entire set of STARSMASHER simulations produced for the development of this thesis, accounting for the relaxation and collision routines, are 18. All of them were analyzed in detail to corroborate that they fulfill the indispensable characteristics within the modeling of massive stars in the framework of the SPH scheme, including the fact that the physical hydrodynamical models were solved numerically in a congruent and satisfactory manner. Each simulation, and its time course, was monitored using SPLASH\*, a public software for the visualization of smoothed particle hydrodynamics data.

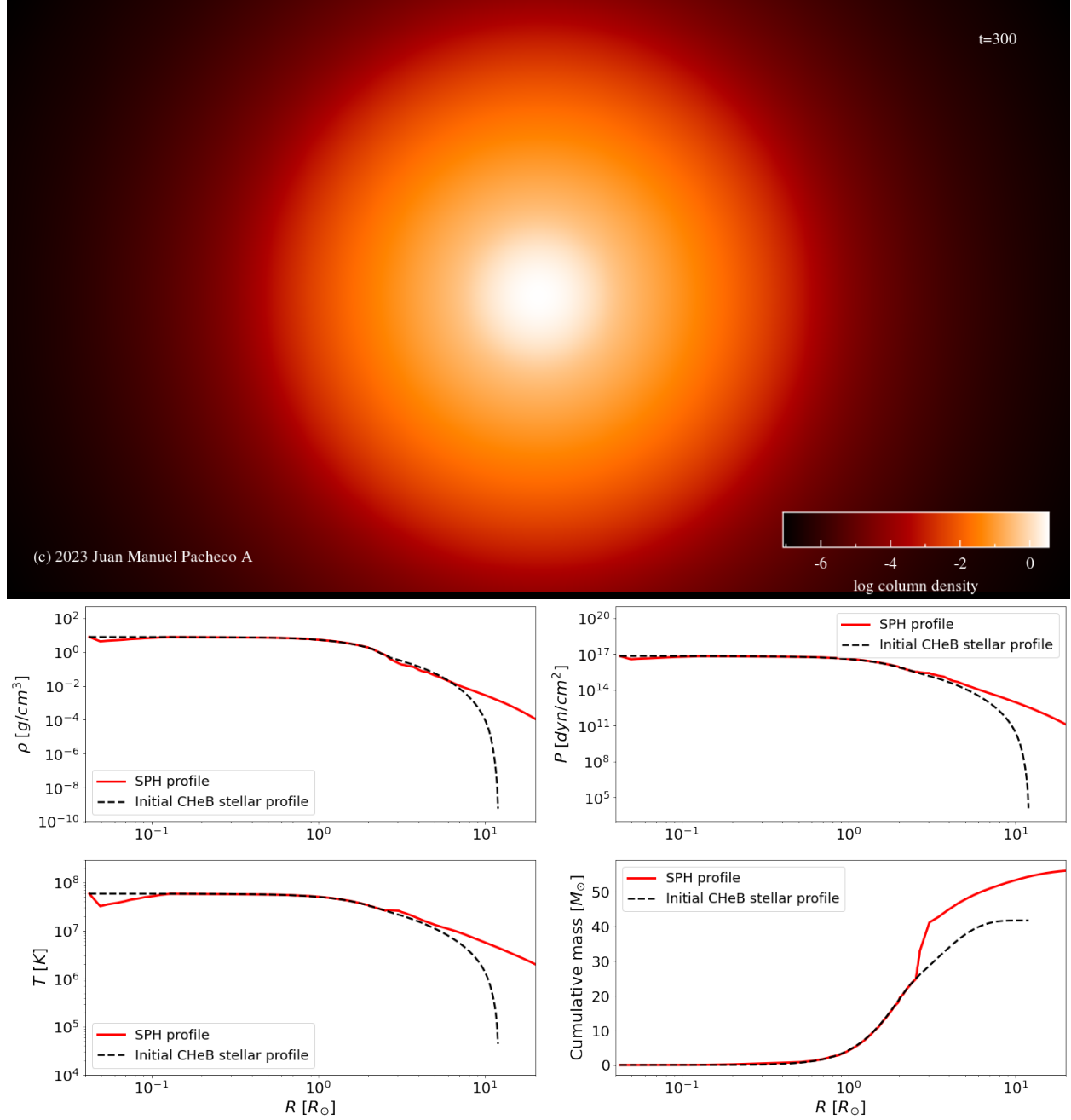
### Relaxed stars

The total amount of singularly relaxed stars is 7. The visualization of the final snapshot of each routine, together with the radial profiles of the main thermodynamical quantities can be seen in figures 2.4, 2.5, 2.6 and 2.7.

\*<https://splash-viz.readthedocs.io/en/latest/index.html#>

**Figure 2.4**

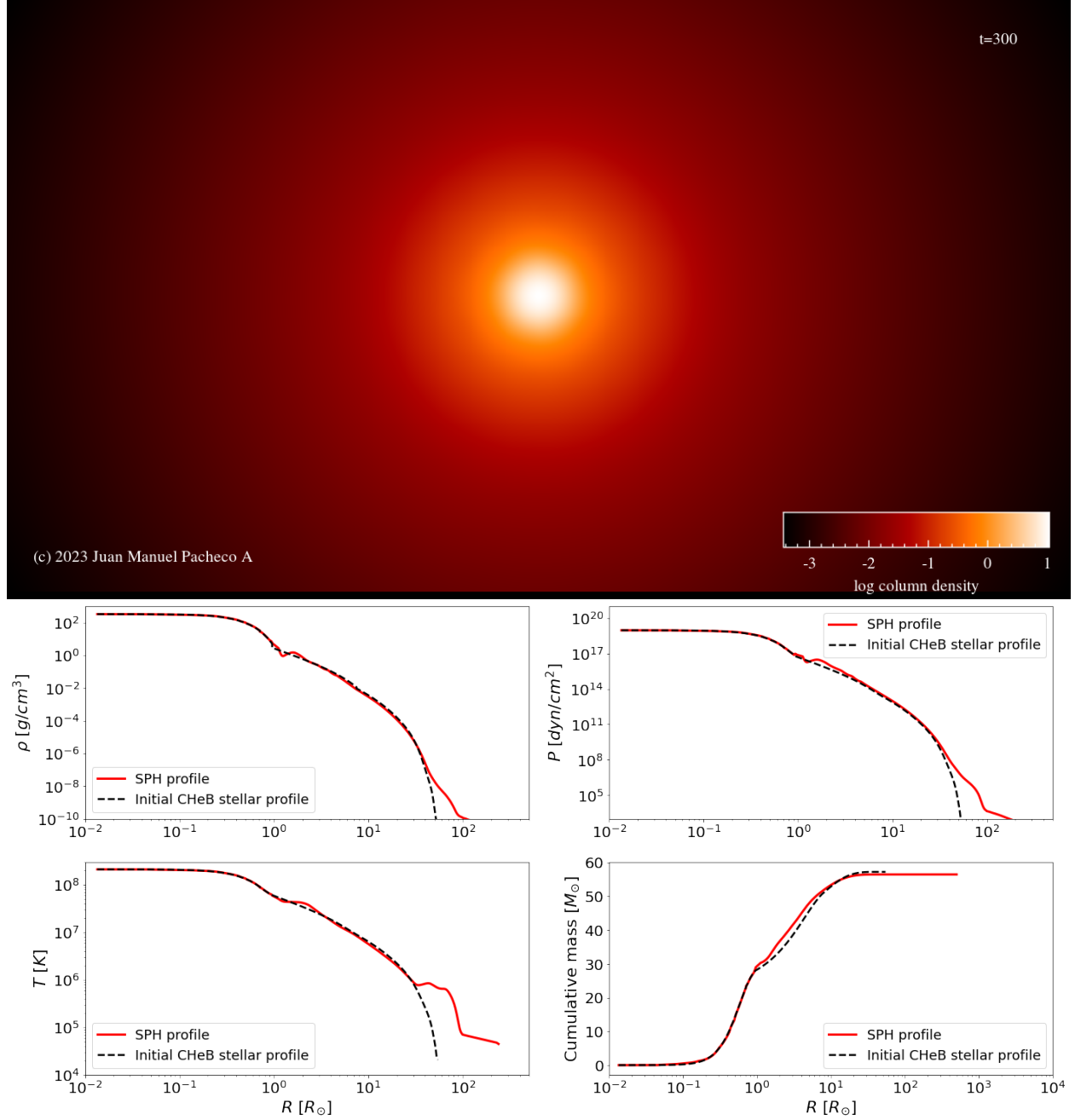
*STARSMASHER relaxation simulation for the MS + 2 Myr PARSEC profile of  $42 M_{\odot}$ .*



*Note.* Top panel: 2D logarithmic density map for the last output file (`out0300.sph`) of the STARSMASHER relaxation routine. The  $x$  and  $y$  axis range from  $-5$  to  $5 R_{\odot}$ , with the densest particle in the simulation as the origin. This image was generated using SPLASH. Middle panel from left to right: density profile in  $g/cm^3$  and pressure profile in  $dyn/cm^2$  along the stellar radius in  $R_{\odot}$ . Bottom panel from left to right: temperature profile in  $K$  and cumulative mass profile in  $M_{\odot}$  along the stellar radius. The red solid lines represent the SPH profile obtained after interpolating the average values obtained in the radial binning of all the particles in the simulation. The dashed black lines represent the input stellar profile MS + 2 Myr produced by PARSEC and described in section 2.1.1.

**Figure 2.5**

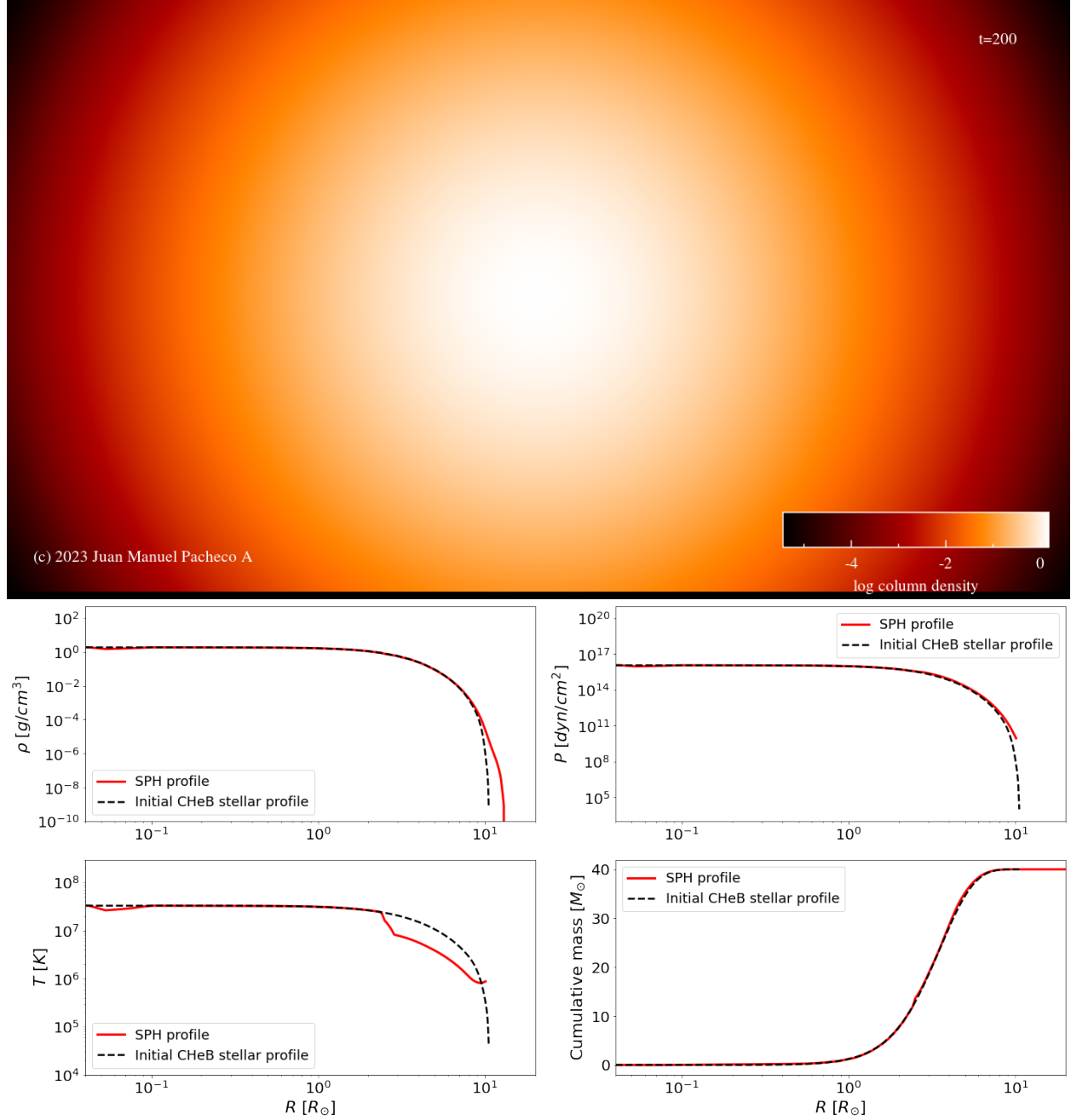
*STARSMASHER relaxation simulation for the CHeB PARSEC profile of  $58 M_{\odot}$ .*



*Note.* Top panel: 2D logarithmic density map for the last output file (`out0300.sph`) of the STARSMASHER relaxation routine. The  $x$  and  $y$  axis range from  $-10$  to  $10 R_{\odot}$ , with the densest particle in the simulation as the origin. This image was generated using SPLASH. Middle panel from left to right: density profile in  $g/cm^3$  and pressure profile in  $dyn/cm^2$  along the stellar radius in  $R_{\odot}$ . Bottom panel from left to right: temperature profile in  $K$  and cumulative mass profile in  $M_{\odot}$  along the stellar radius. The red solid lines represent the SPH profile obtained after interpolating the average values obtained in the radial binning of all the particles in the simulation. The dashed black lines represent the input stellar profile CHeB produced by PARSEC and described in section 2.1.1.

**Figure 2.6**

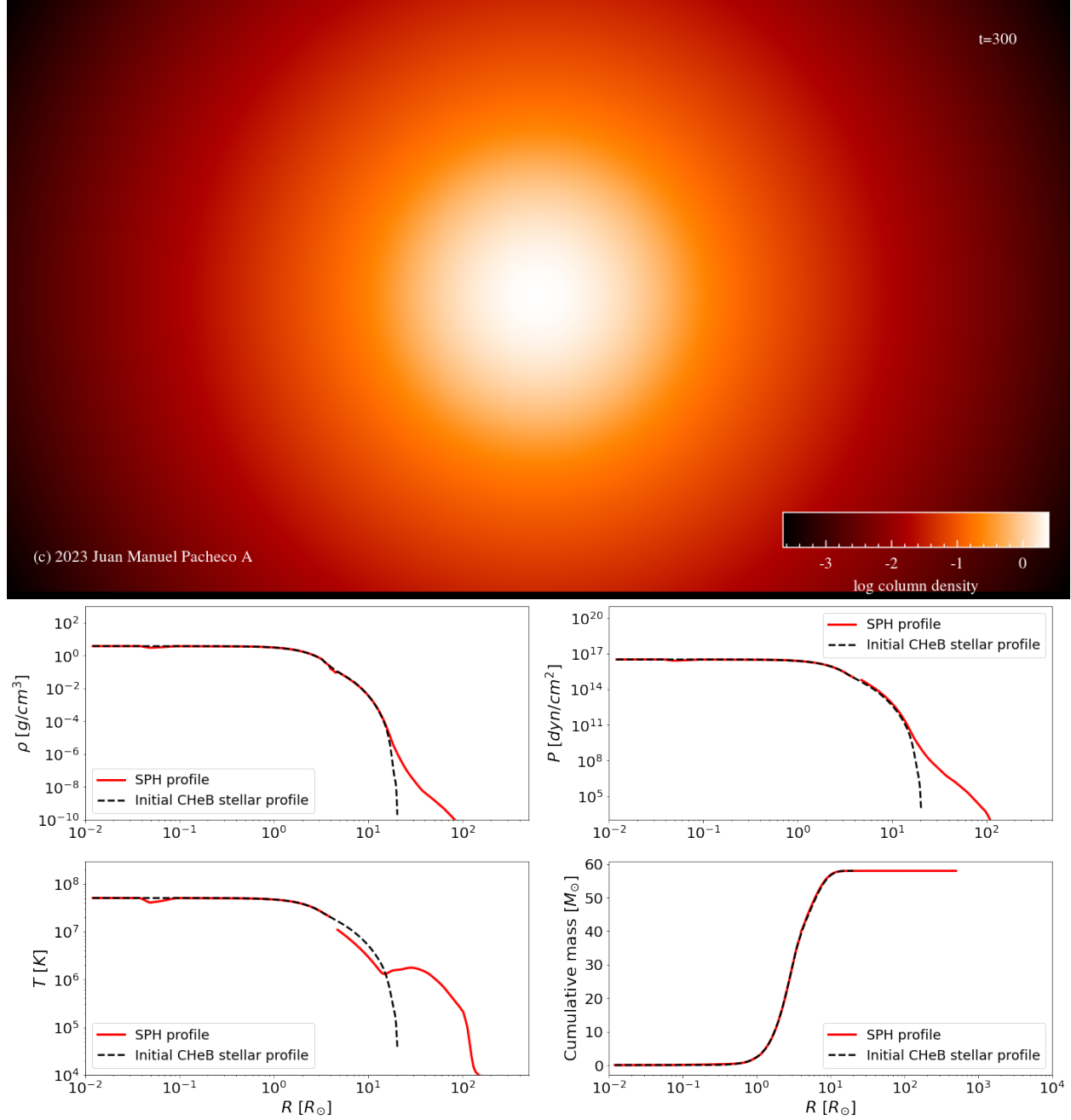
*STARSMASHER relaxation simulation for the ZAMS MESA profile of  $40 M_{\odot}$ .*



*Note.* Top panel: 2D logarithmic density map for the last output file (`out0200.sph`) of the STARSMASHER relaxation routine. The  $x$  and  $y$  axis range from  $-5$  to  $5 R_{\odot}$ , with the densest particle in the simulation as the origin. This image was generated using SPLASH. Middle panel from left to right: density profile in  $g/cm^3$  and pressure profile in  $dyn/cm^2$  along the stellar radius in  $R_{\odot}$ . Bottom panel from left to right: temperature profile in  $K$  and cumulative mass profile in  $M_{\odot}$  along the stellar radius. The red solid lines represent the SPH profile obtained after interpolating the average values obtained in the radial binning of all the particles in the simulation. The dashed black lines represent the input stellar profile ZAMS produced by MESA and described in section 2.1.2.

**Figure 2.7**

*STARSMASHER relaxation simulation for the TAMS MESA profile of  $60 M_{\odot}$ .*



*Note.* Top panel: 2D logarithmic density map for the last output file (`out0300.sph`) of the STARSMASHER relaxation routine. The  $x$  and  $y$  axis range from  $-10$  to  $10 R_{\odot}$ , with the densest particle in the simulation as the origin. This image was generated using SPLASH. Middle panel from left to right: density profile in  $g/cm^3$  and pressure profile in  $dyn/cm^2$  along the stellar radius in  $R_{\odot}$ . Bottom panel from left to right: temperature profile in  $K$  and cumulative mass profile in  $M_{\odot}$  along the stellar radius. The red solid lines represent the SPH profile obtained after interpolating the average values obtained in the radial binning of all the particles in the simulation. The dashed black lines represent the input stellar profile TAMS produced by MESA and described in section 2.1.2.

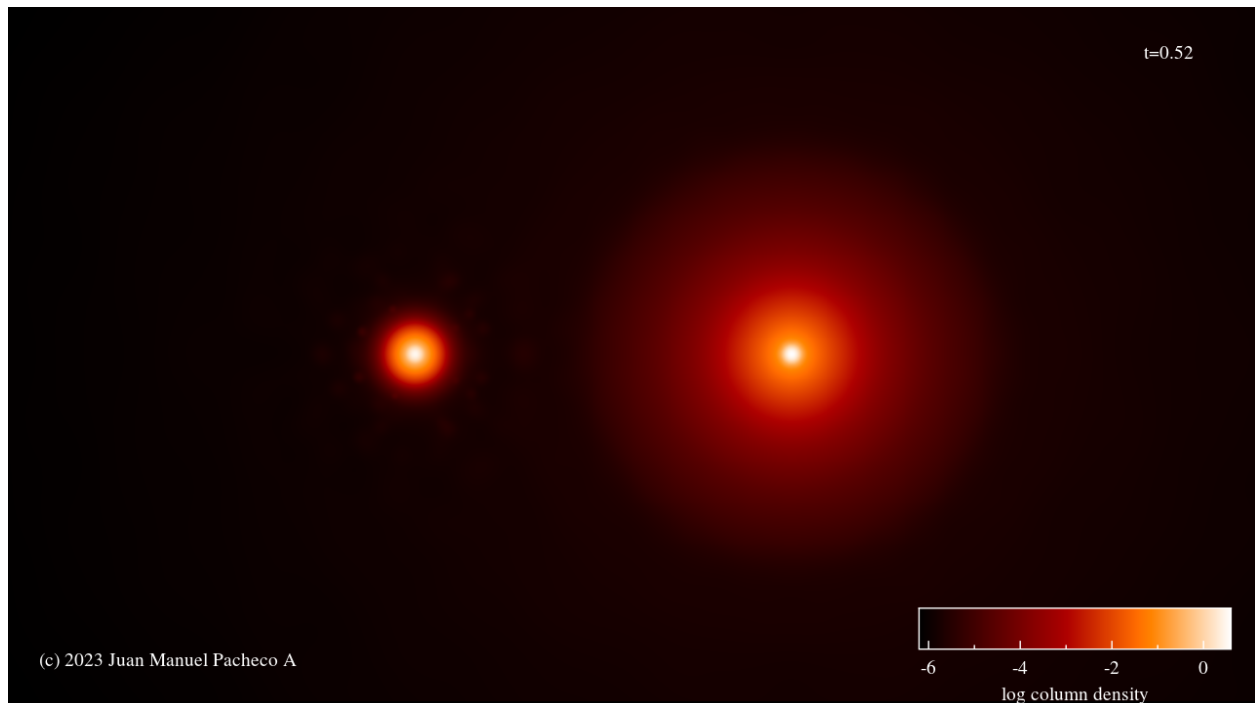
All relaxed stars were simulated for a total amount of time equivalent to 5.53 days, ensuring the hydrodynamical equilibrium by the end of the routine. The direct comparison of the radial profiles derived from STARSMASHER and the initial profiles obtained from MESA and PARSEC, allows us to conclude that the 3D distribution of SPH particles preserves the properties expected for each star, especially in the inner region. The perfect correlation, in both types of simulations, of the density ( $\rho$ ) and the cumulative mass profiles for almost all the layers of the stars, demonstrates that the particle construction methodology within the SPH system has been successfully implemented at STARSMASHER. The radial profiles can differ between the hydrodynamical treatment and the stellar evolution codes at the outer layers. This can be explained as a combination of two factors: the reduced resolution of the SPH scheme in the low-density region, inducing some numerical errors, and the simplified EOS implemented in STARSMASHER with respect to MESA and PARSEC, especially for the case of the pressure ( $P$ ) and the temperature ( $T$ ) (see section 2.2.1). Finally, it is important to clarify that the visualization of the 3 missing relaxed stars is attached in the appendices of this document (see figures 4.1, 4.2 and 4.3).

## Collisions

A total of 11 different collision configurations were analyzed for the development of this project. The SPLASH visualization of each of them can be seen in figures from 2.8 to 2.18.

**Figure 2.8**

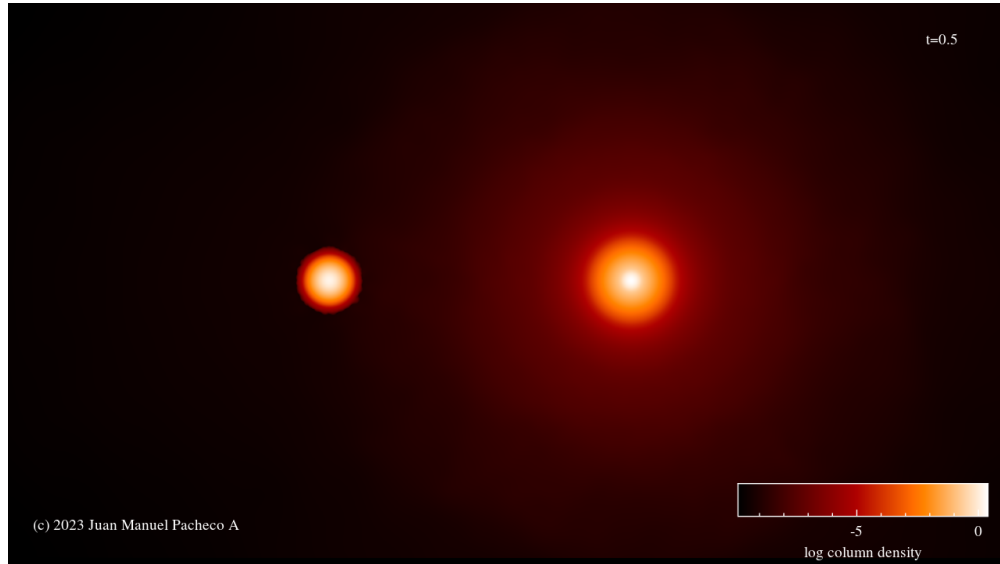
*Renzo et al. (2020): STARSMASHER collision simulation between the MS and TAMS PARSEC profiles of  $42 M_{\odot}$  and  $58 M_{\odot}$  respectively.*



*Note.* 2D logarithmic density map for the first output file (`out0001.sph`) of the STARSMASHER collisional routine. The  $x$  and  $y$  axis range from  $-100 R_{\odot}$  to  $100 R_{\odot}$ , with the center of mass as the origin. In this configuration  $d_{init} = 110 R_{\odot}$ ,  $v_{\infty} = 10 \text{ km/s}$  and  $b = 0 R_{\odot}$ . The total simulated time was 14.82 days.

**Figure 2.9**

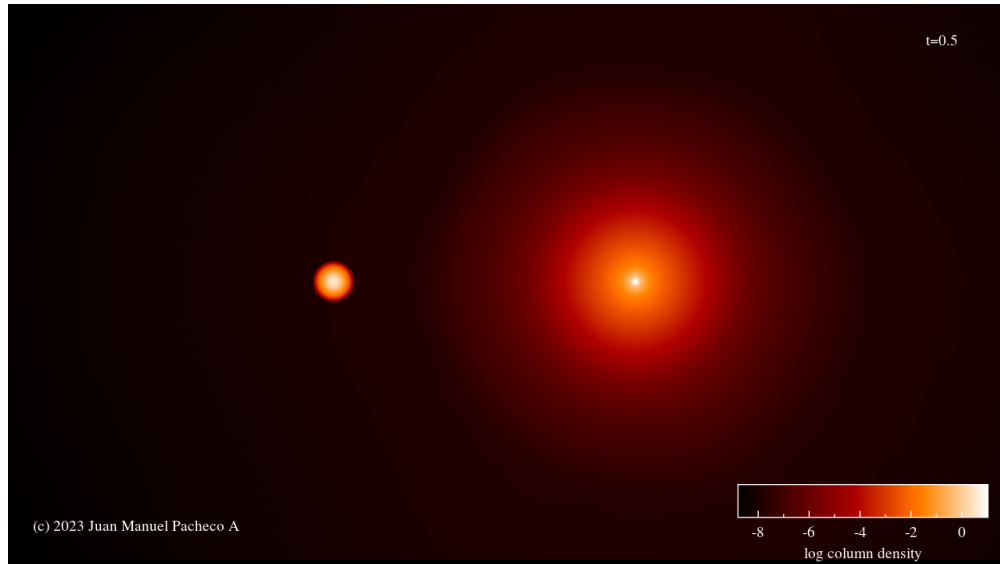
**60 TAMS vs 40 ZAMS:** STARSMASHER collision simulation between the ZAMS and TAMS MESA profiles of  $40 M_{\odot}$  and  $60 M_{\odot}$  respectively.



Note. 2D logarithmic density map for the first output file (`out0001.sph`) of the STARSMASHER collisional routine. The  $x$  and  $y$  axis range from  $-100 R_{\odot}$  to  $100 R_{\odot}$ , with the center of mass as the origin. In this configuration  $d_{init} = 110 R_{\odot}$ ,  $v_{\infty} = 10 \text{ km/s}$  and  $b = 0 R_{\odot}$ . The total simulated time was 9.22 days.

**Figure 2.10**

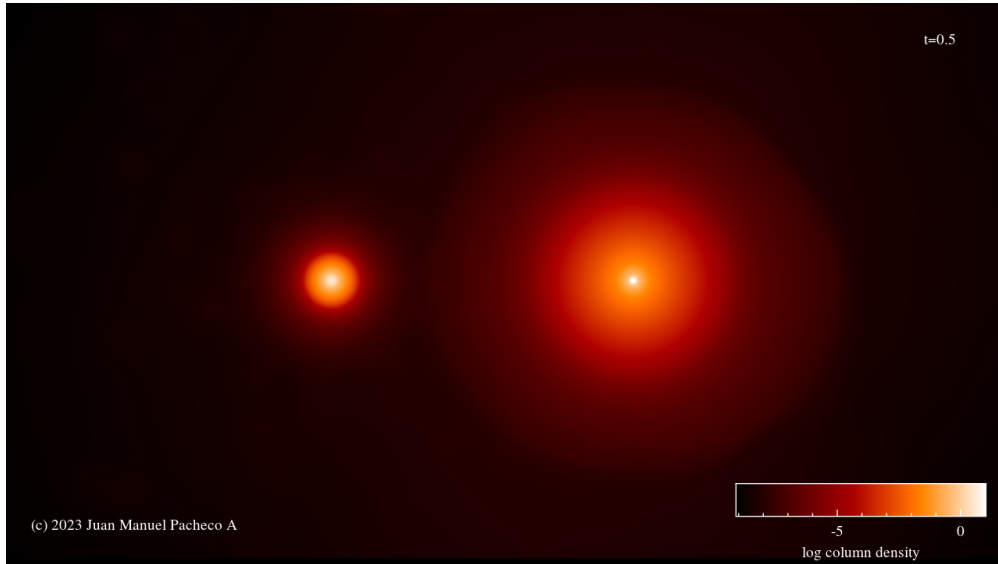
**Half Resolution:** STARSMASHER collision simulation between the MS and CHeB low resolution PARSEC profiles of  $42 M_{\odot}$  and  $58 M_{\odot}$  respectively.



Note. 2D logarithmic density map for the first output file (`out0001.sph`) of the STARSMASHER collisional routine. The  $x$  and  $y$  axis range from  $-100 R_{\odot}$  to  $100 R_{\odot}$ , with the center of mass as the origin. In this configuration  $d_{init} = 110 R_{\odot}$ ,  $v_{\infty} = 10 \text{ km/s}$  and  $b = 0 R_{\odot}$ . The total simulated time was 13.54 days.

**Figure 2.11**

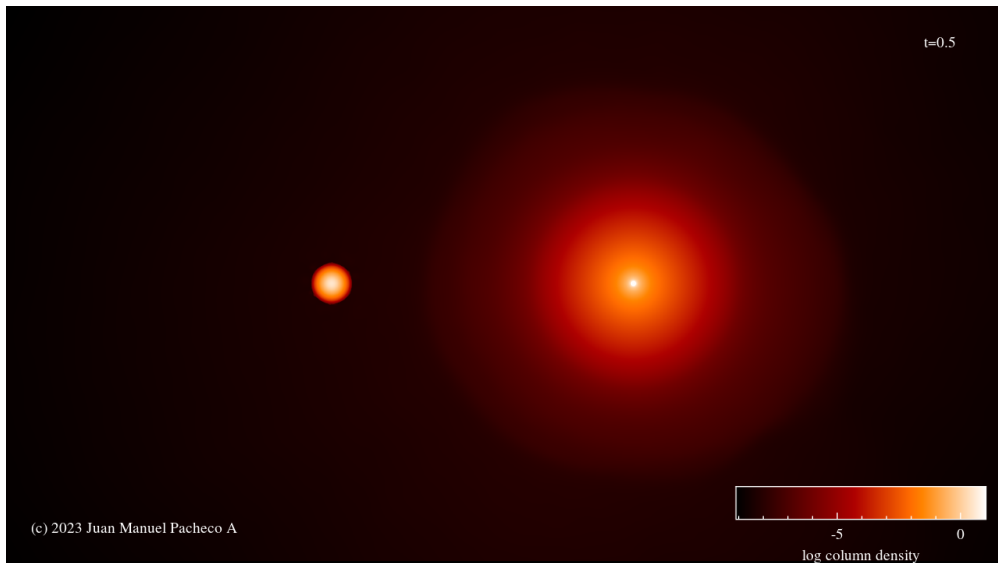
$+ 2 \text{ Myr}$ : STARSMASHER collision simulation between the MS + 2Myr and CHeB PARSEC profiles of  $42 M_{\odot}$  and  $58 M_{\odot}$  respectively.



Note. 2D logarithmic density map for the first output file (`out0001.sph`) of the STARSMASHER collisional routine. The  $x$  and  $y$  axis range from  $-100 R_{\odot}$  to  $100 R_{\odot}$ , with the center of mass as the origin. In this configuration  $d_{init} = 110 R_{\odot}$ ,  $v_{\infty} = 10 \text{ km/s}$  and  $b = 0 R_{\odot}$ . The total simulated time was 4.41 days.

**Figure 2.12**

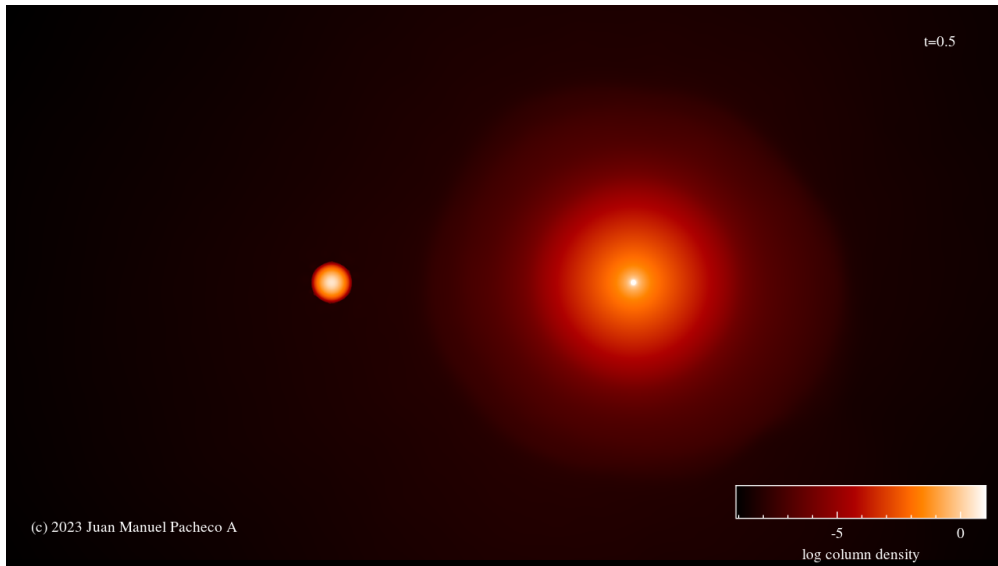
$v_{\infty} = 10 \text{ km/s}$ : STARSMASHER collision simulation between the MS and CHeB PARSEC profiles of  $42 M_{\odot}$  and  $58 M_{\odot}$  respectively.



Note. 2D logarithmic density map for the first output file (`out0001.sph`) of the STARSMASHER collisional routine. The  $x$  and  $y$  axis range from  $-100 R_{\odot}$  to  $100 R_{\odot}$ , with the center of mass as the origin. In this configuration  $d_{init} = 110 R_{\odot}$ ,  $v_{\infty} = 10 \text{ km/s}$  and  $b = 0 R_{\odot}$ . The total simulated time was 11.69 days.

**Figure 2.13**

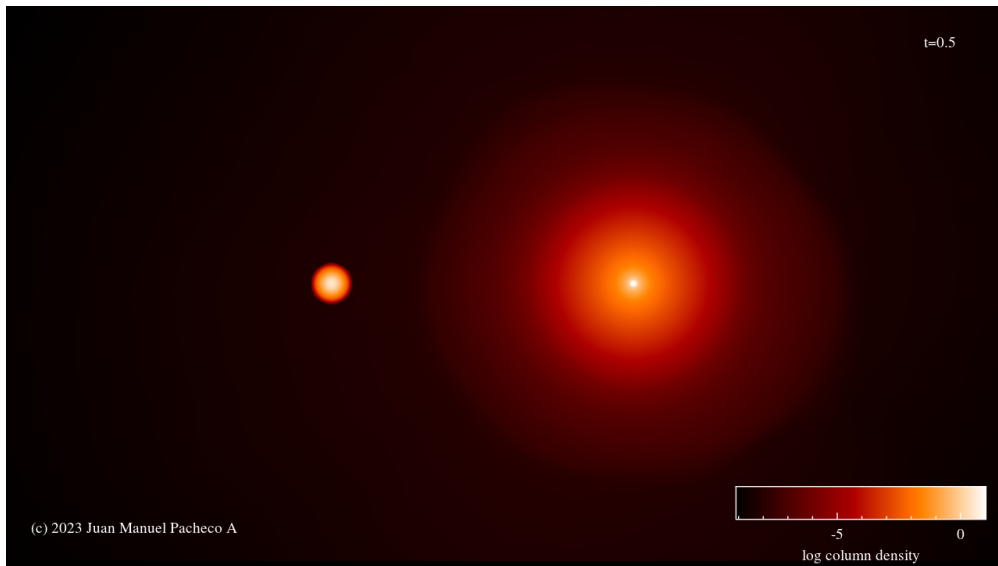
$v_\infty = 100 \text{ km/s}$ : STARSMASHER collision simulation between the MS and CHeB PARSEC profiles of  $42 M_\odot$  and  $58 M_\odot$  respectively.



Note. 2D logarithmic density map for the first output file (out0001.sph) of the STARSMASHER collisional routine. The  $x$  and  $y$  axis range from  $-100 R_\odot$  to  $100 R_\odot$ , with the center of mass as the origin. In this configuration  $d_{init} = 110 R_\odot$ ,  $v_\infty = 100 \text{ km/s}$  and  $b = 0 R_\odot$ . The total simulated time was 2.29 days.

**Figure 2.14**

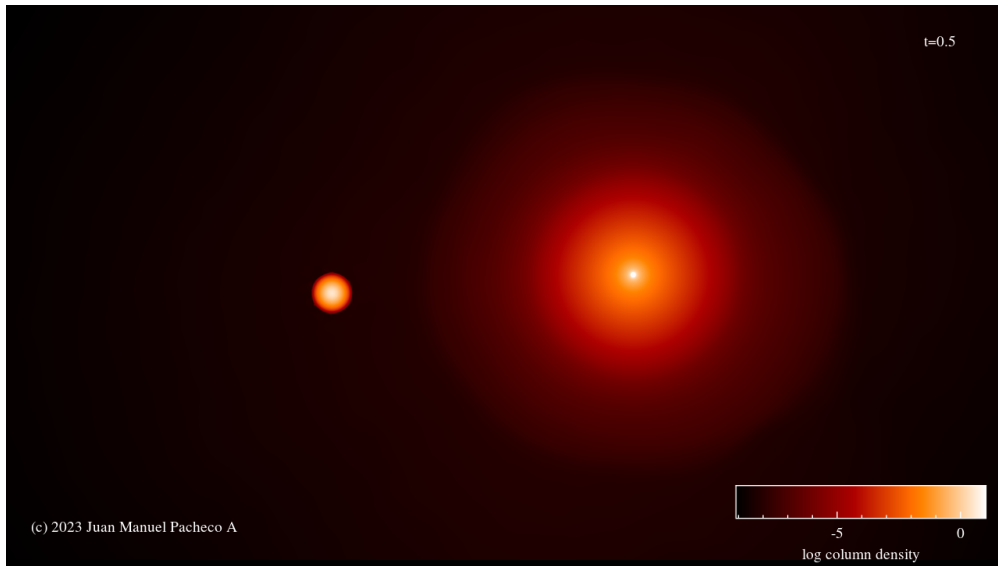
$v_\infty = 500 \text{ km/s}$ : STARSMASHER collision simulation between the MS and CHeB PARSEC profiles of  $42 M_\odot$  and  $58 M_\odot$  respectively.



Note. 2D logarithmic density map for the first output file (out0001.sph) of the STARSMASHER collisional routine. The  $x$  and  $y$  axis range from  $-100 R_\odot$  to  $100 R_\odot$ , with the center of mass as the origin. In this configuration  $d_{init} = 110 R_\odot$ ,  $v_\infty = 500 \text{ km/s}$  and  $b = 0 R_\odot$ . The total simulated time was 11.52 days.

**Figure 2.15**

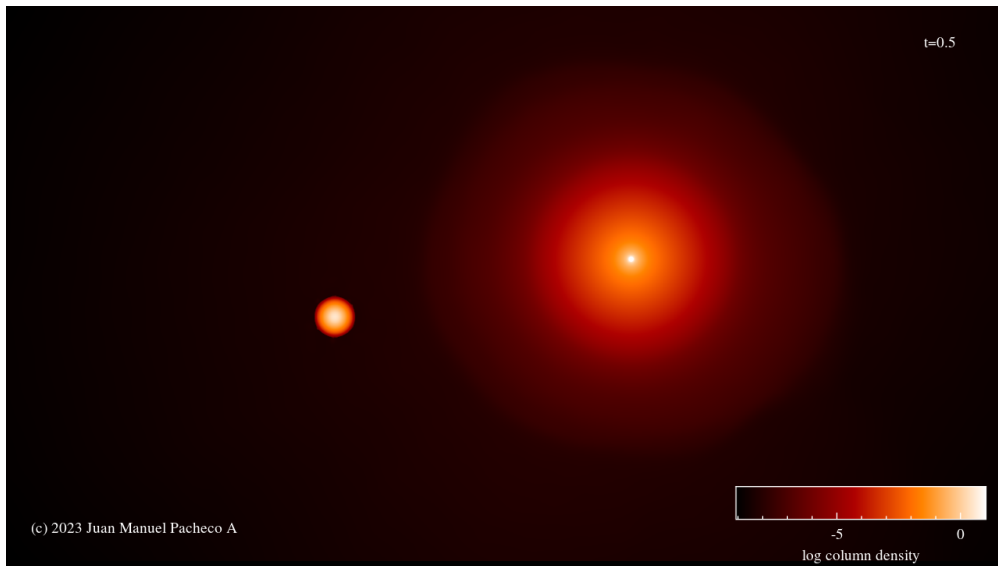
**b = 0.1 R<sub>☉</sub>:** STARSMASHER collision simulation between the MS and CHeB PARSEC profiles of  $42 M_{\odot}$  and  $58 M_{\odot}$  respectively.



*Note.* 2D logarithmic density map for the first output file (`out0001.sph`) of the STARSMASHER collisional routine. The  $x$  and  $y$  axis range from  $-100 R_{\odot}$  to  $100 R_{\odot}$ , with the center of mass as the origin. In this configuration  $d_{init} = 110 R_{\odot}$ ,  $v_{\infty} = 10 \text{ km/s}$  and  $b = 0.1 R_{\odot}$ . The total simulated time was 8.45 days.

**Figure 2.16**

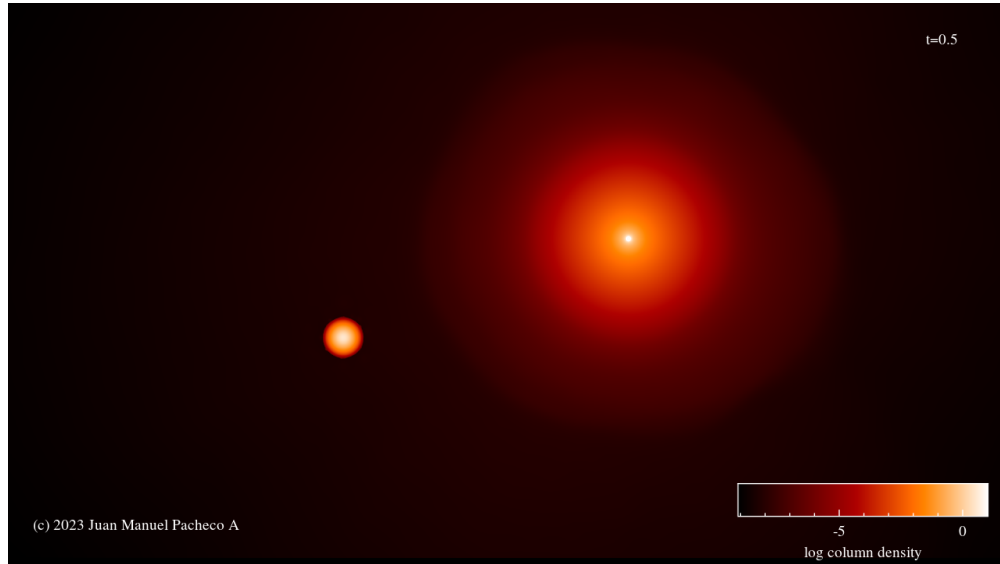
**b = 1 R<sub>☉</sub>:** STARSMASHER collision simulation between the MS and CHeB PARSEC profiles of  $42 M_{\odot}$  and  $58 M_{\odot}$  respectively.



*Note.* 2D logarithmic density map for the first output file (`out0001.sph`) of the STARSMASHER collisional routine. The  $x$  and  $y$  axis range from  $-100 R_{\odot}$  to  $100 R_{\odot}$ , with the center of mass as the origin. In this configuration  $d_{init} = 110 R_{\odot}$ ,  $v_{\infty} = 10 \text{ km/s}$  and  $b = 1 R_{\odot}$ . The total simulated time was 8.14 days.

**Figure 2.17**

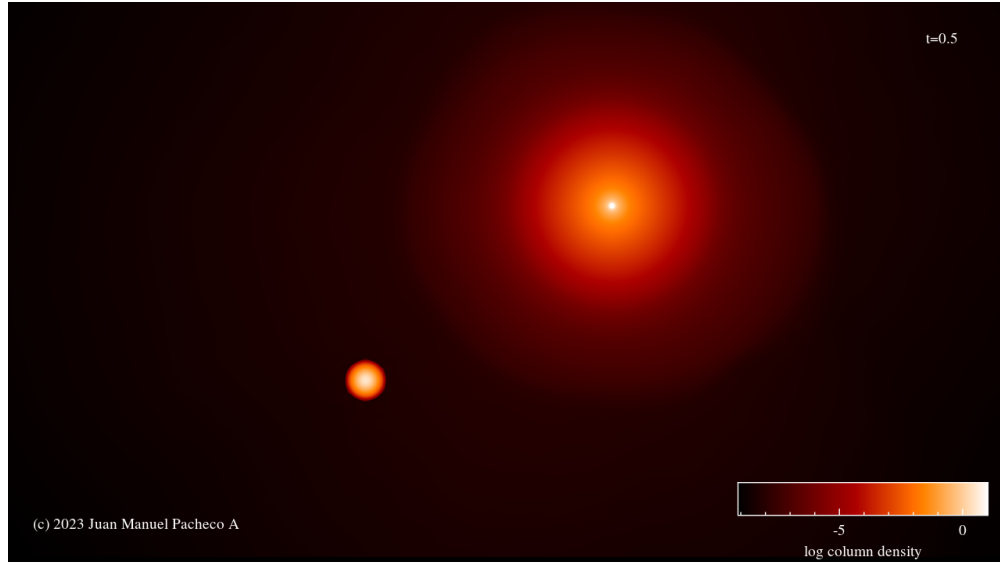
**b = 3 R<sub>☉</sub>:** STARSMASHER collision simulation between the MS and CHeB PARSEC profiles of  $42 M_{\odot}$  and  $58 M_{\odot}$  respectively.



Note. 2D logarithmic density map for the first output file (out0001.sph) of the STARSMASHER collisional routine. The  $x$  and  $y$  axis range from  $-100 R_{\odot}$  to  $100 R_{\odot}$ , with the center of mass as the origin. In this configuration  $d_{init} = 110 R_{\odot}$ ,  $v_{\infty} = 10 \text{ km/s}$  and  $b = 3 R_{\odot}$ . The total simulated time was 12.38 days.

**Figure 2.18**

**b = 10 R<sub>☉</sub>:** STARSMASHER collision simulation between the MS and CHeB PARSEC profiles of  $42 M_{\odot}$  and  $58 M_{\odot}$  respectively.



Note. 2D logarithmic density map for the first output file (out0001.sph) of the STARSMASHER collisional routine. The  $x$  and  $y$  axis range from  $-100 R_{\odot}$  to  $100 R_{\odot}$ , with the center of mass as the origin. In this configuration  $d_{init} = 110 R_{\odot}$ ,  $v_{\infty} = 10 \text{ km/s}$  and  $b = 10 R_{\odot}$ . The total simulated time was 4.33 days.

The methodology employed to determine the characteristics of each collision corresponds to replicating previous studies that analyzed the massive star's encounters for the generation of black holes in the PI mass gap, adding further exploration of the collisional parameters like never before. Traditionally, hydrodynamical simulations of star collisions were restricted to mass ranges below  $40 M_{\odot}$ , and their remnants were analyzed in the context of the generation of Blue stragglers (Costa et al., 2022; Lombardi, Rasio, & Shapiro, 1995). On the other hand, the usual approach to exploring the direct dynamical encounter formation channel is the stellar evolution simulation of the product of these collisions. The remnant is constructed from the homogeneous and controlled addition of mass of the secondary star (ZAMS or MS) into the envelope of the primary star (TAMS or CHeB) imposing that the core of the primary remains unchanged (Ballone et al., 2023; Di Carlo, Mapelli, Giacobbo, et al., 2020; Renzo et al., 2020). This approach assumes naively that no mass is lost during the merger process and the effects of rotation are not included (Renzo et al., 2020). In short, the collisions of massive stars have not been simulated in detail until now, let alone or in the context of PI black hole production.

Each STARSMASHER simulation was assigned a name throughout the development of this thesis (in bold at the beginning of each of visualization) depending on their initial parameters. **Renzo et al. (2020)** is set to mimic the scenario proposed in Renzo et al. (2020), where a primary TAMS star of  $58 M_{\odot}$  collides with a secondary MS star of  $42 M_{\odot}$  in a radial orbit ( $b = 0$ ) and with a velocity that corresponds to the dispersion velocity of stars in young stellar clusters ( $v_{\infty} = 10 \text{ km/s}$ ) (see figure 2.8).  $v_{\infty} = 10 \text{ km/s}$ , mimic the characteristics explained in Di Carlo, Mapelli, Giacobbo, et al. (2020) and also used in Ballone et al. (2023), where the primary star is a CHeB of  $58 M_{\odot}$  and the secondary star is a  $42 M_{\odot}$  MS, both of them colliding with the same orbital parameters as for the Renzo case (see figure 2.12). All the other configurations are variations on a maximum of two parameters with respect to these baseline cases.

**60 TAMS vs 40 ZAMS** only change the Renzo inputs by increasing the mass of the primary TAMS to  $60 M_{\odot}$  and by replacing the secondary for a ZAMS star of  $40 M_{\odot}$  (see figure 2.9). **Half Resolution** use a CHeB primary modeled with half of the SPH particles, while all the other values used in  $v_{\infty} = 10 \text{ km/s}$  remain unchanged (see figure 2.10). **+ 2 Myr** keeps the same configuration as for  $v_{\infty} = 10 \text{ km/s}$  and just replace the secondary for a MS + 2 Myr star of the same mass (see figure 2.11).  $v_{\infty} = 100 \text{ km/s}$  and  $v_{\infty} = 500 \text{ km/s}$  follow the exact same configuration as  $v_{\infty} = 10 \text{ km/s}$  just by increasing the velocity at infinity to  $100 \text{ km/s}$  and  $500 \text{ km/s}$  respectively (see figures 2.13 and 2.14).  $b = 0.1 R_{\odot}$ ,  $b = 1 R_{\odot}$ ,  $b = 3 R_{\odot}$  and  $b = 10 R_{\odot}$  explore the non-radial collisional scenario by keeping the same parameters as in  $v_{\infty} = 10 \text{ km/s}$  but changing the impact parameter to 0.1, 1, 3 and  $10 R_{\odot}$  correspondingly to their names (see figures 2.15, 2.16, 2.17 and 2.18). Finally, all collisions were scheduled to occur after 1 day and the initial separation was fixed for all cases as  $d_{init} = 110 R_{\odot}$ .

In terms of computational costs, each of the collision simulations lasted between 3 and 4 weeks to be completed depending on the available computational resources. The computations performed in this study were set to use 8 CPUs, with 16 tasks per node, and 2 GPUs from the DemoBlack server of the Astronomy and Physics department of the University of Padova.

### 2.3 Entropy sorting

Hydrodynamical simulations are the perfect tool to explore any type of collision between stars. The numerical solution of Euler's equations coupled with the proper treatment of radiation, magnetic fields, EOS, rotation, viscosity, etc. (as described in section 2.2.1), is the only way to determine the precise characteristic of the remnant object after the direct encounter. However, as mentioned in the last paragraph of the previous subsection, the SPH simulations are very expensive in terms of computational resources. The more physical processes are included in the hydrodynamical modeling of stars, the more time is needed to calculate each of the particle properties and the convergence of the numerical integration of the equations can be dramatically affected. Due to this major disadvantage, complementary methodologies have been developed to explore the consequences of stellar collisions without the need for direct calculation of the hydrodynamical equations.

The entropy sorting algorithm is a frequently used approximation in the literature to derive the structure of stars formed after gentle mergers (Ballone et al., 2023; Gaburov et al., 2008; Glebbeek et al., 2013; Lombardi et al., 1995). The central concept behind this method is Archimedes's principle, by which any fluid will redistribute itself, after being taken out of its equilibrium, following the density differences: a fluid element with a greater density than its environment will accelerate downward, while one with a smaller density will be buoyed upward (Gaburov et al., 2008). The hydrostatic equilibrium will be reached again once the density of each fluid element is equal to the density of its environment. In the collisional scenario, the gas inside both stars is at hydrostatic equilibrium until they crash together, after that moment the density of each fluid element will be continuously adjusted in such a way that pressure equilibrium with the environment is achieved. This means that the buoyancy of each gas parcel will be determined by the relation between its pressure and its density, i.e. by its EOS.

For the case of an ideal gas the buoyancy, also known as the entropic variable ( $A$ ), is determined by

$$A = \frac{P}{\rho^\Gamma}, \quad (2.38)$$

where  $\Gamma$  is the adiabatic index. By construction,  $A$  depends directly upon entropy and composition, and it remains constant for each fluid element in the absence of heating and mixing (Gaburov et al., 2008). Equation 2.38 has been successfully used to describe the underlying hydrodynamics of radial collisions among low-mass MS stars (Lombardi et al., 1995; Lombardi, Thrall, Deneva, Fleming, & Grabowski, 2003; J. C. Lombardi Jr et al., 2002) since those stars are well described by a monatomic ideal gas EOS, where  $\Gamma = 5/3$ . In that situation  $\rho = (P/A)^{3/5}$ , meaning that gas elements with lower  $A$  will have greater  $\rho$  at constant  $P$ . Consequently, fluid elements with smaller values of  $A$  sink to the bottom of a potential well, and the  $A$  profile of a star in stable hydrostatic equilibrium increases radially outwards (Gaburov et al., 2008).

Contrary to the low-mass scenario, fluid in high-mass MS stars is described by a mixture of monatomic ideal gas and radiation in thermal equilibrium, as implemented in STARSMASHER. In such cases, the total pressure is computed using equation 2.21, and the specific entropy is

$$s - s_0 = \frac{3}{2} \frac{k}{\mu} \left[ \log \left( \frac{kT}{\rho^{2/3} \mu} \right) + \frac{8}{3} \frac{1-\beta}{\beta} \right] \equiv \frac{3}{2} \frac{k}{\mu} \log A, \quad (2.39)$$

where  $k$  is the Boltzmann constant,  $\mu$  the mean molecular mass,  $s_0$  depends only on composition and  $\beta = P_{\text{gas}}/P_{\text{tot}}$  with  $P_{\text{tot}} = P_{\text{gas}} + P_{\text{rad}}$  (Clayton, 1983). Equation 2.39 defines buoyancy as

$$A = \frac{P_{\text{tot}}}{\rho^{5/3}} e^{\frac{8(1-\beta)}{\beta}}, \quad (2.40)$$

and manipulating expressions 2.39 and 2.40 the expression for density can be establish as

$$\rho = \frac{3k^4}{A^3 \mu^4 a} \frac{1-\beta}{\beta} e^{\frac{8(1-\beta)}{\beta}}, \quad (2.41)$$

where  $a$  is the radiation constant. The relationship shown in equation 2.41 proves that for the high-mass collisional scenario, conserving the adiabatic and no mixing approximation, one expects the different fluid elements of the two stars to rearrange into hydrostatic equilibrium, with  $A$  monotonically increasing outwards (Ballone et al., 2023).

Using the theoretical framework described here the remnant star after the collision of two massive stars can be reconstructed, without the need for the full hydrodynamical simulation, by applying the following entropy sorting algorithm:

1. Run the relaxation routine of STARSMASHER for the two parent stars to transform their 1D stellar evolution profiles into a 3D distribution of SPH particles.
2. Compute the entropic variable  $A$ , using equation 2.40, for the whole set of particles that compound both stars.
3. Generate the new star by sorting the particles of the initial colliding stars in a way such that  $A$  increases monotonically.

Is crucial to remember that this treatment is framed within the assumptions of a gentle merger, where the propagation of shocks is not allowed, as well as the mixing of the particles derived from the rotation induced after the impact (Gaburov et al., 2008). These conditions are unrealistic in the case of stellar collisions and therefore the results obtained from this algorithm should be analyzed with caution and always compared with full hydrodynamic simulations when available. However, previous studies have shown that this methodology allows a very good reconstruction of stellar remnants at a much lower computational cost, facilitating the exploration of the parameter space (Ballone et al., 2023; Gaburov et al., 2008; Glebbeek et al., 2013; Lombardi et al., 1995).

In the development of this thesis, we decided to implement this algorithm to contrast its results with a large set of hydrodynamical simulations of stellar collisions, seeking to establish some correlation that allows its implementation on a large scale intending to reduce the time spent on the generation of candidate remnants for the formation of black holes in the PI mass gap.

### 3. Results

Due to the conditions expected in the core at the end of the life of massive stars, the traditional theory of stellar evolution does not contemplate the existence of black holes in the mass range between 60 and  $120 M_{\odot}$ . This interval, known as the PI mass gap, has been explored thanks to the detection of GWs, concluding that there are at least two black holes, and many more candidates, within the unexpected range. This thesis work explores the possibility of black hole formation, in the PI mass gap, from the collision of two massive stars in the interior of young SC. The results presented here demonstrate that such a formation channel can generate a massive remnant star, with the necessary structure and sufficient mass, to collapse into a  $60 - 120 M_{\odot}$  black hole at the end of its evolution, alleviating the tension between current GW detections and the classical stellar evolution theory.

In this last chapter, we present how the amount of mass lost, at each instant, was computed for the multiple simulations of stellar collisions. The temporal tracking of this quantity allowed us to establish which stellar remnants reached a dynamical equilibrium after the impact. All of the STARSMASHER simulations analyzed here formed a stellar remnant whose mass falls within the range of the PI mass gap, and the largest amount of mass lost after impact was set at  $\sim 19.5 \%$ . The remnants of the collisions were also analyzed to determine their inner dynamics. The mean values of each velocity component, and their standard deviations, were estimated for each of the gravitationally bound SPH particles. This procedure leads us to conclude that stellar collisions with a non-zero impact parameter, will generate stellar remnants that will undergo chemical mixing in their envelopes thanks to angular momentum transfer. This fact can dramatically affect the subsequent stellar evolution of such post-collision products, even preventing them to collapse into a black hole.

This chapter ends with a direct comparison between the results obtained from the hydrodynamic simulations and those derived from the implementation of the entropy sorting algorithm. In collisions where the evolutionary states of both stars are distinguishable, and therefore the thermodynamic properties in their interiors, the construction of the collisional remnant from the ordering of the initial SPH particles was shown to be effective. Post-collisional stars generated from radial buoyancy enhancement share the same structure as those resulting from months-long SPH simulations. In this thesis, we show how the entropy sorting algorithm can even predict a range of possibilities for the total mass of the resulting post-collision star, a fact that will greatly facilitate the exploration of the parameter space for future work on stellar collisions.

### 3.1 Cumulative mass profiles and bound mass

To analyze how the characteristics of the remnant star are affected by the change of collisional parameters, it is first necessary to define which SPH particles compose the post-collisional star in every simulation. At the beginning of each encounter, the SPH particles are clearly associated with one of the two relaxed stars, however as time begins to flow, and both stars begin to approach each other, this clear distinction becomes blurred. What determines whether or not a gas element is part of a star, in the context of hydrodynamical simulations, is the fact that it is gravitationally bound to it. For that reason, the criteria we follow is the one presented in Ballone et al. (2023), where every  $i$ -th SPH particle is considered bound to the remnant if its total specific energy ( $e_i$ ) is negative. Mathematically speaking if, and only if,  $e_i < 0$  is fulfilled. In this simplified approach the computation of  $e_i$  follows the definition

$$e_i = v_{cm,i}^2 + u_i - G \cdot \frac{M_{encl,i}}{d_{cm,i}}, \quad (3.1)$$

where  $G$  is the gravitational constant,  $u_i$  is the specific internal energy,  $v_{cm,i}$  and  $d_{cm,i}$  are the velocity and distance calculated with respect to the total center of mass, and  $M_{encl,i}$  is the total mass enclosed within  $d_{cm,i}$ . This approach assumes a spherical configuration after the impact for the calculation of the potential energy. This assumption is not entirely realistic, especially in areas immediately next to the center of mass and in cases where collisions are non-radial. However, the accurate calculation of the potential energy of each particle considering the contributions of all other particles is excessively slow, even including parallelization processes. Our comparisons allowed us to conclude that the precise calculation differs from the approximation only up to  $d_{cm,1} = 1.5 R_\odot$ , thereafter both results are identically the same. For that reason, the bound criterion implemented in this thesis assumes at first that all particles with  $d_{cm,i} \leq 1.5 R_\odot$  are gravitationally bound to the remnant star, and then equation 3.1 is applied.

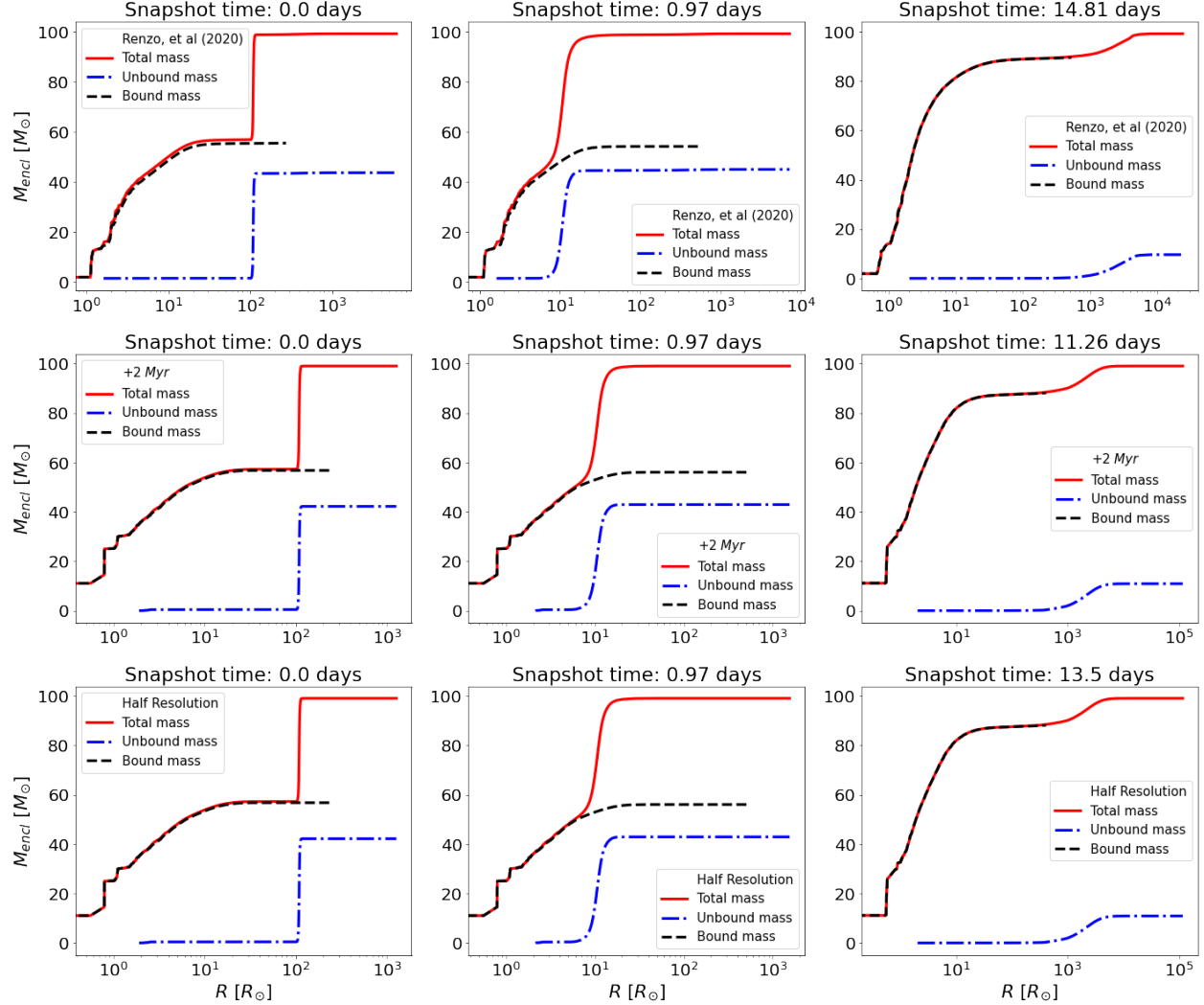
Equation 3.1 is extremely sensible to the determination of the total center of mass ( $cm$ ). By construction, STARSMASHER simulations are programmed to reassign the position of each particle in such a way that the  $cm$  remains constant for all snapshots. This is not true for the physical  $cm$  of collisions, since the motion of stars can vary its position in space. For this reason, the total center of mass used in the calculation of equation 3.1 must be defined following a computational criterion that fits the SPH scheme. The best alternative is to define the  $cm$  of each snapshot as the highest density point (particle). This definition does not apply to the pre-collision analysis of the two stars but ensures that the distance to the center of the remnant is stable once the encounter has occurred. The densest particle within the SPH scheme will represent the central region of the new stellar core.

Following the procedure described in the preceding paragraphs, the bound and unbound mass profiles, along the stellar radius, can be built for any snapshot (see figures from 3.1 to 3.3). The results are in agreement with the expected behavior for all the simulations. At the beginning of the collision (snapshot time: 0 days), only particles modeling the primary star are considered gravitationally bound, while all the particles forming the secondary star are unbound. This can be explained because the core of the most massive star is the densest point of the simulation when the two stars are far from collapsing. The unbound profiles start to grow just when  $R = 110 R_\odot$ , matching the initial separation distance of all collisions. When the collision occurs (snapshot time:

$\sim 1$  days), the bound and unbound particles (basically the two stars) start to mix and the separation distance between them is only the radius of the primary star. In the end, all particles that belong to the remnant star are arranged by increasing radius from the core, and the unbound particles are located at the outer regions of the simulation.

**Figure 3.1**

*Time evolution of the total, bound, and unbound mass profiles for the Renzo, et al. (2020), + 2 Myr and Half Resolution simulations.*

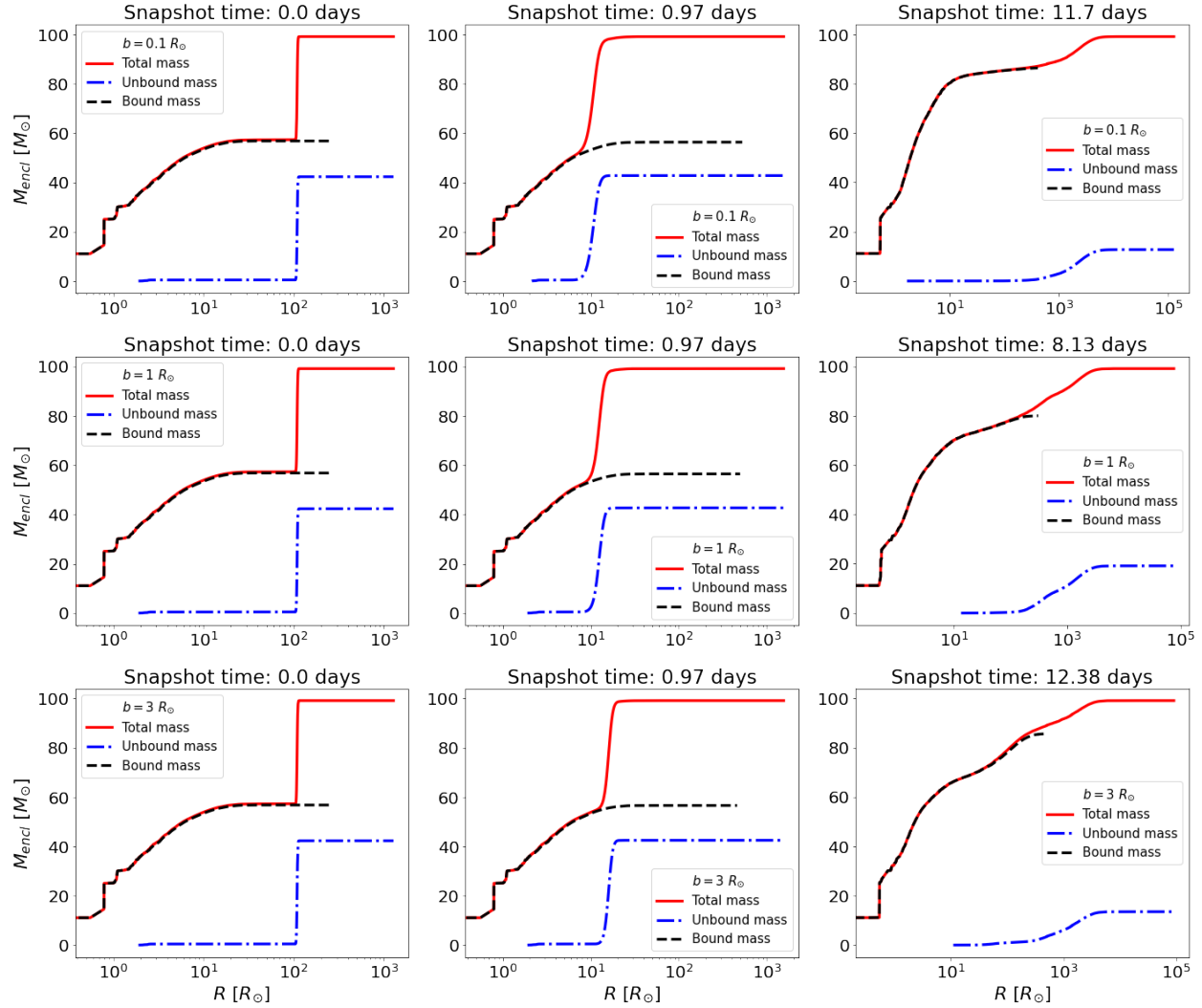


*Note.* Panels from top to bottom: enclosed mass radial profiles for the Renzo, et al (2020), + 2 Myr and Half Resolution simulations respectively. Columns from left to right: different evolutionary stages of the simulations starting from the beginning of the STARSMASHER run, going to the time when the collision occurs, and finishing at the end of each collisional routine. The enclosed mass at each radius ( $M_{\text{encl}}$ ), in  $M_{\odot}$ , is plotted on the  $y$  axis, meanwhile the radius from the instantaneous center of mass of the system, in  $R_{\odot}$ , is plotted on the  $x$  axis. The solid red lines correspond to the mass profiles for the total distribution of SPH particles in each snapshot, the dash-dotted blue lines are the enclosed mass profiles of the unbound particles and the dashed black lines are the bound particle mass profiles at each evolutionary stage. The classification of bound and unbound particles was made following the criteria explained in section 3.1 using equation 3.1.

The total specific energy of the particles ejected from the remnant star increases as a result of linear momentum transfer upon collision and shock propagation. These two processes are responsible for the increase in the kinetic and internal specific energy of the unbound particles, allowing them to escape the gravitational attraction of the new star.

**Figure 3.2**

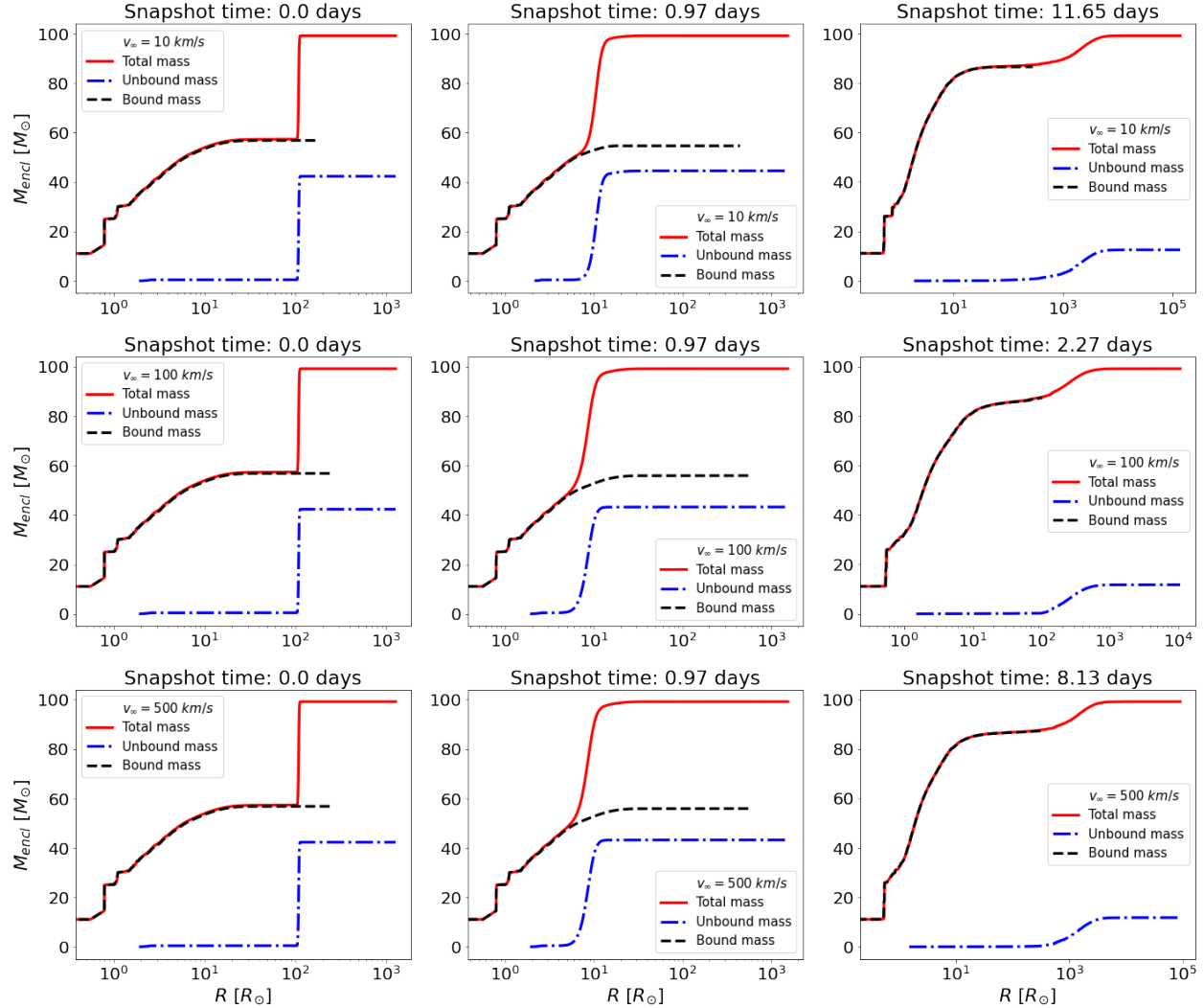
*Time evolution of the total bound, and unbound mass profiles for the  $b = 0.1 R_\odot$ ,  $b = 1 R_\odot$  and  $b = 3 R_\odot$  simulations.*



*Note.* Panels from top to bottom: enclosed mass radial profiles for the  $b = 0.1 R_\odot$ ,  $b = 1 R_\odot$  and  $b = 3 R_\odot$  simulations respectively. Columns from left to right: different evolutionary stages of the simulations starting from the beginning of the STARSMASHER run, going to the time when the collision occurs, and finishing at the end of each collisional routine. The enclosed mass at each radius ( $M_{encl}$ ), in  $M_\odot$ , is plotted on the  $y$  axis, meanwhile the radius from the instantaneous center of mass of the system, in  $R_\odot$ , is plotted on the  $x$  axis. The solid red lines correspond to the mass profiles for the total distribution of SPH particles in each snapshot, the dash-dotted blue lines are the enclosed mass profiles of the unbound particles and the dashed black lines are the bound particle mass profiles at each evolutionary stage. The classification of bound and unbound particles was made following the criteria explained in section 3.1 using equation 3.1.

**Figure 3.3**

*Time evolution of the total bound, and unbound mass profiles for the  $v_\infty = 10 \text{ km/s}$ ,  $v_\infty = 100 \text{ km/s}$  and  $v_\infty = 500 \text{ km/s}$  simulations.*



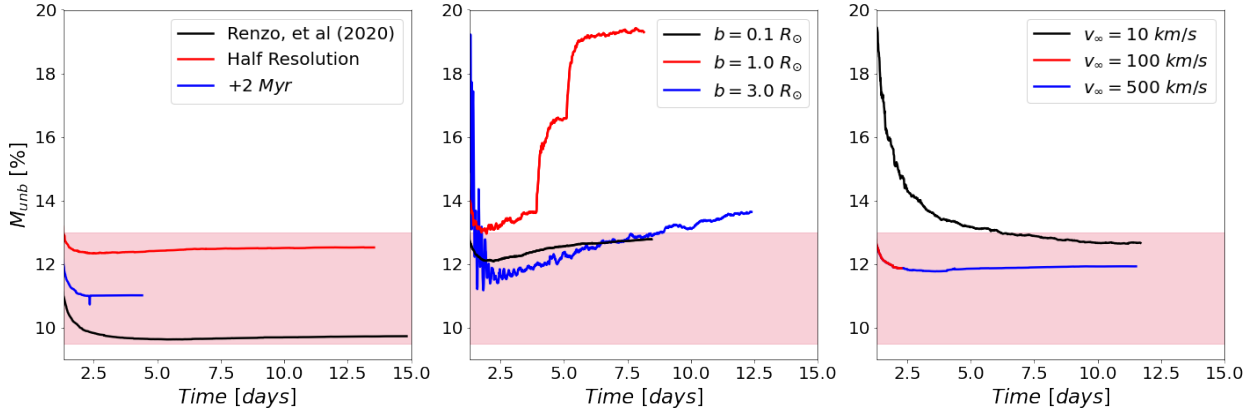
*Note.* Panels from top to bottom: enclosed mass radial profiles for the  $v_\infty = 10 \text{ km/s}$ ,  $v_\infty = 100 \text{ km/s}$  and  $v_\infty = 500 \text{ km/s}$  simulations respectively. Columns from left to right: different evolutionary stages of the simulations starting from the beginning of the STARSMASHER run, going to the time when the collision occurs, and finishing at the end of each collisional routine. The enclosed mass at each radius ( $M_{\text{encl}}$ ), in  $M_\odot$ , is plotted on the  $y$  axis, meanwhile the radius from the instantaneous center of mass of the system, in  $R_\odot$ , is plotted on the  $x$  axis. The solid red lines correspond to the mass profiles for the total distribution of SPH particles in each snapshot, the dash-dotted blue lines are the enclosed mass profiles of the unbound particles and the dashed black lines are the bound particle mass profiles at each evolutionary stage. The classification of bound and unbound particles was made following the criteria explained in section 3.1 using equation 3.1.

After the generation and analysis of the mass profiles, the bound-unbound selection criterion was applied to compute the percentage of unbound mass ( $M_{\text{unb}}$ ) for each step in the time evolution of the collisions (see figure 3.4). This quantity remains stable after the collision for most of the simulations analyzed here, only those configurations where  $b \neq 0$  present alterations in their  $M_{\text{unb}}$

after the first impact.

**Figure 3.4**

*Time evolution of the unbound mass percentage for all the STARSMASHER collision simulations.*



*Note.* The time evolution for the unbound mass percentage is grouped into three different sets to improve visibility. Each column from left to right: Renzo, et al (2020), Half Resolution and  $+ 2 \text{ Myr}$ , then all the set of  $b = 0.1, 1$  and  $3 R_{\odot}$  and finally all simulations computed with velocity changes  $v_{\infty} = 10, 100$  and  $500 \text{ km/s}$ . The unbound mass at each time step ( $M_{unb}$ ), in %, is plotted on the  $y$  axis, meanwhile the time, in days, is plotted on the  $x$  axis. The solid black lines correspond to the unbound mass profiles for Renzo, et al (2020),  $b = 0.1 R_{\odot}$  and  $v_{\infty} = 10 \text{ km/s}$ . The solid red lines correspond to the unbound mass profiles for Half Resolution,  $b = 1 R_{\odot}$  and  $v_{\infty} = 100 \text{ km/s}$ . The solid blue lines correspond to the unbound mass profiles for  $+ 2 \text{ Myr}$ ,  $b = 3 R_{\odot}$ , and  $v_{\infty} = 500 \text{ km/s}$ . Finally, the crimson-shaded square in each graph represents the interval of unbound mass ranging from 9.5 % to 14 %, where almost all the simulations are located at the end of the STARSMASHER collisional routine.

For radial collisions ( $b = 0$ ) we can conclude that the dynamical relaxation process, following the direct dynamical encounter, occurs efficiently. Excluding  $v_{\infty} = 10 \text{ km/s}$ , the  $M_{unb}$  of each radial collision simulation remains unchanged after 4 days. The discrepancies in the value at which this profile stabilizes are associated with the different evolutionary stages of the stars in each simulation. The Renzo et al. (2020) case, which presents the lowest percentage of mass loss, is the only one of those analyzed here with a primary star in TAMS; all the others modeled the most massive star as a CHeB. The increase of  $+ 2 \text{ Myr}$  in the evolution of the secondary star also resulted in a small variation of the final value of  $M_{unb}$ . These fluctuations are understood because each evolutionary stage determines the stellar size. Larger stars have less gravitationally bound envelopes, and vice versa. This is a key factor in the amount of mass the remnant star can inherit after the collision.

For  $b = 0.1, 1$  and  $3 R_{\odot}$  (middle panel of figure 3.4) the percentage of unbound mass is not constant.  $b = 0.1 R_{\odot}$  and  $b = 3 R_{\odot}$  experience gradual  $M_{unb}$  increases over time, with a few minor disturbances. The  $b = 1 R_{\odot}$  is more dramatic, its percentage of mass lost is almost double compared to the other simulations, and its increase is not gradual, it occurs in sharp jumps every few days. These peaks in the  $M_{unb}$  profile are associated with successive collisions of the primary and secondary stellar nuclei. Due to the conservation of angular momentum, the non-radial colli-

sions may experience a phase, after the first impact, where the cores of the primary stars orbit a common point without fully merging. During this period, and thanks to the dissipation of energy, these nuclei can collide more than once until they merge completely. These successive collisions produce the propagation of shocks along the remnant star, detaching its farthest layers.

The percentage of mass lost at the end of the simulation is what will determine the final mass of the stellar remnant. Looking at the plot 3.4 we can notice that all simulations, except  $b = 1$  and  $b = 3$ , have the last value of their  $M_{unb}$  profiles within the range of values from 9.5 % to 13 % (all lines end inside the crimson rectangle). Looking at the table 3.1 this can be seen much clearer, changes in evolutionary state, numerical resolution, or impact velocity all lead to the same amount of mass lost within about 3.5 %. Only by changing the impact parameter one can attain a substantially larger mass loss, greatly affecting the post-collisional dynamics. Low values of  $b$  ( $b < 0.1 R_\odot$ ) do not generate dramatic changes concerning the radial cases, medium values ( $b \sim 1 R_\odot$ ) generate a final remnant with a high dynamic relaxation time and a percentage of mass lost that can double the typical cases. Finally, high values of  $b$  ( $b > 3 R_\odot$ ) can result in the formation of a system that never generates a remnant star, but rather an orbiting system with a common envelope.

These hydrodynamical simulations highlight the crucial role of the periastron separation in the development of massive star collisions, a result whose importance should be highlighted. First of all, perfectly radial collisions ( $b = 0$ ) have almost zero probability of occurring in the universe, let alone in environments like the young SC. Second of all, at the moment all the works that analyze stellar collisions as a black hole formation channel in the PI mass gap, assume that radial collisions are the most violent possible scenario, and therefore, those that determine the maximum limit of mass loss [Ballone et al. \(2023\)](#); [Di Carlo, Mapelli, Giacobbo, et al. \(2020\)](#); [Renzo et al. \(2020\)](#), which is demonstrably not the case.

**Table 3.1**

*Final percentage of unbound mass, and predicted remnant mass, for each of the simulated STARSMASHER collisions.*

Simulation	$M_{unb}$ [%]	$M_{remnant}$ [ $M_\odot$ ]
Renzo, et al (2020)	9.73	89.82
Half Resolution	12.52	87.48
+ 2 Myr	11.01	88.54
$b = 0.1 R_\odot$	12.78	86.78
$b = 1 R_\odot$	19.30	80.30
$b = 3 R_\odot$	13.64	86.36
$v_\infty = 10 km/s$	12.66	87.34
$v_\infty = 100 km/s$	11.87	87.69
$v_\infty = 500 km/s$	11.93	87.63

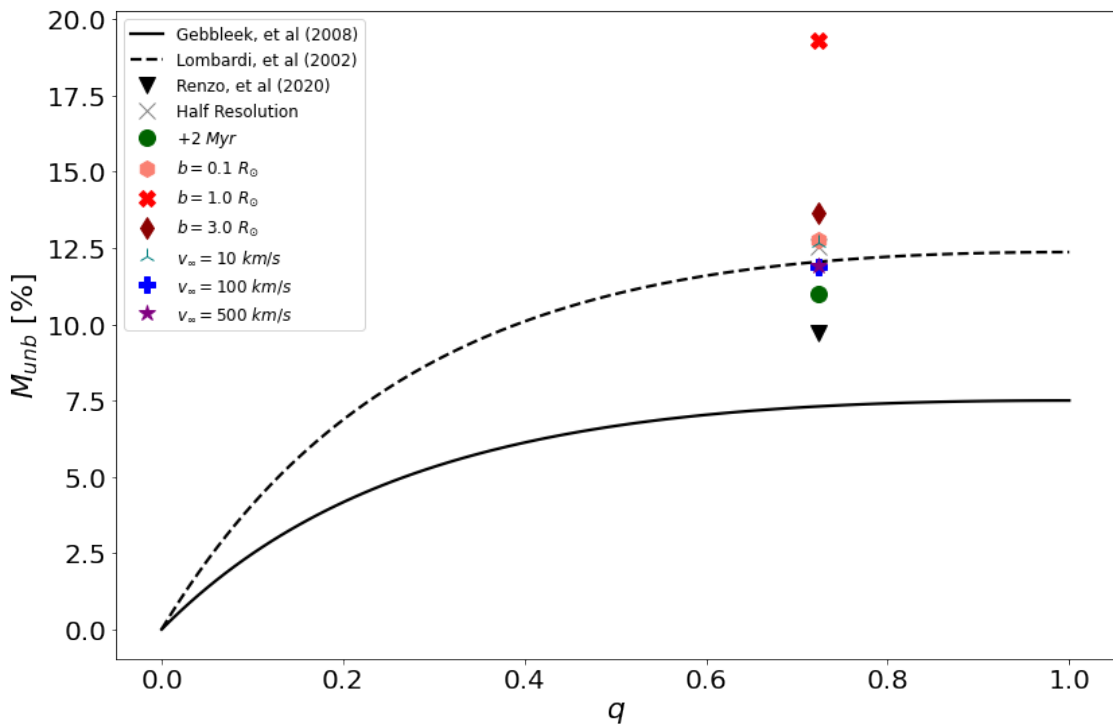
*Note.* Columns from left to right: simulation name, final unbound mass percentage, and stellar remnant mass in  $M_\odot$ .

Despite the possibly large amount of mass lost, looking at the third column of the table 3.1 we

can conclude that all simulations formed a remnant with a mass within the PI mass gap, and quite far from its lower limit ( $60 M_{\odot}$ ). This is a result in favor of the massive star collisions formation channel, the necessary mass quota is met for all variations explored in this work. Unless the post-collisional star suffer a dramatic mass loss ( $> 20 M_{\odot}$ ) before the gravitational collapse, each of these collisions could form a black hole within the PI mass gap.

**Figure 3.5**

*Expected semi-analytical mass loss in the stellar collisional scenario Vs computed mass loss by the STARSMASHER simulation scheme.*



*Note.* The unbound mass percentage ( $M_{unb}$  in % units) is plotted on the  $y$  axis, meanwhile, the  $x$  represents all possible values for the  $q$  parameter, defined as the ratio between the mass of the secondary star and the mass of the primary star involve the collision ( $q = M_2/M_1$ ). The solid and dashed black lines correspond to the expected mass loss after a collision of two stars as a function of  $q$ , following the semi-analytical prescriptions introduced in Glebbeek and Pols (2008) and J. C. Lombardi Jr et al. (2002) respectively (equations 3.3 and 3.2). The markers represent the unbound mass for the last snapshot in each STARSMASHER simulation, determined by the bound-unbound criteria described in section 3.1. The  $q$  value for all simulations is essentially the same because in all configurations  $M_2 \sim 42$  and  $M_1 \sim 58$ .

Finally, it is important to compare these results with other estimates of mass loss in stellar collisions. Due to the lack of experiments with hydrodynamical simulations in this area, some authors have proposed semi-analytical models that allow the estimation of this quantity from the essential characteristics of the colliding stars. This is the case of the formula proposed by J. C. Lombardi Jr et al. (2002), where the  $M_{unb}$  can be modeled as

$$M_{unb} = C_1 \cdot \frac{q}{(1+q)^2} \cdot \frac{R_{1,86} + R_{2,86}}{R_{1,50} + R_{2,50}}, \quad (3.2)$$

where  $q = M_2/M_1$ ,  $C_1 = 0.157$  and  $R_{n,86}$  and  $R_{n,50}$  are the radii containing 86 % and 50 % of the mass of parent star  $n$  (1 for the primary and 2 for the secondary). This equation is suited for radial collisions between low-mass stars and was calibrated using very precise hydrodynamical simulations. Glebbeek and Pols (2008) proposed a simplified alternative to the equation 3.2, that also works in the radial low-mass collisional scenario, where

$$M_{unb} = C_2 \cdot \frac{q}{(1+q)^2}, \quad (3.3)$$

here  $C_2 = 0.3$ .

Figure 3.5 shows the comparison of the unbound mass percentages obtained from the STARS-MASHER simulations and the values predicted by equations 3.2 and 3.3. In this case, all collisions were set with the same mass values for the primary and secondary star and therefore all have the same  $q = 0.72$ . The simplified Geebleck model fits our results better and predicts a very similar mass loss in almost all cases, only the  $b = 1 R_\odot$  simulation deviates quite far from this paradigm. This discrepancy is expected since this model does not consider non-radial collisions and it is impressive that it is still close to the simulated values of  $b = 0.1 R_\odot$  and  $b = 3 R_\odot$ . Apart from the above, equation 3.3 was calibrated for low-mass stars, so its ability to predict values in massive collisions, as in this case, is something that should be highlighted and that allows the extension of this formula for any type of encounter regardless of the mass. For our sample of simulations equation 3.2 does not work properly.

### 3.2 Rotational evolution of the remnant

The mass of the remnant, although it is one of the essential characteristics that allow it to meet the requirements to form a black hole in the PI mass gap, should not be the only property to be analyzed. Many other factors can influence the evolutionary process of the post-collisional star, preventing its gravitational collapse. For this reason, in this study, we analyze the dynamics of the SPH particles that model each collisional remnant, intending to identify possible alterations in its chemical and structural composition.

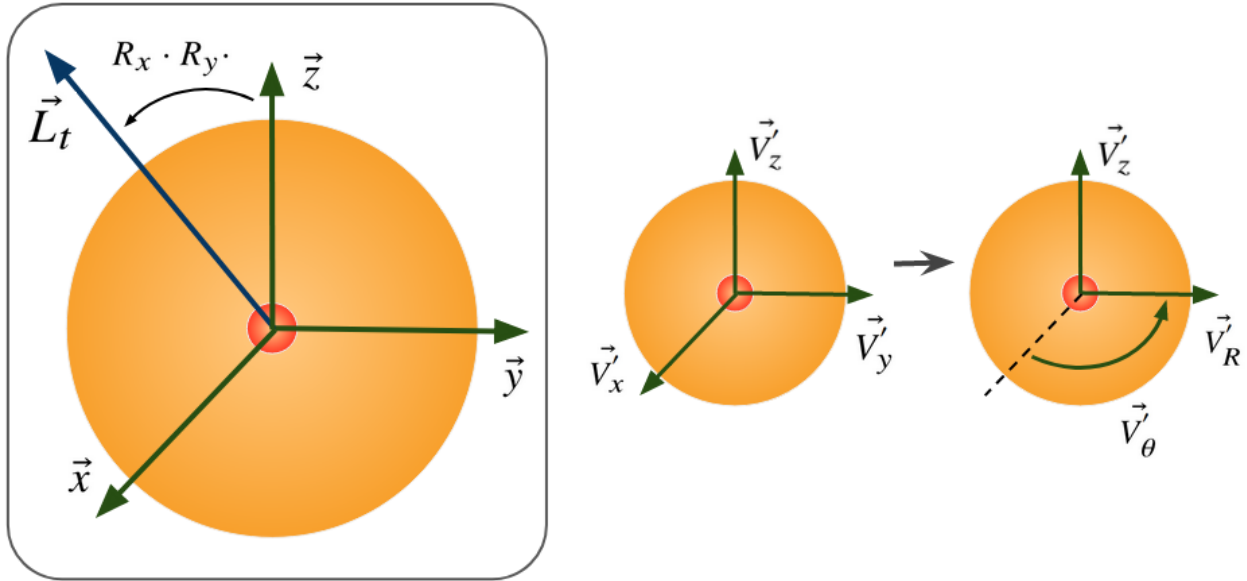
The reference frame from which all bound SPH particle velocities were computed, was constructed from the total angular momentum ( $\vec{L}_t$ ) of the ensemble. The process consisted of determining the rotation axis of the remnant star using the velocities and positions stored in each snapshot of the simulations. Then, by applying two rotation transformations on the  $y$ -axis and  $x$ -axis respectively (rotation matrixes  $R_x$  and  $R_y$ ), the  $z$ -coordinate axis was aligned with  $\vec{L}_t$  (see the scheme inside the gray box in figure 3.6). From this point on, the velocities of each bound particle were rewritten in a cylindrical coordinate system ( $\vec{V}_R$ ,  $\vec{V}_\theta$  and  $\vec{V}_z$ ) that allows a more intuitive and direct interpretation of what is happening inside the remnant star (see figure 3.6).

The time evolution of the mean values, considering all SPH bound particles, for the radial ( $V_R$ ), tangential ( $V_\theta$ ) and vertical ( $V_z$ ) velocity components was computed for the whole set of STARS-MASHER simulations (see figure 3.7). The behavior of each of these values, and the description of the internal dynamics of the post-collisional star, can be grouped into two. The radial collisions ( $b = 0$ ), presented in the top and bottom panel of figure 3.7, exhibit a velocity profile where  $V_R$

is the dominant component (solid black lines). The mean values of  $V_\theta$  and  $V_z$  oscillate around 0 km/s (blue and red solid lines respectively), indicating that there is no net rotation or net vertical motion within the SPH star. The radial translation of the whole set of particles is explained by the transfer of linear momentum upon collision, and their natural decay in time is explained by the energy loss processes considered in STARSMASHER.

**Figure 3.6**

*Construction of the coordinate system aligned with the spin axis of the remnant star, and its subsequent change to a cylindrical coordinate system.*



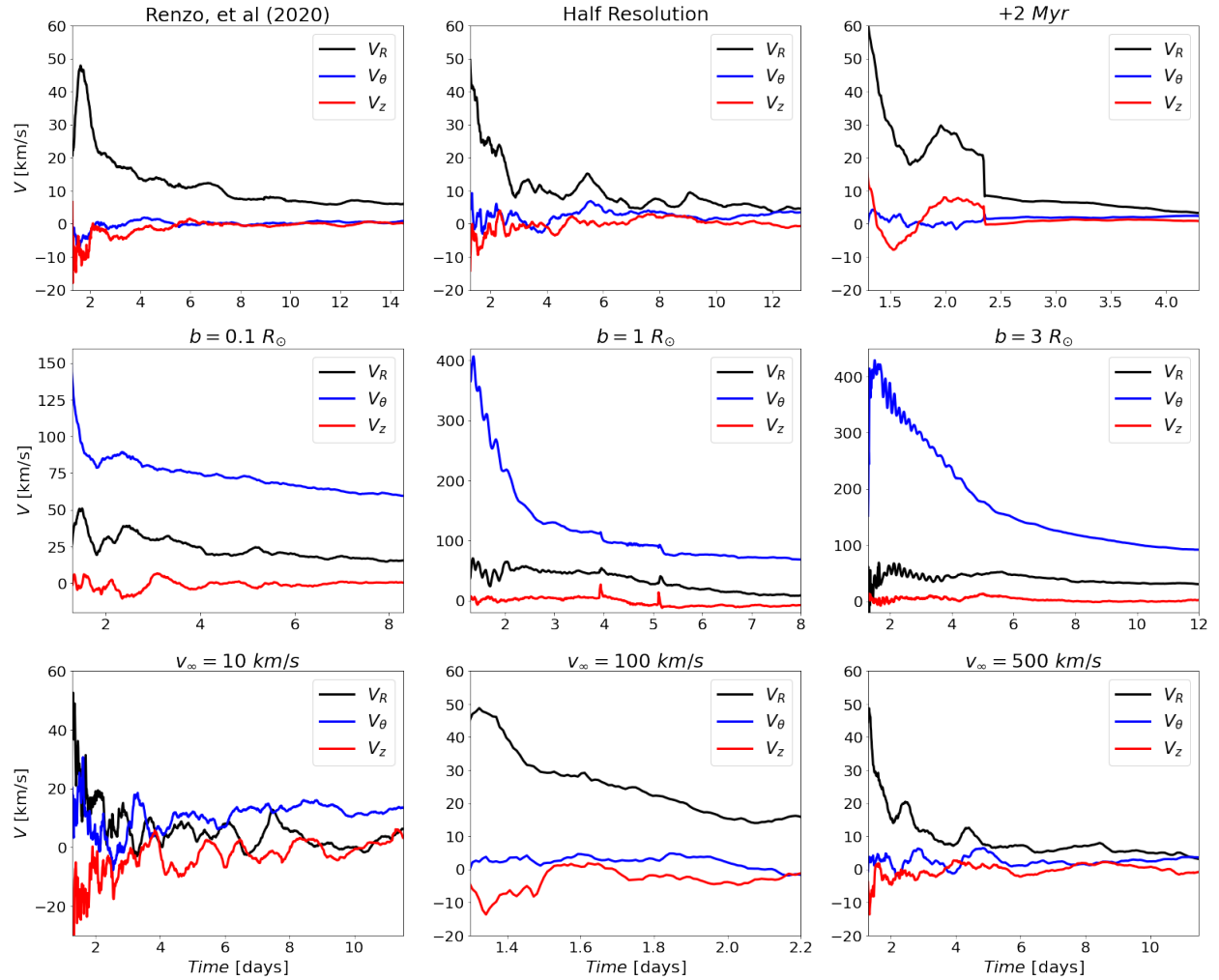
*Note.* The large orange circle represents the envelope of the remnant star, while the small reddish circle represents its core. In the framed drawing inside the gray box, the dark blue vector represents the total angular momentum of the particles that compose the star ( $\vec{L}_t$ ), while the green vectors demarcate the directions of the default coordinate axis in STARSMASHER ( $x$ ,  $y$  and  $z$ ). Applying the rotation matrices on  $y$  and  $x$  ( $R_x \cdot R_y \cdot$ ) constructs the primed reference frame ( $x'$ ,  $y'$  and  $z'$ ) whose  $z'$  axis is aligned with  $\vec{L}_t$ . This process is represented by the curved black vector. To the right of the gray square is exemplified the process of changing coordinates from the primed system of velocities ( $V'_x$ ,  $V'_y$  and  $V'_z$ ) to the cylindrical system ( $V'_R$ ,  $V'_\theta$  and  $V'_z$ ).

The case of non-radial collisions ( $b \neq 0$ ), located in the middle panel of the figure 3.7, is much more interesting. In this type of collision, the predominant component over time is  $V_\theta$ , exceeding  $V_R$  at each instant.  $V_z$  continues to oscillate around 0 km/s so that the net vertical motion of the remnant star is again ruled out. In this case, the net rotation of the particles modeling the post-collisional star arises due to the transfer of angular momentum upon collision (see figure 3.9). This is an extremely interesting fact since it can promote chemical mixing within the envelope of the star, radically changing all its subsequent evolution (Ballone et al., 2023; Costa et al., 2022; Di Carlo, Mapelli, Giacobbo, et al., 2020; Renzo et al., 2020). In addition, these velocity profiles present peaks common to all velocity components at certain time instants. This is strong evidence in favor of the orbital scenario of the nuclei of the parent stars, which derives in collisions after the first impact and that we saw also appear in the unbound mass profiles. Finally, it is very important

to emphasize that the mean values of the velocity components presented here are within the range of the values reported by other authors who have explored the stellar collision scenario using SPH simulations (Sills, Faber, Lombardi Jr, Rasio, & Warren, 2001).

**Figure 3.7**

*Time evolution of the mean velocity components of all SPH particles involved in the collision simulations.*



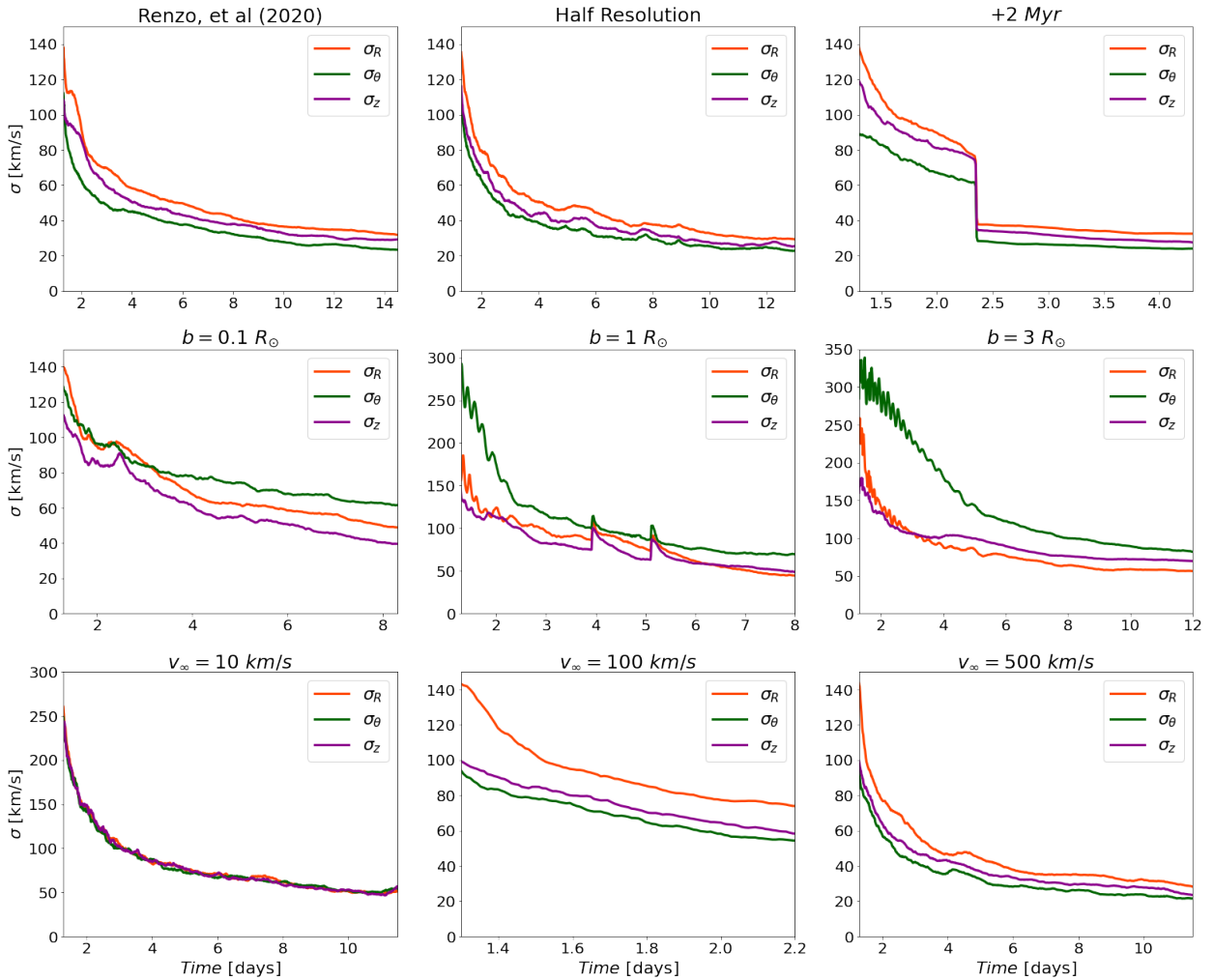
*Note.* In each square the mean velocity ( $V$ ) is plotted on the  $y$  axis, in  $km/s$  units. The  $x$  axis is the equivalent simulated time, in days. At the top panel, from left to right, the visualized collision simulations are Renzo, et al (2020), Half Resolution, and + 2 Myr. At the medium panel, from left to right:  $b = 0.1 R_{\odot}$ ,  $b = 1 R_{\odot}$  and  $b = 3 R_{\odot}$ . The bottom panel, from left to right:  $v_{\infty} = 10 km/s$ ,  $v_{\infty} = 100 km/s$  and  $v_{\infty} = 500 km/s$ . The black, blue, and red solid lines represent the mean velocities components for all the SPH particles in each snapshot: radial ( $V_R$ ), tangential ( $V_{\theta}$ ), and vertical ( $V_z$ ), respectively.

The time evolution of the standard deviation values for the radial ( $\sigma_R$ ), tangential ( $\sigma_{\theta}$ ) and vertical ( $\sigma_z$ ) velocity components was also computed for the whole set of STARSMASHER simulations (see figure 3.8). In this case, all the conclusions drawn from the velocity profiles also apply. The only predominant difference is that the profiles of the standard deviations are not so far apart be-

tween components for all configurations. Only the cases  $b = 1 R_\odot$  and  $b = 3 R_\odot$  exhibit a clear differentiation of  $\sigma_\theta$  over the others. This is explained due to the high values of  $V_\theta$  shown by the particles resulting from the repeated subsequent collisions.

**Figure 3.8**

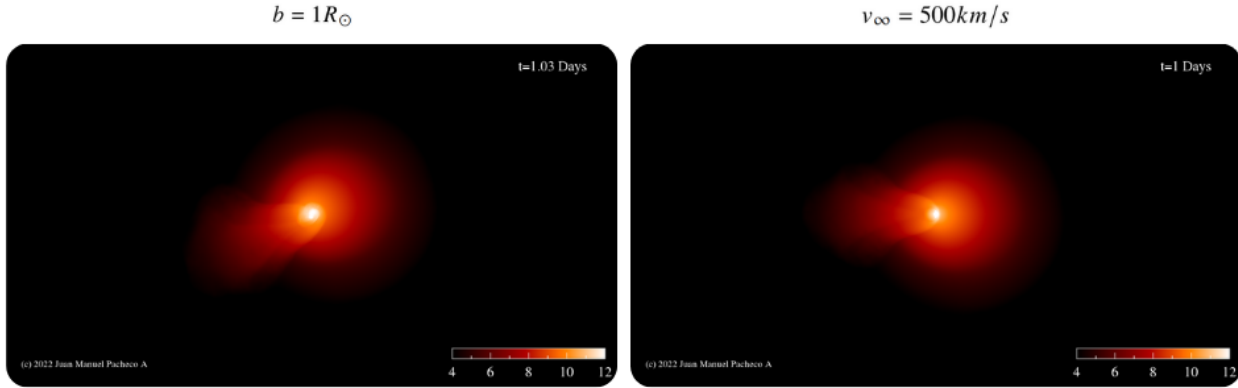
*Time evolution of the standard deviation for each velocity component of all SPH particles involved in the collision simulations.*



*Note.* In each square the standard deviation ( $\sigma$ ) is plotted on the  $y$  axis, in  $km/s$  units. The  $x$  axis is the equivalent simulated time, in days. At the top panel, from left to right, the visualized collision simulations are Renzo, et al (2020), Half Resolution, and + 2 Myr. At the medium panel, from left to right:  $b = 0.1 R_\odot$ ,  $b = 1 R_\odot$  and  $b = 3 R_\odot$ . The bottom panel, from left to right:  $v_\infty = 10 km/s$ ,  $v_\infty = 100 km/s$  and  $v_\infty = 500 km/s$ . The orange, green, and purple solid lines represent the standard deviation for each velocity component for all the SPH particles in each snapshot: radial ( $\sigma_R$ ), tangential ( $\sigma_\theta$ ), and vertical ( $\sigma_z$ ), respectively.

**Figure 3.9**

*Comparison of impact instants between a non-radial collision ( $b = 1 R_{\odot}$ ) and a radial collision ( $v_{\infty} = 500 \text{ km/s}$ ).*



*Note.* 2D logarithmic density map for the direct encounter (out0105.sph) of the  $b = 1 R_{\odot}$  and  $v = 500 \text{ km/s}$  STARSMASHER collisional routines. The  $x$  and  $y$  axis range from  $-100 R_{\odot}$  to  $100 R_{\odot}$ , with the center of mass as the origin. It can be clearly distinguished how the particles that are part of the non-radial collision simulation start to rotate upon impact, while the particles of the radial collision do not exhibit this behavior.

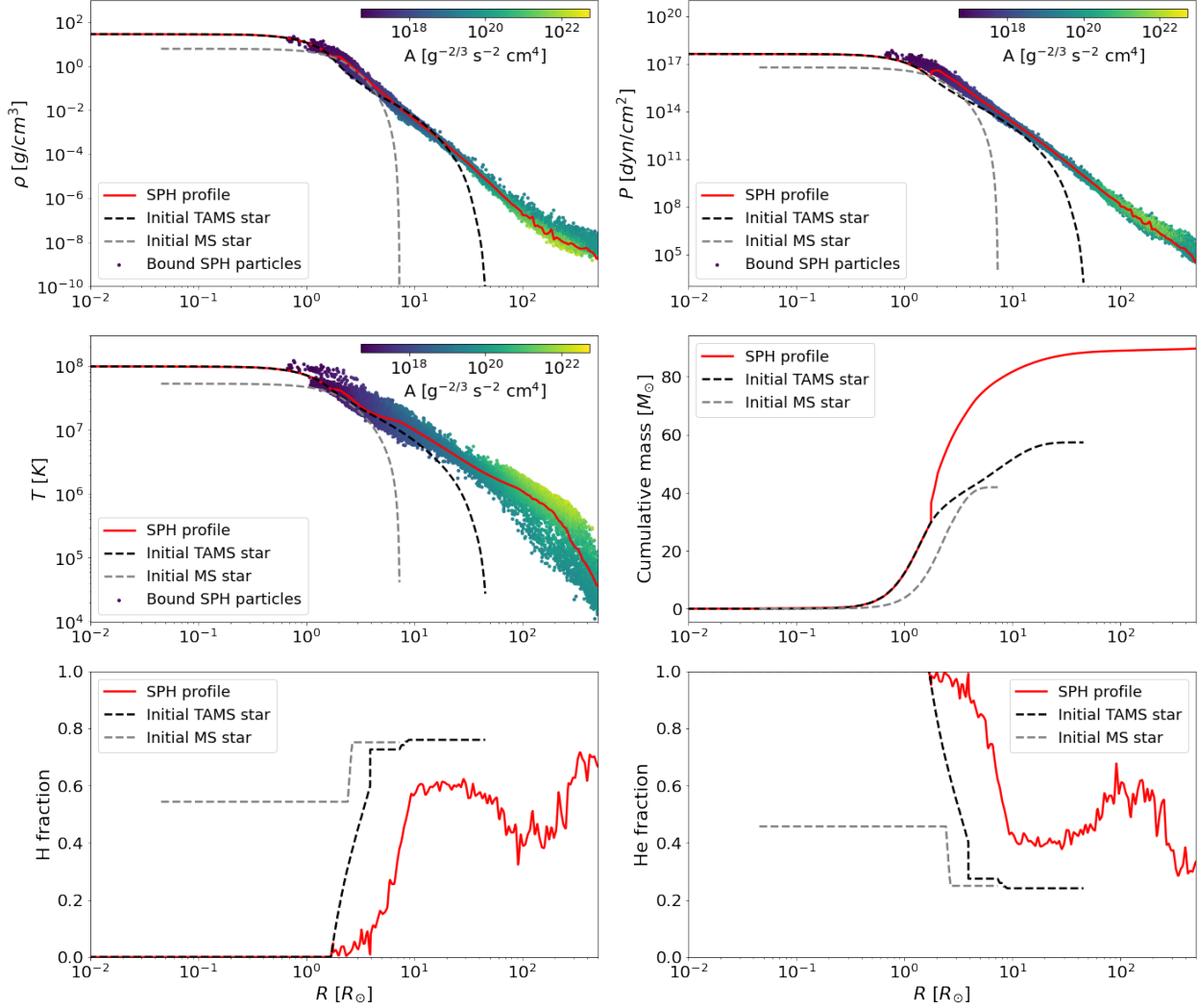
### 3.3 Hydrodynamics Vs Entropy

Having completed the dynamical analysis of the particles that make up our set of remnant stars, we can begin to study in more detail the stellar structure of each post-collisional star. To achieve this goal, radial profiles of density ( $\rho$ ), pressure ( $P$ ), temperature ( $T$ ), cumulative mass, and hydrogen and helium fractions were generated from the bound particles of the last snapshot for each STARSMASHER simulation. The profiles constructed from the SPH particles were in turn directly compared to the initial radial profiles, generated from the input files of the stellar evolution codes, of the parent stars of each collision (see figures from 3.10 to 3.18).

The first thing that stands out from the comparison between the initial profiles, and the profile of each collisional remnant, is that the  $\rho$ ,  $P$ , and  $T$  after the collision are almost identical to those of the initial stars. The profiles constructed from the interpolation of the mean values of these properties for the SPH particles (solid red lines in figures 3.10 to 3.18) follow the behavior expected from the sum of the two profiles constructed with PARSEC (black and gray dashed lines in figures 3.10 to 3.18)). The only radical difference is marked in their radial extensions, since the particles gravitationally bound to the remnant reach much larger radii than the initial ones, as would be expected from this scenario. This agreement corroborates that the modeling performed in the relaxation and collision routines by STARSMASHER preserves the main properties of the stars generated from the stellar evolution codes. This is a fact to note since the treatment of EOS within the SPH scheme is much more simplified (see section 2.2.1) than in codes such as PARSEC and MESA. The physical assumptions adopted in the hydrodynamical simulations of massive star collisions work, even under thermodynamically changing conditions (e.g., post-impact shock propagation).

**Figure 3.10**

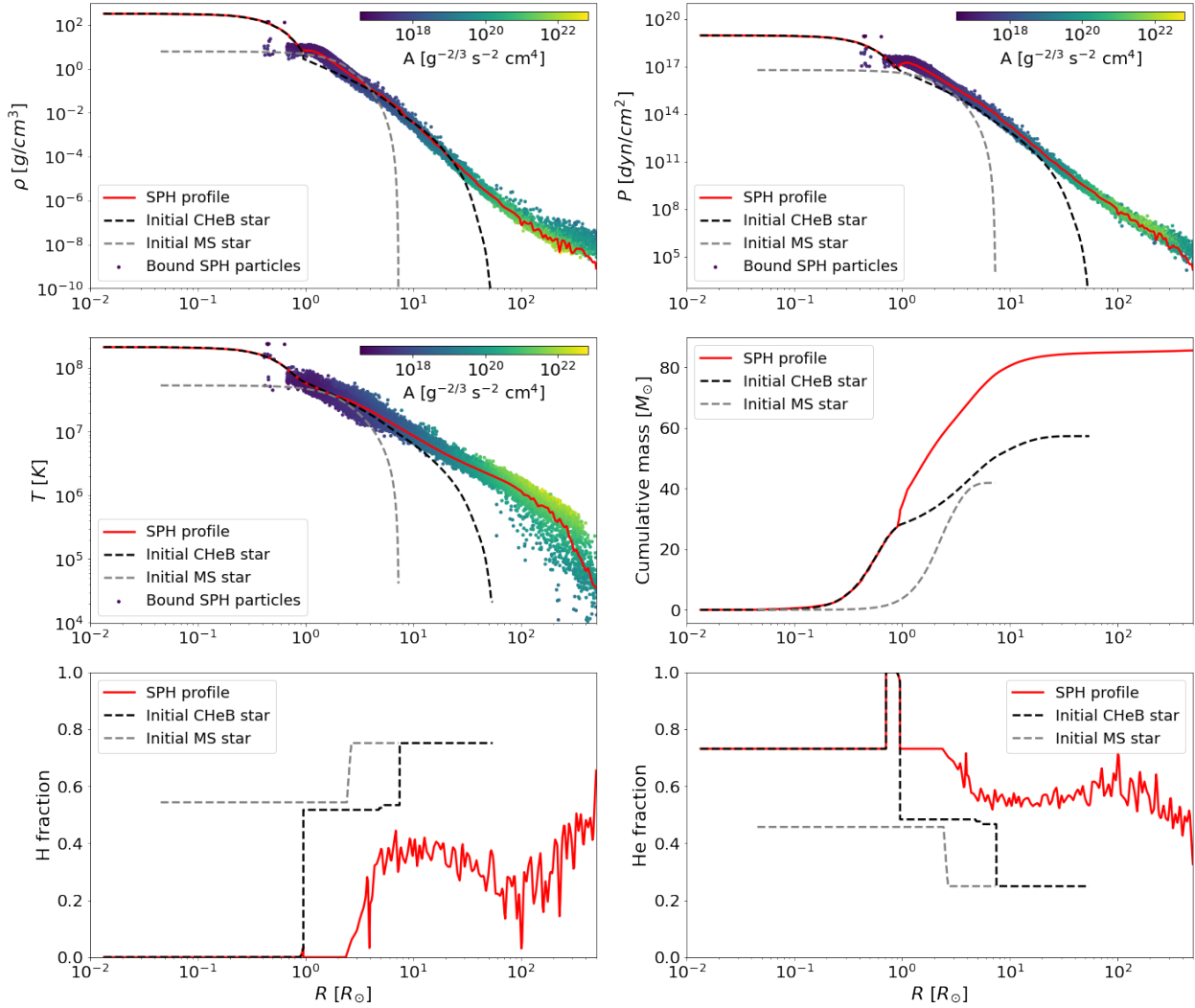
Radial profiles of the main stellar properties for the remnant star of the Renzo, et al (2020) collision simulation.



*Note.* At the top panel, from left to right: density profile ( $\rho$ ) in  $g/cm^3$ , and pressure ( $P$ ) profile in  $dyn/cm^2$ , both of them along the stellar radius in  $R_\odot$ . At the medium panel, from left to right: temperature profile ( $T$ ) in  $K$ , and cumulative mass profile in  $M_\odot$ , both of them along the stellar radius in  $R_\odot$ . At the bottom panel, from left to right: hydrogen fraction and helium fraction, along the stellar radius in  $R_\odot$ . The red solid lines represent the SPH profile obtained after interpolating the average values obtained in the radial binning of all the particles in the final snapshot of the simulation. The dashed black lines represent the input stellar profile for the primary star at TAMS produced by PARSEC and described in section 2.1.1. The dashed gray lines represent the input stellar profile for the secondary star at MS produced by PARSEC and described in section 2.1.1. For the density, pressure, and temperature profiles, the colored dots are the bound SPH particles, ordered by increasing distance to the center of the simulation. They are colored by their entropic variable ( $A$ ), in  $g^{-2/3}s^{-2}cm^4$ , calculated using equation 2.40.

**Figure 3.11**

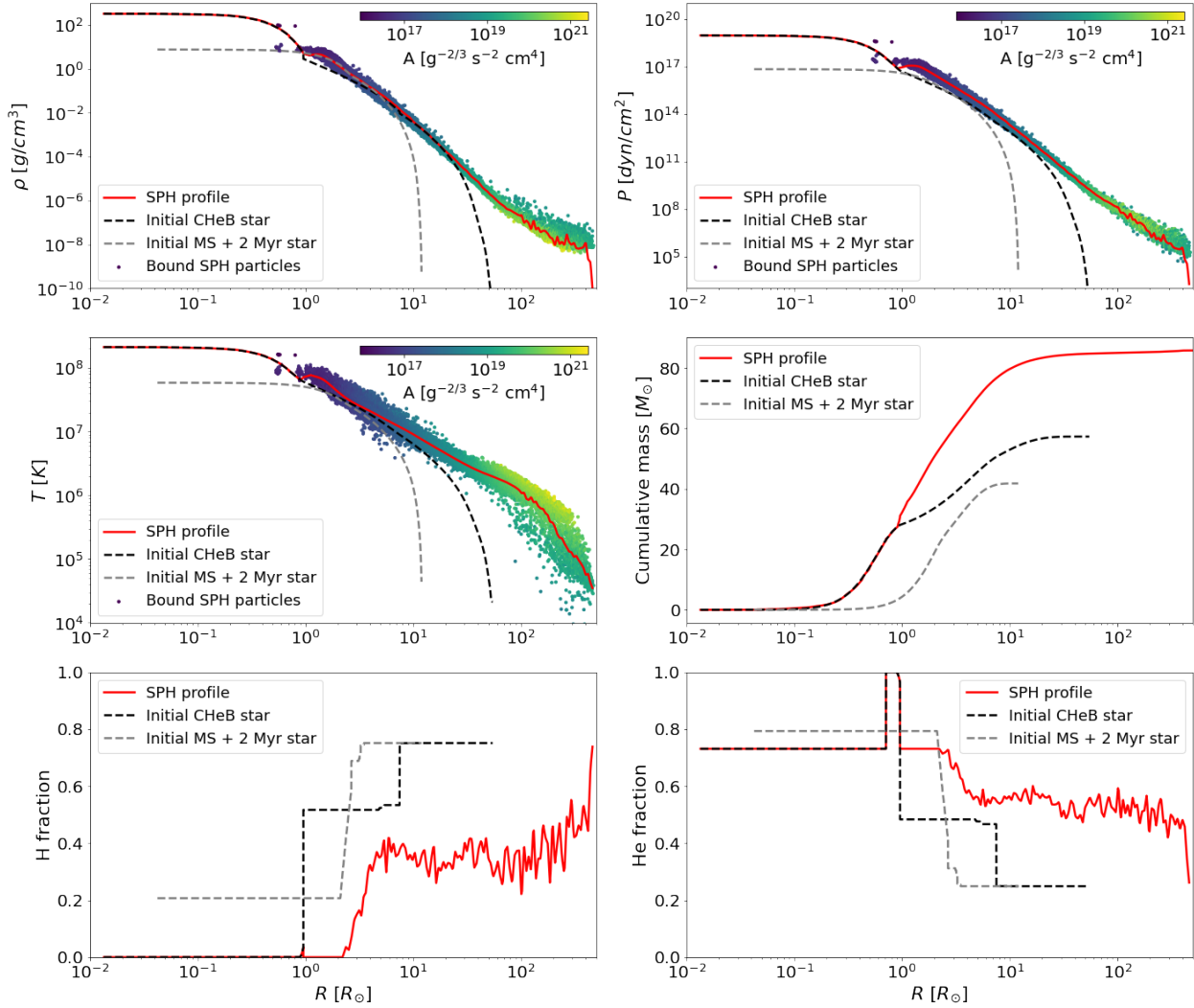
*Radial profiles of the main stellar properties for the remnant star of the Half Resolution collision simulation.*



*Note.* At the top panel, from left to right: density profile ( $\rho$ ) in  $g/cm^3$ , and pressure ( $P$ ) profile in  $dyn/cm^2$ , both of them along the stellar radius in  $R_\odot$ . At the medium panel, from left to right: temperature profile ( $T$ ) in  $K$ , and cumulative mass profile in  $M_\odot$ , both of them along the stellar radius in  $R_\odot$ . At the bottom panel, from left to right: hydrogen fraction and helium fraction, along the stellar radius in  $R_\odot$ . The red solid lines represent the SPH profile obtained after interpolating the average values obtained in the radial binning of all the particles in the final snapshot of the simulation. The dashed black lines represent the input stellar profile for the primary star at CHeB produced by PARSEC and described in section 2.1.1. The dashed gray lines represent the input stellar profile for the secondary star at MS produced by PARSEC and described in section 2.1.1. For the density, pressure, and temperature profiles, the colored dots are the bound SPH particles, ordered by increasing distance to the center of the simulation. They are colored by their entropic variable ( $A$ ), in  $g^{-2/3} s^{-2} cm^4$ , calculated using equation 2.40.

**Figure 3.12**

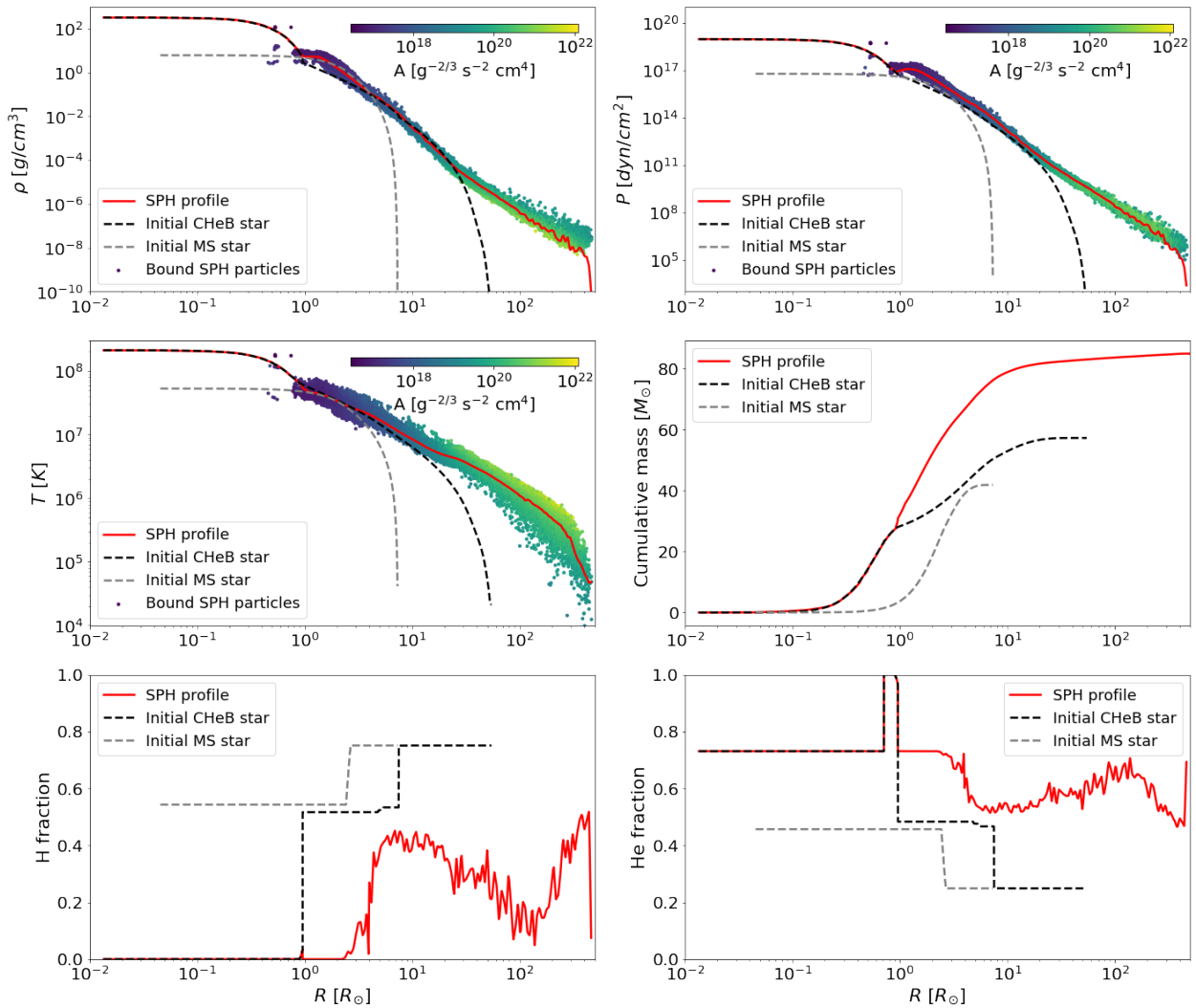
Radial profiles of the main stellar properties for the remnant star of the + 2 Myr collision simulation.



*Note.* At the top panel, from left to right: density profile ( $\rho$ ) in  $g/cm^3$ , and pressure ( $P$ ) profile in  $dyn/cm^2$ , both of them along the stellar radius in  $R_\odot$ . At the medium panel, from left to right: temperature profile ( $T$ ) in  $K$ , and cumulative mass profile in  $M_\odot$ , both of them along the stellar radius in  $R_\odot$ . At the bottom panel, from left to right: hydrogen fraction and helium fraction, along the stellar radius in  $R_\odot$ . The red solid lines represent the SPH profile obtained after interpolating the average values obtained in the radial binning of all the particles in the final snapshot of the simulation. The dashed black lines represent the input stellar profile for the primary star at CHeB produced by PARSEC and described in section 2.1.1. The dashed gray lines represent the input stellar profile for the secondary star at MS + 2 Myr produced by PARSEC and described in section 2.1.1. For the density, pressure, and temperature profiles, the colored dots are the bound SPH particles, ordered by increasing distance to the center of the simulation. They are colored by their entropic variable ( $A$ ), in  $g^{-2/3} s^{-2} cm^4$ , calculated using equation 2.40.

**Figure 3.13**

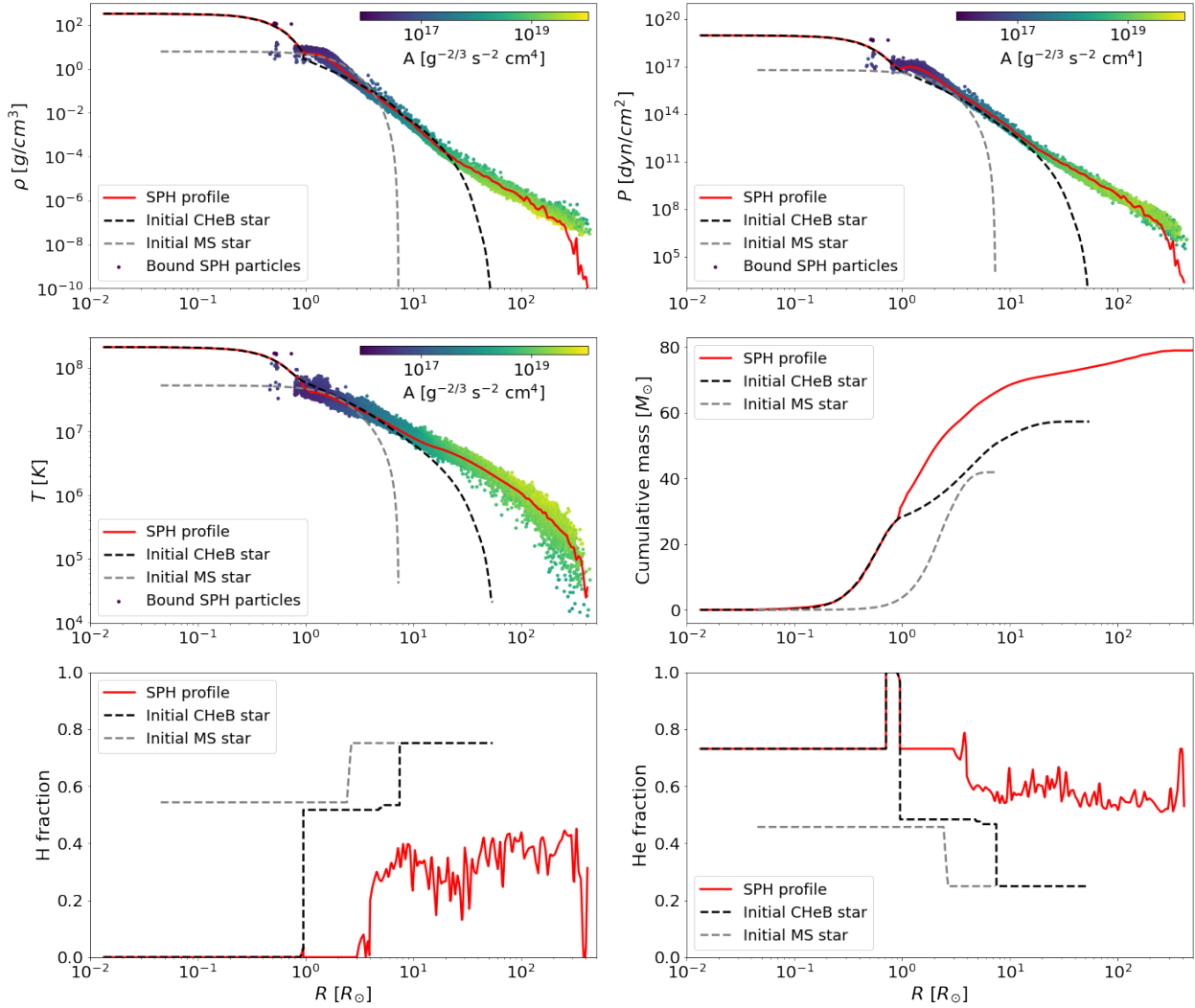
*Radial profiles of the main stellar properties for the remnant star of the  $b = 0.1 R_\odot$  collision simulation.*



*Note.* At the top panel, from left to right: density profile ( $\rho$ ) in  $g/cm^3$ , and pressure ( $P$ ) profile in  $dyn/cm^2$ , both of them along the stellar radius in  $R_\odot$ . At the medium panel, from left to right: temperature profile ( $T$ ) in  $K$ , and cumulative mass profile in  $M_\odot$ , both of them along the stellar radius in  $R_\odot$ . At the bottom panel, from left to right: hydrogen fraction and helium fraction, along the stellar radius in  $R_\odot$ . The red solid lines represent the SPH profile obtained after interpolating the average values obtained in the radial binning of all the particles in the final snapshot of the simulation. The dashed black lines represent the input stellar profile for the primary star at CHeB produced by PARSEC and described in section 2.1.1. The dashed gray lines represent the input stellar profile for the secondary star at MS produced by PARSEC and described in section 2.1.1. For the density, pressure, and temperature profiles, the colored dots are the bound SPH particles, ordered by increasing distance to the center of the simulation. They are colored by their entropic variable ( $A$ ), in  $g^{-2/3} s^{-2} cm^4$ , calculated using equation 2.40.

**Figure 3.14**

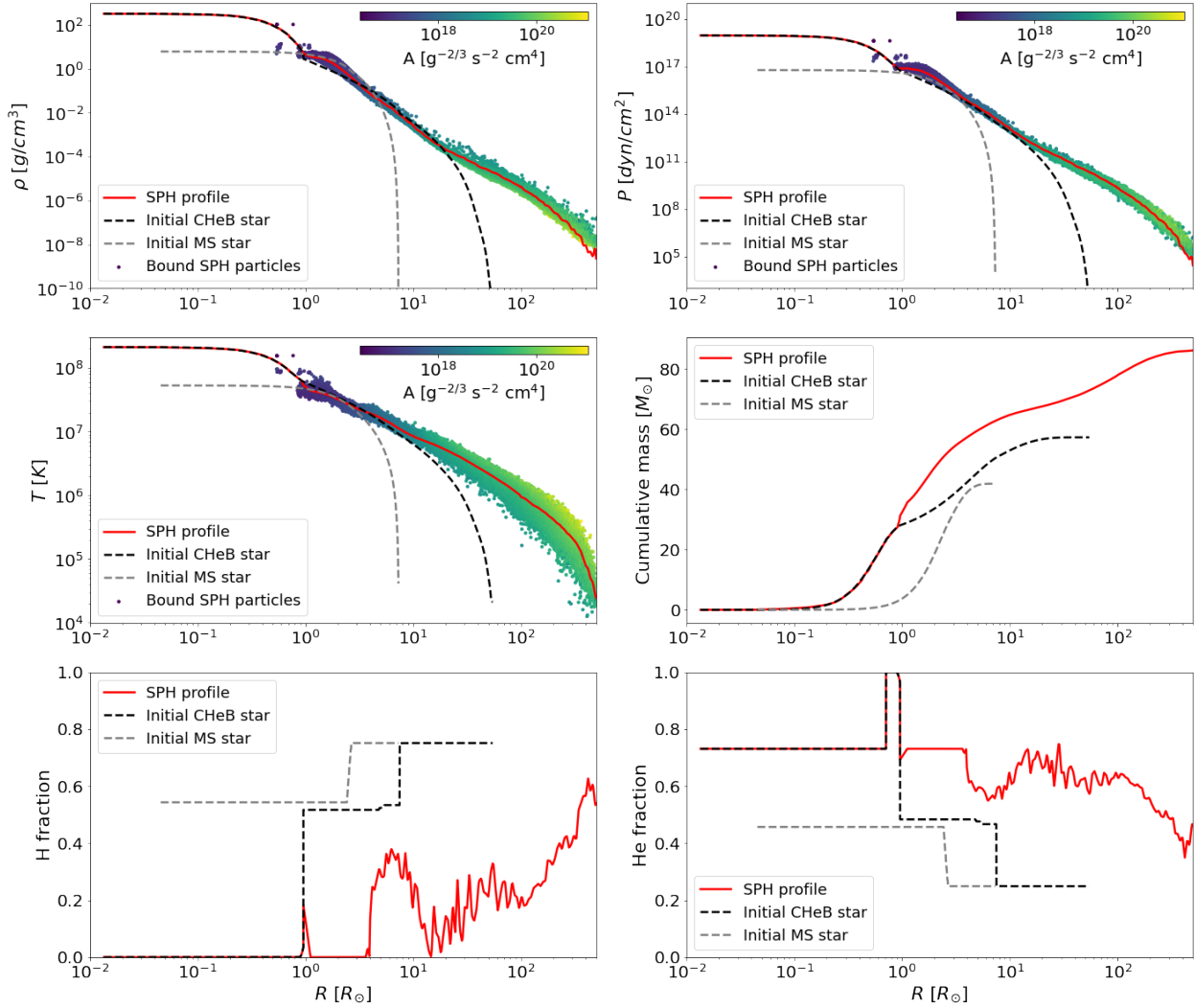
Radial profiles of the main stellar properties for the remnant star of the  $b = 1 R_\odot$  collision simulation.



*Note.* At the top panel, from left to right: density profile ( $\rho$ ) in  $g/cm^3$ , and pressure ( $P$ ) profile in  $dyn/cm^2$ , both of them along the stellar radius in  $R_\odot$ . At the medium panel, from left to right: temperature profile ( $T$ ) in  $K$ , and cumulative mass profile in  $M_\odot$ , both of them along the stellar radius in  $R_\odot$ . At the bottom panel, from left to right: hydrogen fraction and helium fraction, along the stellar radius in  $R_\odot$ . The red solid lines represent the SPH profile obtained after interpolating the average values obtained in the radial binning of all the particles in the final snapshot of the simulation. The dashed black lines represent the input stellar profile for the primary star at CHeB produced by PARSEC and described in section 2.1.1. The dashed gray lines represent the input stellar profile for the secondary star at MS produced by PARSEC and described in section 2.1.1. For the density, pressure, and temperature profiles, the colored dots are the bound SPH particles, ordered by increasing distance to the center of the simulation. They are colored by their entropic variable ( $A$ ), in  $g^{-2/3} s^{-2} cm^4$ , calculated using equation 2.40.

**Figure 3.15**

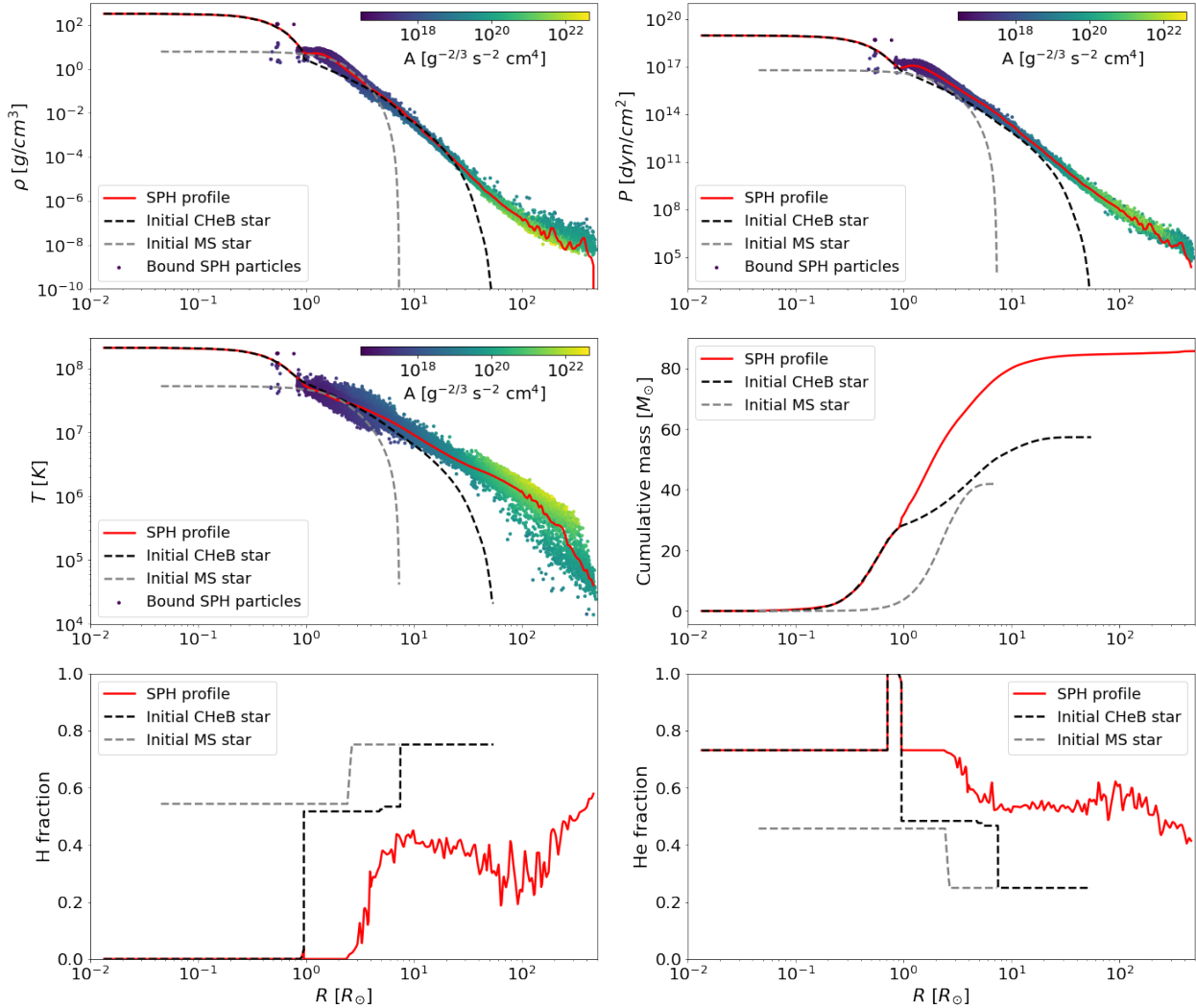
Radial profiles of the main stellar properties for the remnant star of the  $b = 3 R_\odot$  collision simulation.



*Note.* At the top panel, from left to right: density profile ( $\rho$ ) in  $g/cm^3$ , and pressure ( $P$ ) profile in  $dyn/cm^2$ , both of them along the stellar radius in  $R_\odot$ . At the medium panel, from left to right: temperature profile ( $T$ ) in  $K$ , and cumulative mass profile in  $M_\odot$ , both of them along the stellar radius in  $R_\odot$ . At the bottom panel, from left to right: hydrogen fraction and helium fraction, along the stellar radius in  $R_\odot$ . The red solid lines represent the SPH profile obtained after interpolating the average values obtained in the radial binning of all the particles in the final snapshot of the simulation. The dashed black lines represent the input stellar profile for the primary star at CHeB produced by PARSEC and described in section 2.1.1. The dashed gray lines represent the input stellar profile for the secondary star at MS produced by PARSEC and described in section 2.1.1. For the density, pressure, and temperature profiles, the colored dots are the bound SPH particles, ordered by increasing distance to the center of the simulation. They are colored by their entropic variable ( $A$ ), in  $g^{-2/3} s^{-2} cm^4$ , calculated using equation 2.40.

**Figure 3.16**

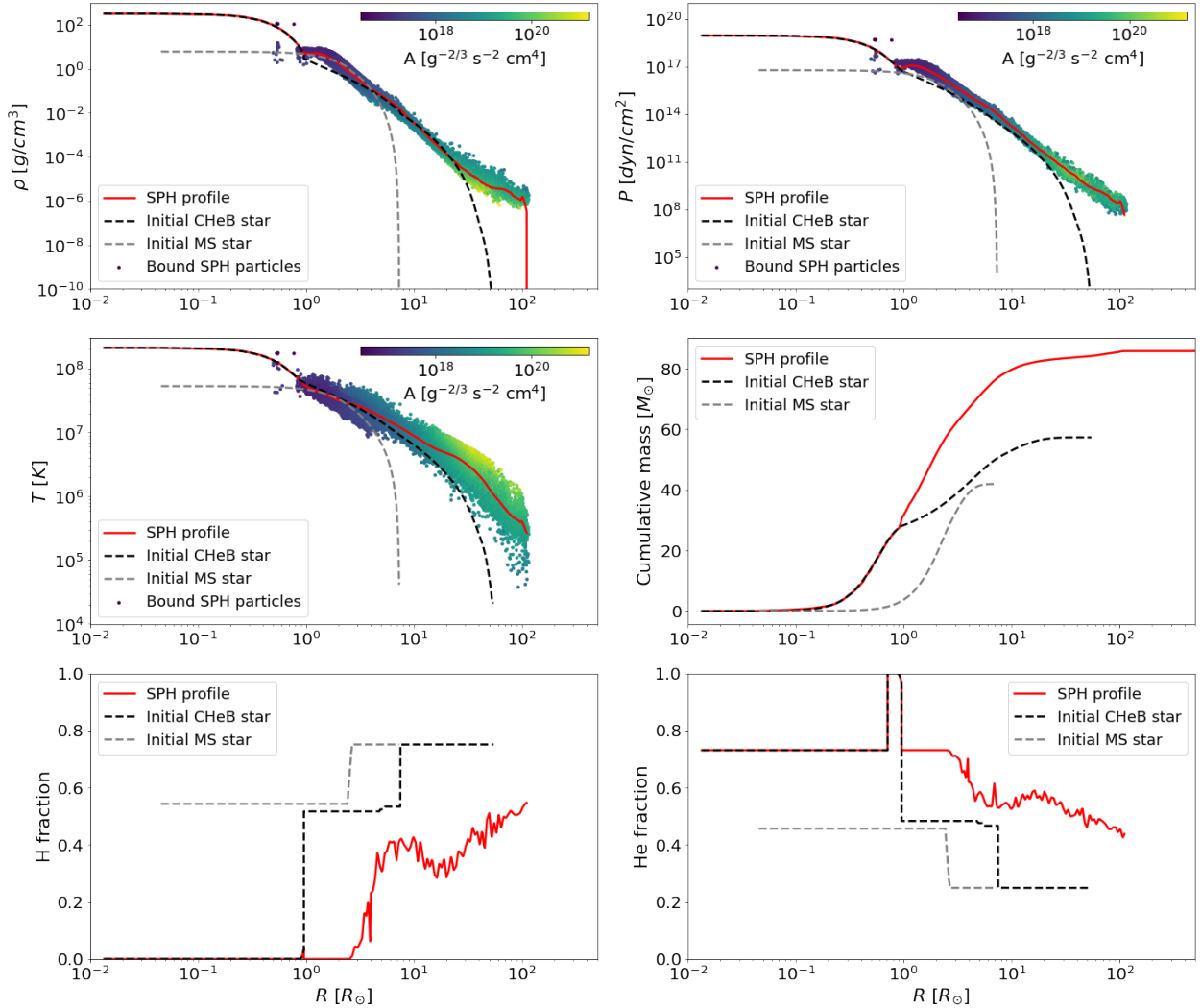
Radial profiles of the main stellar properties for the remnant star of the  $v_\infty = 10 \text{ km/s}$  collision simulation.



*Note.* At the top panel, from left to right: density profile ( $\rho$ ) in  $\text{g}/\text{cm}^3$ , and pressure ( $P$ ) profile in  $\text{dyn}/\text{cm}^2$ , both of them along the stellar radius in  $R_\odot$ . At the medium panel, from left to right: temperature profile ( $T$ ) in  $K$ , and cumulative mass profile in  $M_\odot$ , both of them along the stellar radius in  $R_\odot$ . At the bottom panel, from left to right: hydrogen fraction and helium fraction, along the stellar radius in  $R_\odot$ . The red solid lines represent the SPH profile obtained after interpolating the average values obtained in the radial binning of all the particles in the final snapshot of the simulation. The dashed black lines represent the input stellar profile for the primary star at CHeB produced by PARSEC and described in section 2.1.1. The dashed gray lines represent the input stellar profile for the secondary star at MS produced by PARSEC and described in section 2.1.1. For the density, pressure, and temperature profiles, the colored dots are the bound SPH particles, ordered by increasing distance to the center of the simulation. They are colored by their entropic variable ( $A$ ), in  $\text{g}^{-2/3} \text{s}^{-2} \text{cm}^4$ , calculated using equation 2.40.

**Figure 3.17**

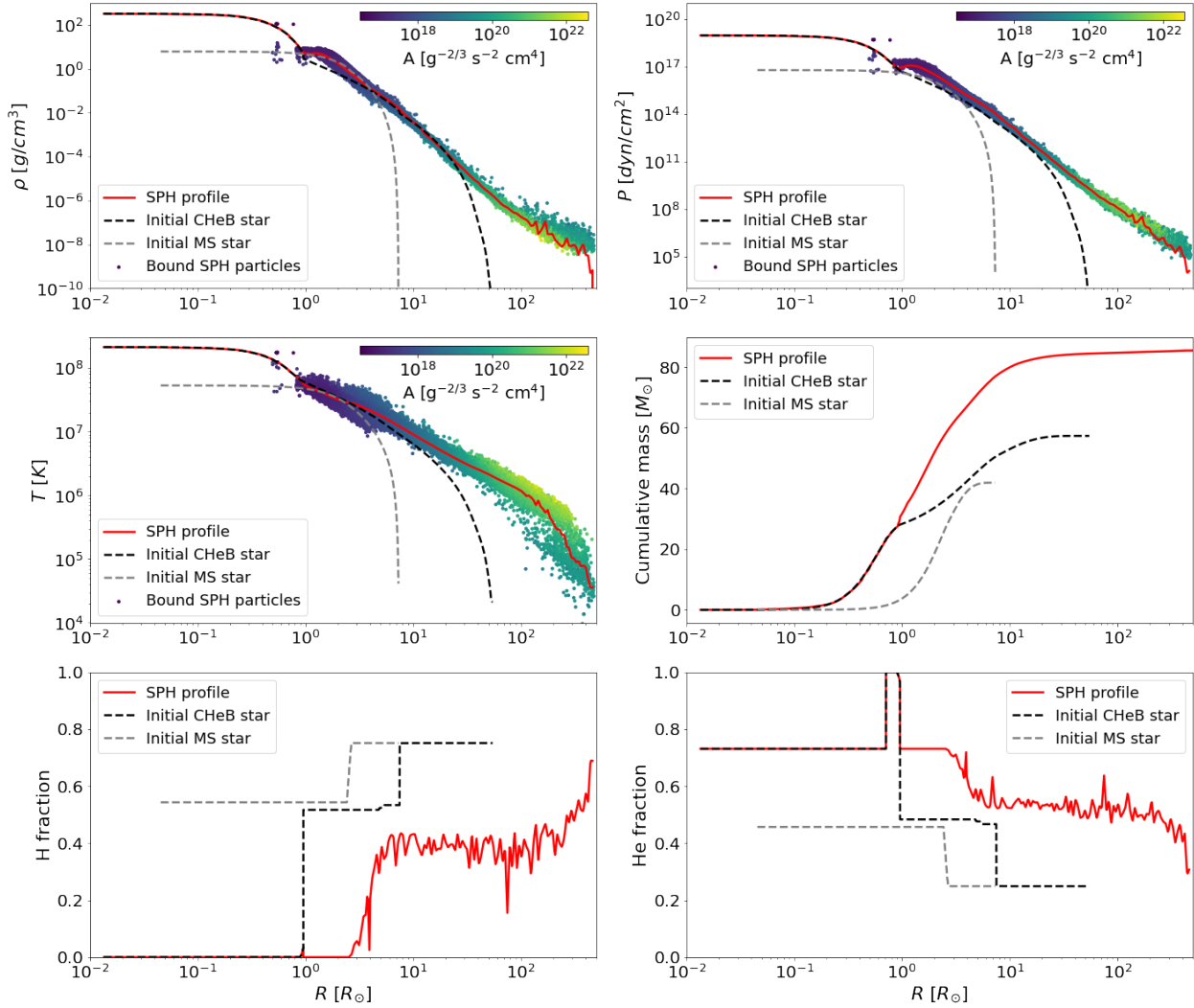
Radial profiles of the main stellar properties for the remnant star of the  $v_\infty = 100 \text{ km/s}$  collision simulation.



*Note.* At the top panel, from left to right: density profile ( $\rho$ ) in  $\text{g/cm}^3$ , and pressure ( $P$ ) profile in  $\text{dyn/cm}^2$ , both of them along the stellar radius in  $R_\odot$ . At the medium panel, from left to right: temperature profile ( $T$ ) in  $K$ , and cumulative mass profile in  $M_\odot$ , both of them along the stellar radius in  $R_\odot$ . At the bottom panel, from left to right: hydrogen fraction and helium fraction, along the stellar radius in  $R_\odot$ . The red solid lines represent the SPH profile obtained after interpolating the average values obtained in the radial binning of all the particles in the final snapshot of the simulation. The dashed black lines represent the input stellar profile for the primary star at CHeB produced by PARSEC and described in section 2.1.1. The dashed gray lines represent the input stellar profile for the secondary star at MS produced by PARSEC and described in section 2.1.1. For the density, pressure, and temperature profiles, the colored dots are the bound SPH particles, ordered by increasing distance to the center of the simulation. They are colored by their entropic variable ( $A$ ), in  $\text{g}^{-2/3} \text{s}^{-2} \text{cm}^4$ , calculated using equation 2.40.

**Figure 3.18**

Radial profiles of the main stellar properties for the remnant star of the  $v_\infty = 500 \text{ km/s}$  collision simulation.



*Note.* At the top panel, from left to right: density profile ( $\rho$ ) in  $\text{g}/\text{cm}^3$ , and pressure ( $P$ ) profile in  $\text{dyn}/\text{cm}^2$ , both of them along the stellar radius in  $R_\odot$ . At the medium panel, from left to right: temperature profile ( $T$ ) in  $K$ , and cumulative mass profile in  $M_\odot$ , both of them along the stellar radius in  $R_\odot$ . At the bottom panel, from left to right: hydrogen fraction and helium fraction, along the stellar radius in  $R_\odot$ . The red solid lines represent the SPH profile obtained after interpolating the average values obtained in the radial binning of all the particles in the final snapshot of the simulation. The dashed black lines represent the input stellar profile for the primary star at CHeB produced by PARSEC and described in section 2.1.1. The dashed gray lines represent the input stellar profile for the secondary star at MS produced by PARSEC and described in section 2.1.1. For the density, pressure, and temperature profiles, the colored dots are the bound SPH particles, ordered by increasing distance to the center of the simulation. They are colored by their entropic variable ( $A$ ), in  $\text{g}^{-2/3} \text{s}^{-2} \text{cm}^4$ , calculated using equation 2.40.

Regarding the cumulative mass profiles, and the hydrogen and helium fractions, the comparisons of the final SPH profile with the initial stellar profiles allow us to conclude that structurally all remnants are formed preserving the core of the primary star (TAMS or CHeB), while the envelope

arises from combining all the mass of the secondary star with the remaining mass of the primary. In figures 3.10 to 3.18 we can see how the solid red line (SPH profile) follows the same behavior as the dotted black line (primary star profile) in the first radial values, while later they radically diverge. This happens in both chemical composition and size. This result has been reported by other authors in studies very similar to this thesis (Ballone et al., 2023; Costa et al., 2022), and allows corroborating the widely used hypothesis for the construction of remnants using only stellar evolution codes. In such methodologies, the post-collisional star is built by preserving the primary star core, while the mass of the secondary star is added to its envelope (Di Carlo, Mapelli, Giacobbo, et al., 2020; Glebbeek et al., 2013; Renzo et al., 2020). It is important to emphasize that this can be concluded since the parent stars analyzed here, and in all the previously mentioned works, present a clear differentiation in their evolutionary state at the moment of impact. In cases where the evolutionary stages are not so distinguishable this behavior can change since the conditions of both nuclei will be very similar, favoring their mixing.

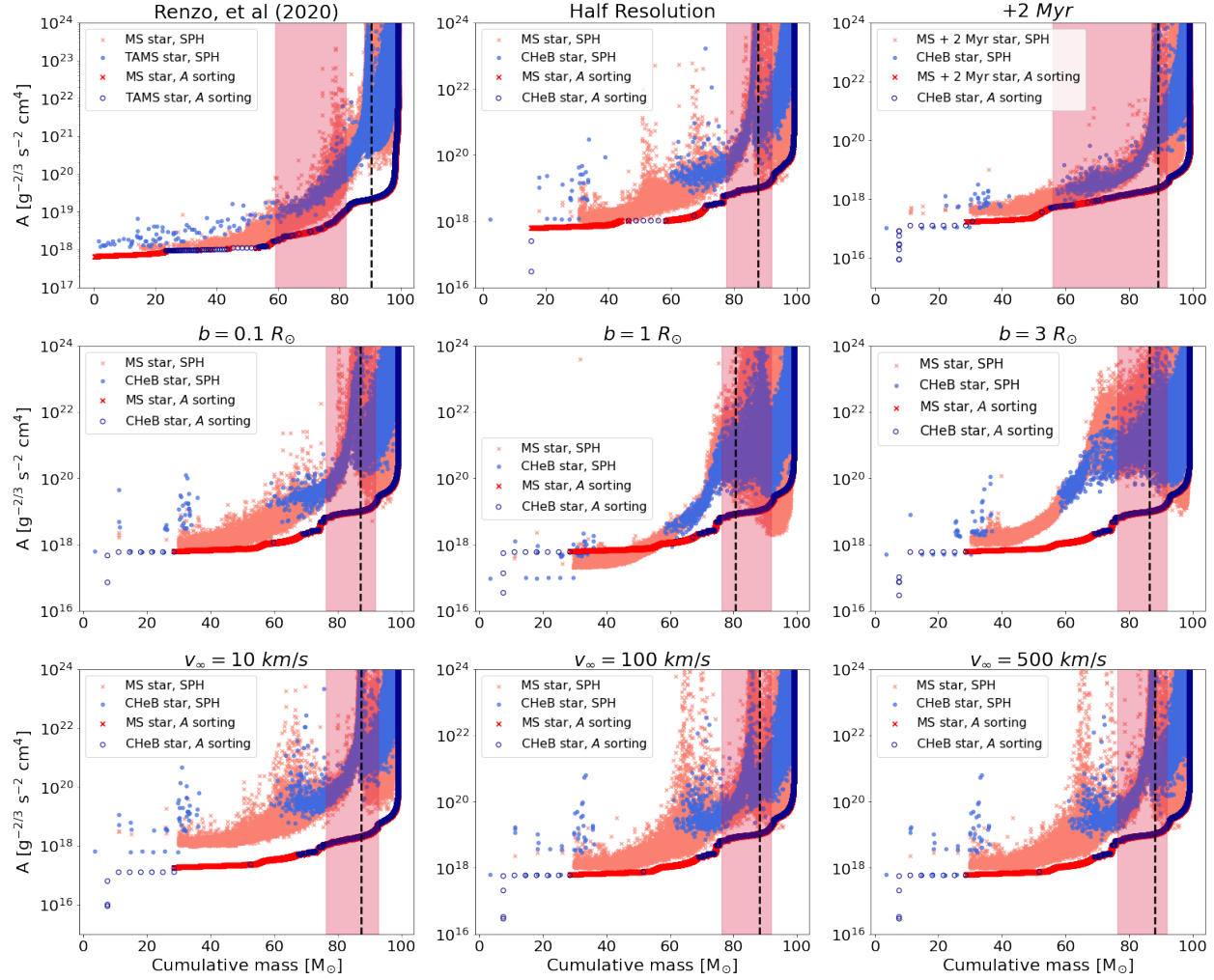
After the analysis of the stellar structure, we also decided to test the buoyancy principle explained in section 2.3. Under that theoretical framework, the bound particles forming each stellar remnant should be rearranged so that their entropic variable  $A$  increases from the core to the outer layers (Gaburov et al., 2008). This is the reason why in the  $\rho$ ,  $P$  and  $T$  profiles, in each of figures 3.10 through 3.18, the SPH particles belonging to the post-collisional star were colored with respect to the  $A$  value in  $g^{-2/3}s^{-2}cm^4$  units. As evidenced in each of the above plots, all the hydrodynamical simulations performed with STARSMASHER and analyzed in this thesis, follow this principle. The particles with lower  $A$  (violet colors) are located in the initial region of the radial profiles, while the particles with higher  $A$  (yellow colors) are located in the outer regions of the star. This is a very important result, since it allows us to extend the range of applicability of the entropy ordering algorithm explained in section 2.3. Now  $A$  also allows to distinction of different layers of post-collisional stars built from massive parent stars outside a gentle collisional environment.

Finally, and thanks to the previous result, we decided to apply the entropy sorting algorithm for all collision configurations. The basic idea was to construct the post-collision star from the SPH files, using the relaxation routines of STARSMASHER, to compare it directly with the last snapshot of each collision routine. In this way, the differences between a full collisional hydrodynamical simulation and a semi-analytic approximation could be evidenced. Figure 3.19 shows the entropic variable profiles, along the cumulative mass coordinate, of each collision configuration. In each box, we compare their respective STARSMASHER simulation (light reds X's and filled light blue circles), with the results of the entropy sorting algorithm for the same parent stars (reds X's and empty dark blue circles). Analyzing each simulation we can see that although the precise values of  $A$  differ in the two methodologies (differences in the y-axis), the arrangement of each of the SPH particles inside the star is almost equivalent in all cases (the markers and colors of each particle are located at very close values in the x-axis). This is again a very interesting and powerful result because it allows us to construct the post-collisional stars without the need to run the hydrodynamical collision routine, greatly reducing the time spent in the construction of these profiles and thus allowing a broader, more detailed, and faster exploration of the parameter space of massive stellar collisions. The differences in the y-axis are because the thermodynamic conditions inside the primary and secondary stars radically differ from those of the remnant star, but the important

thing here is not to determine  $A$  precisely but to be able to identify its differences.

**Figure 3.19**

*Entropic variable profile, along the cumulative mass coordinate, of each STARSMASHER collision simulation remnant star.*



*Note.* In each square the entropic variable ( $A$ ) (defined in sec 2.3) is plotted on the  $y$  axis, in  $g^{-2/3} s^{-2} cm^4 g/cm^3$  units. The  $x$  axis is the cumulative mass, from the center of the remnant star outward, in  $M_\odot$  (this quantity is equivalent to the stellar radius). At the top panel, from left to right, the visualized collision simulations are Renzo, et al (2020), Half Resolution, and + 2 Myr. At the medium panel, from left to right:  $b = 0.1 R_\odot$ ,  $b = 1 R_\odot$  and  $b = 3 R_\odot$ . The bottom panel, from left to right:  $v_\infty = 10 km/s$ ,  $v_\infty = 100 km/s$  and  $v_\infty = 500 km/s$ . The circle points represent the particles that originally modeled the primary star of the collision (TAMS or CHeB, depending on the case), while the X's represent the particles that modeled the secondary star (MS or MS + 2 Myr, depending the case). The dark blue nonfilled circles and the big reds X's correspond to the  $A$  values computed from the initial conditions of the simulations, and they arrange to form the remnant star following the entropic sorting algorithm described in section 2.3. The light blue filled circles and the small salmon X's, correspond to the  $A$  values computed from the final snapshot of the SPH simulations. The dotted black line is the total bound mass of the remnant star formed after the collision, and the light crimson square demarcates the limits where the entropy profile, built from the sorting algorithm, has its second plateau.

Apart from the possibility of constructing the structure of the collisional star, in this work, we identify that the entropy sorting algorithm can predict an expected range of mass loss in the collision, a key feature that can only be accurately determined today using SPH simulations. Looking again at figure 3.19 we can notice that the mass loss (vertical dashed black line), determined with the criterion discussed in section 3.1, is almost always located inside the blurred crimson rectangle, except for the Renzo, et al (2020) case. The lower and upper vertical limits of the rectangle coincide with the starting and ending points of the second plateau of the  $A$  profile determined by the algorithm. These two points can be precisely located using a mathematical criterion, since their positions in  $x$  (Cumulative mass in  $M_{\odot}$ ) coincide with the places where the second derivative of the profile is equal to 0 (they are a point of inflection), and their values can be seen in table 3.2.

**Table 3.2**

*Final percentage of unbound mass, and predicted remnant mass, for each of the simulated STARSMASHER collisions.*

Simulation	$M_{A,\text{low-limit}}$ [ $M_{\odot}$ ]	$M_{A,\text{up-limit}}$ [ $M_{\odot}$ ]	$M_{\text{remnant}}$ [ $M_{\odot}$ ]
Renzo, et al (2020)	58.96	82.06	89.82
Half Resolution	77.39	91.89	87.48
+ 2 Myr	55.78	91.75	88.54
$b = 0.1 R_{\odot}$	76.26	91.82	86.78
$b = 1 R_{\odot}$	76.26	91.82	80.30
$b = 3 R_{\odot}$	76.26	91.82	86.36
$v_{\infty} = 10 \text{ km/s}$	76.26	92.73	87.34
$v_{\infty} = 100 \text{ km/s}$	76.26	91.82	87.69
$v_{\infty} = 500 \text{ km/s}$	76.26	91.82	87.63

*Note.* Columns from left to right: simulation name, final unbound mass percentage, and stellar remnant mass in  $M_{\odot}$ .

In constructing the entropic profile it can then be proposed that these inflection points be considered as the values between which the mass lost after the collision ( $M_{\text{unb}}$ ) can fluctuate. This would allow the post-collision star to be constructed mimicking the structure and mass of a full hydrodynamical collision simulation. It is essential to point out that these results are not satisfactory when the chemical composition of both parent stars is almost equivalent because they are close in their evolutionary stages, meaning that each set of particles will have similar values for  $A$ , as stated in equation 2.40 (Gaburov et al., 2008). That is why this algorithm does not apply in the Renzo, et al (2020) scenario.

### 3.4 Recommendations and perspectives

In general terms, the results obtained in this work are in favor of the hypothesis of the black hole population in the PI mass gap through stellar collisions of massive stars. Each of the collisional simulations has generated a stellar remnant with the mass indicated for such a target. However, to continue building evidence in this sense, it is necessary to propose future work in which all the stellar remnants analyzed here can evolve to their final state using stellar evolution codes. This coupling will allow us to compute with certainty the percentage of collisions that function as a

formation channel, together with their dependence on the collisional parameters varied here.

In addition to the above, this scenario still needs further exploration of the parameter space, and this thesis allows us to glimpse that the entropy ordering algorithm should be a tool used for this purpose. However, this methodology should always be accompanied and compared with hydrodynamical simulations when these can be generated.

Finally, it has been shown throughout this work that STARSMASHER is a very high-level stellar collision simulation code, which manages to apply the SPH scheme in adverse thermodynamic conditions, obtaining physical results in a not very long time and with an almost constant convergence rate. However, to revalidate the comparison with the entropy ordering method, it is proposed that more tests be carried out on its shock propagation treatment, seeking to determine more clearly if the evolution of the thermodynamic properties along the non-gentle shocks is adequate.

#### 4. Conclusions

The detection of black holes in the PI mass gap brought with it the challenge of exploring new formation channels for the generation of such compact objects. This thesis explored the possibility of forming PI black holes through the collision of massive stars in young SC. To achieve this goal, a set of 9 hydrodynamical simulations of massive stellar collisions, generated with the SPH STARSMASHER code, were constructed and analyzed. Such a large set of different settings had never been analyzed before. This methodology allowed us to describe in detail the dynamical and structural characteristics of the remnant star, and its dependence on the main collisional parameters, verifying that all configurations of direct dynamical encounters meet the mass requirements to form the desired black hole.

In addition to the above, the entropy sorting algorithm for the construction of stellar remnants, proposed by [J. C. Lombardi Jr et al. \(2002\)](#) and [Glebbeek and Pols \(2008\)](#), was applied in all collisions. Their results were directly compared with the full hydrodynamic simulations verifying their similarities and limitations, thus extending their range of applicability. The post-collisional stellar profiles generated from the algorithm allowed the determination of the percentage of mass lost after the collision, a result enormously useful for the future exploration of the parameter space of stellar collisions and for the first time proposed in this work. After the joint analysis of both methodologies, the formation channel through stellar impacts is established as a plausible channel to explain black holes in the IP, in agreement with previous studies on the same problem ([Ballone et al., 2023](#); [Costa et al., 2022](#); [Di Carlo, Mapelli, Giacobbo, et al., 2020](#); [Renzo et al., 2020](#)). This allows us to alleviate this tension without the need to introduce substantial changes in the current theory of stellar evolution.

This thesis confirms that the determination of the center of the remnant is a central point in the analysis of hydrodynamical simulations of star collisions since it is the starting point from which all other calculations are derived and permeates all the conclusions that can be drawn from the analysis. It is always recommended to be very sensitive with the criterion that is finally adopted for such a definition and it is a point that must be specified in any of these types of studies. The approximation for specific potential energy made in this study impacts the expected results for bound-unbound particles at the lower radial boundaries, however, the final impact on the unbound mass percentage is almost negligible after correction for the central particles. The possibility of using the precise formula for the calculation of the specific potential energy should be rejected, as it demands excessive computational resources for this type of analysis.

Undoubtedly the most important collisional parameter, among the ones explored here, in determining the final characteristics of the remnant star is the impact parameter. Increasing its value gradually increases the percentage of mass lost in the collision (as it can be seen in Table 3.1) and for sufficiently high values could produce a remnant that does not fall within the possible candidates for the generation of a black hole in the pair-instability mass gap. In addition to the above, we were able to show that having a non-radial collision automatically produces a tangential velocity component in the particles that make up the post-coalescence star, triggering a change in the chemical composition of the star's envelope and therefore impacting its subsequent evolution, generating the possibility of them skip the formation of a PI black hole, even if the mass conditions are met. It is important to emphasize that radial collisions should be almost impossible in the Universe, dynamical heating of stellar clusters prevents almost any collision where  $b = 0$ . For this reason, the fact that this parameter is the most important value in determining the mass loss is of major importance and indicates that the assumption made in previous studies, where the upper limit to that mass loss is set by the radial configuration, should be revised.

The SPH particle entropy sorting methodology, for the generation of stellar collisional remnants, was shown to closely reproduce the results of full hydrodynamic simulations. The buoyancy principle applied in all the configurations described here makes it possible to recreate the post-collisional stellar structures and propose a selection criterion for the mass loss within a range. However, for configurations involving primary and secondary stars at a close evolutionary stage, this algorithm does not allow a correct reproduction of the full hydrodynamical simulation results.

Finally, addressing the objective of this thesis, all the simulations analyzed here produce a post-coalescence star with the mass necessary to generate a black hole within the PI mass gap. This fact strongly favors stellar collisions of massive stars as a viable population channel for such black holes, since the orbital parameters of the encounters described here are in agreement with the expected properties of stellar collisions in young star clusters. This mechanism may alleviate existing tensions following observations of black holes in the PI mass gap.

## References

- Abbott, R., Abbott, T., Abraham, S., Acernese, F., Ackley, K., Adams, C., ... others (2020a). Gw190521: a binary black hole merger with a total mass of 150 m. *Physical review letters*, 125(10), 101102.
- Abbott, R., Abbott, T., Abraham, S., Acernese, F., Ackley, K., Adams, C., ... others (2020b). Properties and astrophysical implications of the 150 m binary black hole merger gw190521. *The Astrophysical Journal Letters*, 900(1), L13.
- Abbott, R., Abbott, T., Acernese, F., Ackley, K., Adams, C., Adhikari, N., ... others (2021a). Gwtc-2.1: Deep extended catalog of compact binary coalescences observed by ligo and virgo during the first half of the third observing run. *arXiv preprint arXiv:2108.01045*.
- Abbott, R., Abbott, T., Acernese, F., Ackley, K., Adams, C., Adhikari, N., ... others (2021b). Gwtc-3: compact binary coalescences observed by ligo and virgo during the second part of the third observing run. *arXiv preprint arXiv:2111.03606*.
- Aghakhanloo, M., Murphy, J. W., Smith, N., & Hložek, R. (2017). Modelling luminous-blue-variable isolation. *Monthly Notices of the Royal Astronomical Society*, 472(1), 591–603.
- Alastuey, A., & Jancovici, B. (1978). Nuclear reaction rate enhancement in dense stellar matter. *Astrophysical Journal, Part 1, vol. 226, Dec. 15, 1978, p. 1034-1040.*, 226, 1034–1040.
- Amthor, A. M., Galaviz, D., Heger, A., Sakharuk, A., Schatz, H., & Smith, K. (2006). Sensitivity of type i x-ray bursts to rp-process reaction rates. *arXiv preprint astro-ph/0608451*.
- Angulo, C., Arnould, M., Rayet, M., Descouvemont, P., Baye, D., Leclercq-Willain, C., ... others (1999). A compilation of charged-particle induced thermonuclear reaction rates. *Nuclear Physics A*, 656(1), 3–183.
- Antonini, F., Gieles, M., & Gualandris, A. (2019). Black hole growth through hierarchical black hole mergers in dense star clusters: implications for gravitational wave detections. *Monthly Notices of the Royal Astronomical Society*, 486(4), 5008–5021.
- Arca-Sedda, M., Rizzuto, F. P., Naab, T., Ostriker, J., Giersz, M., & Spurzem, R. (2021). Breaching the limit: formation of gw190521-like and imbh mergers in young massive clusters. *The Astrophysical Journal*, 920(2), 128.
- Ballone, A., Costa, G., Mapelli, M., MacLeod, M., Torniamenti, S., & Pacheco-Arias, J. M. (2023).

- Formation of black holes in the pair-instability mass gap: Hydrodynamical simulations of a head-on massive star collision. *Monthly Notices of the Royal Astronomical Society*, 519(4), 5191–5201.
- Balsara, D. S. (1995). Von neumann stability analysis of smoothed particle hydrodynamics—suggestions for optimal algorithms. *Journal of Computational Physics*, 121(2), 357–372.
- Banerjee, S. (2022). Binary black hole mergers from young massive clusters in the pair-instability supernova mass gap. *Astronomy & Astrophysics*, 665, A20.
- Barkat, Z., Rakavy, G., & Sack, N. (1967). Dynamics of supernova explosion resulting from pair formation. *Physical Review Letters*, 18(10), 379.
- Bartos, I., Kocsis, B., Haiman, Z., & Márka, S. (2017). Rapid and bright stellar-mass binary black hole mergers in active galactic nuclei. *The Astrophysical Journal*, 835(2), 165.
- Belczynski, K., Heger, A., Gladysz, W., Ruiter, A. J., Woosley, S., Wiktorowicz, G., ... others (2016). The effect of pair-instability mass loss on black-hole mergers. *Astronomy & Astrophysics*, 594, A97.
- Belczynski, K., Hirschi, R., Kaiser, E., Liu, J., Casares, J., Lu, Y., ... Soria, R. (2020). The formation of a 70 m black hole at high metallicity. *The Astrophysical Journal*, 890(2), 113.
- Benz, W. (1990). Smooth particle hydrodynamics: a review. *The numerical modelling of nonlinear stellar pulsations: Problems and prospects*, 269–288.
- Bertelli, G., Bressan, A., Chiosi, C., Fagotto, F., & Nasi, E. (1994). A&as, 106. 275 (B94).
- Bertelli, G., Girardi, L., Marigo, P., & Nasi, E. (2008). Scaled solar tracks and isochrones in a large region of the z–y plane-i. from the zams to the tp-agb end for 0.15–2.5 stars. *Astronomy & Astrophysics*, 484(3), 815–830.
- Bertelli, G., Nasi, E., Girardi, L., & Marigo, P. (2009). Scaled solar tracks and isochrones in a large region of the z–y plane-ii. from 2.5 to 20 m stars. *Astronomy & Astrophysics*, 508(1), 355–369.
- Bond, J., Arnett, W., & Carr, B. J. (1984). The evolution and fate of very massive objects. *Astrophysical Journal, Part 1 (ISSN 0004-637X)*, vol. 280, May 15, 1984, p. 825-847. Research supported by the Science and Engineering Research Council., 280, 825–847.
- Bressan, A., Chiosi, C., & Bertelli, G. (1981). Mass loss and overshooting in massive stars. *Astronomy and Astrophysics*, 102, 25–30.
- Bressan, A., Fagotto, F., Bertelli, G., & Chiosi, C. (1993). Evolutionary sequences of stellar models with new radiative opacities. ii-z= 0.02. *Astronomy and Astrophysics Supplement Series (ISSN 0365-0138)*, vol. 100, no. 3, p. 647-664., 100, 647–664.
- Bressan, A., Marigo, P., Girardi, L., Salasnich, B., Dal Cero, C., Rubele, S., & Nanni, A. (2012).

- Parsec: stellar tracks and isochrones with the padova and trieste stellar evolution code. *Monthly Notices of the Royal Astronomical Society*, 427(1), 127–145.
- Brott, I., de Mink, S. E., Cantiello, M., Langer, N., de Koter, A., Evans, C. J., ... Vink, J. S. (2011). Rotating massive main-sequence stars-i. grids of evolutionary models and isochrones. *Astronomy & Astrophysics*, 530, A115.
- Caffau, E., Ludwig, H.-G., Steffen, M., Freytag, B., & Bonifacio, P. (2011). Solar chemical abundances determined with a co5bold 3d model atmosphere. *Solar Physics*, 268, 255–269.
- Caramana, E. J., Shashkov, M. J., & Whalen, P. P. (1998). Formulations of artificial viscosity for multi-dimensional shock wave computations. *Journal of Computational Physics*, 144(1), 70–97.
- Cassisi, S., Potekhin, A., Pietrinferni, A., Catelan, M., & Salaris, M. (2007). Updated electron-conduction opacities: the impact on low-mass stellar models. *The Astrophysical Journal*, 661(2), 1094.
- Caughlan, G. R., & Fowler, W. A. (1988). Thermonuclear reaction rates v. *Atomic Data and Nuclear Data Tables*, 40(2), 283–334.
- Chen, Y., Bressan, A., Girardi, L., Marigo, P., Kong, X., & Lanza, A. (2015). Parsec evolutionary tracks of massive stars up to 350 m at metallicities 0.0001 z 0.04. *Monthly Notices of the Royal Astronomical Society*, 452(1), 1068–1080.
- Choi, J., Dotter, A., Conroy, C., Cantiello, M., Paxton, B., & Johnson, B. D. (2016). Mesa isochrones and stellar tracks (mist). i. solar-scaled models. *The Astrophysical Journal*, 823(2), 102.
- Chugunov, A., Dewitt, H., & Yakovlev, D. (2007). Coulomb tunneling for fusion reactions in dense matter: Path integral monte carlo versus mean field. *Physical Review D*, 76(2), 025028.
- Clayton, D. D. (1983). *Principles of stellar evolution and nucleosynthesis*. University of Chicago press.
- Coleman Miller, M., & Hamilton, D. P. (2002). Production of intermediate-mass black holes in globular clusters. *Monthly Notices of the Royal Astronomical Society*, 330(1), 232–240.
- Costa, G., Ballone, A., Mapelli, M., & Bressan, A. (2022). Formation of black holes in the pair-instability mass gap: evolution of a post-collision star. *Monthly Notices of the Royal Astronomical Society*, 516(1), 1072–1080.
- Costa, G., Bressan, A., Mapelli, M., Marigo, P., Iorio, G., & Spera, M. (2021). Formation of gw190521 from stellar evolution: the impact of the hydrogen-rich envelope, dredge-up, and 12c ( $\alpha, \gamma$ ) 16o rate on the pair-instability black hole mass gap. *Monthly Notices of the Royal Astronomical Society*, 501(3), 4514–4533.
- Costa, G., Girardi, L., Bressan, A., Chen, Y., Goudfrooij, P., Marigo, P., ... Lanza, A. (2019). Multiple stellar populations in ngc 1866-new clues from cepheids and colour–magnitude

- diagram. *Astronomy & Astrophysics*, 631, A128.
- Costa, G., Girardi, L., Bressan, A., Marigo, P., Rodrigues, T. S., Chen, Y., ... Goudfrooij, P. (2019). Mixing by overshooting and rotation in intermediate-mass stars. *Monthly Notices of the Royal Astronomical Society*, 485(4), 4641–4657.
- Cox, J. P., & Giuli, R. T. (1968). *Principles of stellar structure: Physical principles* (Vol. 1). Gordon and Breach.
- Croon, D., McDermott, S. D., & Sakstein, J. (2020). New physics and the black hole mass gap. *Physical Review D*, 102(11), 115024.
- Cyburt, R. H., Amthor, A. M., Ferguson, R., Meisel, Z., Smith, K., Warren, S., ... others (2010). The jina reaclib database: its recent updates and impact on type-i x-ray bursts. *The Astrophysical Journal Supplement Series*, 189(1), 240.
- Dewitt, H., Graboske, H., & Cooper, M. (1973). Screening factors for nuclear reactions. i. general theory. *Astrophysical Journal, Vol. 181, pp. 439-456* (1973), 181, 439–456.
- Di Carlo, U. N., Giacobbo, N., Mapelli, M., Pasquato, M., Spera, M., Wang, L., & Haardt, F. (2019). Merging black holes in young star clusters. *Monthly Notices of the Royal Astronomical Society*, 487(2), 2947–2960.
- Di Carlo, U. N., Mapelli, M., Bouffanais, Y., Giacobbo, N., Santoliquido, F., Bressan, A., ... Haardt, F. (2020). Binary black holes in the pair instability mass gap. *Monthly Notices of the Royal Astronomical Society*, 497(1), 1043–1049.
- Di Carlo, U. N., Mapelli, M., Giacobbo, N., Spera, M., Bouffanais, Y., Rastello, S., ... others (2020). Binary black holes in young star clusters: the impact of metallicity. *Monthly Notices of the Royal Astronomical Society*, 498(1), 495–506.
- Faber, J. A., & Rasio, F. A. (2000). Post-newtonian sph calculations of binary neutron star coalescence: Method and first results. *Physical Review D*, 62(6), 064012.
- Farmer, R., Fields, C., Petermann, I., Dessart, L., Cantiello, M., Paxton, B., & Timmes, F. (2016). On variations of pre-supernova model properties. *The Astrophysical Journal Supplement Series*, 227(2), 22.
- Farmer, R., Renzo, M., de Mink, S., Fishbach, M., & Justham, S. (2020). Constraints from gravitational-wave detections of binary black hole mergers on the 12c ( $\alpha, \gamma$ ) 16o rate. *The Astrophysical Journal Letters*, 902(2), L36.
- Farmer, R., Renzo, M., de Mink, S., Marchant, P., & Justham, S. (2019). Mind the gap: the location of the lower edge of the pair-instability supernova black hole mass gap. *The Astrophysical Journal*, 887(1), 53.
- Farrell, E., Groh, J. H., Hirschi, R., Murphy, L., Kaiser, E., Ekström, S., ... Meynet, G. (2021). Is gw190521 the merger of black holes from the first stellar generations? *Monthly Notices of the Royal Astronomical Society: Letters*, 502(1), L40–L44.

- Ferguson, J. W., Alexander, D. R., Allard, F., Barman, T., Bodnarik, J. G., Hauschildt, P. H., ... Tamanai, A. (2005). Low-temperature opacities. *The Astrophysical Journal*, 623(1), 585.
- Fernández, R., Quataert, E., Kashiyama, K., & Coughlin, E. R. (2018). Mass ejection in failed supernovae: variation with stellar progenitor. *Monthly Notices of the Royal Astronomical Society*, 476(2), 2366–2383.
- Fishbach, M., Holz, D. E., & Farr, B. (2017). Are ligo's black holes made from smaller black holes? *The Astrophysical Journal Letters*, 840(2), L24.
- Fragione, G., Loeb, A., & Rasio, F. A. (2020). On the origin of gw190521-like events from repeated black hole mergers in star clusters. *The Astrophysical Journal Letters*, 902(1), L26.
- Fraley, G. S. (1968). Supernovae explosions induced by pair-production instability. *Astrophysics and Space Science*, 2(1), 96–114.
- Fuller, G., Fowler, W., & Newman, M. (1985). Stellar weak interaction rates for intermediate-mass nuclei. iv-interpolation procedures for rapidly varying lepton capture rates using effective log (ft)-values. *Astrophysical Journal, Part 1 (ISSN 0004-637X)*, vol. 293, June 1, 1985, p. 1-16., 293, 1–16.
- Gaburov, E., Bédorf, J., & Zwart, S. P. (2010). Gravitational tree-code on graphics processing units: implementation in cuda. *Procedia Computer Science*, 1(1), 1119–1127.
- Gaburov, E., Lombardi, J. C., & Zwart, S. P. (2010). On the onset of runaway stellar collisions in dense star clusters–ii. hydrodynamics of three-body interactions. *Monthly Notices of the Royal Astronomical Society*, 402(1), 105–126.
- Gaburov, E., Lombardi Jr, J. C., & Portegies Zwart, S. (2008). Mixing in massive stellar mergers. *Monthly Notices of the Royal Astronomical Society: Letters*, 383(1), L5–L9.
- Gerosa, D., & Berti, E. (2017). Are merging black holes born from stellar collapse or previous mergers? *Physical Review D*, 95(12), 124046.
- Gingold, R. A., & Monaghan, J. J. (1977). Smoothed particle hydrodynamics: theory and application to non-spherical stars. *Monthly notices of the royal astronomical society*, 181(3), 375–389.
- Girardi, L., Bressan, A., Bertelli, G., & Chiosi, C. (2000). Evolutionary tracks and isochrones for low-and intermediate-mass stars: From 0.15 to 7, and from to 0.03. *Astronomy and Astrophysics Supplement Series*, 141(3), 371–383.
- Glebbeek, E., Gaburov, E., Portegies Zwart, S., & Pols, O. R. (2013). Structure and evolution of high-mass stellar mergers. *Monthly Notices of the Royal Astronomical Society*, 434(4), 3497–3510.
- Glebbeek, E., & Pols, O. R. (2008). Evolution of stellar collision products in open clusters-ii. a grid of low-mass collisions. *Astronomy & Astrophysics*, 488(3), 1017–1025.

- Graboske, H., Dewitt, H. d., Grossman, A., & Cooper, M. (1973). Screening factors for nuclear reactions. ii. intermediate screening and astrophysical applications. *Astrophysical Journal, Vol. 181, pp. 457-474 (1973)*, 181, 457–474.
- Haft, M., Raffelt, G., & Weiss, A. (1993). Standard and non-standard plasma neutrino emission revisited. *arXiv preprint astro-ph/9309014*.
- Heger, A., Langer, N., & Woosley, S. (2000). Presupernova evolution of rotating massive stars. i. numerical method and evolution of the internal stellar structure. *The Astrophysical Journal, 528(1)*, 368.
- Heger, A., & Woosley, S. E. (2002). The nucleosynthetic signature of population iii. *The Astrophysical Journal, 567(1)*, 532.
- Henyey, L., Vardya, M., & Bodenheimer, P. (1965). Studies in stellar evolution. iii. the calculation of model envelopes. *The Astrophysical Journal, 142(3)*, 841–854.
- Hernquist, L., & Katz, N. (1989). Treesph-a unification of sph with the hierarchical tree method. *Astrophysical Journal Supplement Series (ISSN 0067-0049), vol. 70, June 1989, p. 419-446. Research supported by the San Diego Supercomputer Center, Pittsburgh Supercomputer Center, and New Jersey High Technology Grant., 70*, 419–446.
- Herwig, F. (2000). The evolution of agb stars with convective overshoot. *arXiv preprint astro-ph/0007139*.
- Hubbard, W. B., & Lampe, M. (1969). Thermal conduction by electrons in stellar matter. *The Astrophysical Journal Supplement Series, 18*, 297.
- Iben Jr, I. (1975). Thermal pulses; p-capture, alpha-capture, s-process nucleosynthesis; and convective mixing in a star of intermediate mass. *Astrophysical Journal, vol. 196, Mar. 1, 1975, pt. 1, p. 525-547.*, 196, 525–547.
- Iben Jr, I., & MacDonald, J. (1985). The effects of diffusion due to gravity and due to composition gradients on the rate of hydrogen burning in a cooling degenerate dwarf. i-the case of a thick helium buffer layer. *The Astrophysical Journal, 296*, 540–553.
- Iglesias, C. A., & Rogers, F. J. (1996). Updated opal opacities. *Astrophysical Journal v. 464, p. 943, 464*, 943.
- Itoh, N., Hayashi, H., Nishikawa, A., & Kohyama, Y. (1996). Neutrino energy loss in stellar interiors. vii. pair, photo-, plasma, bremsstrahlung, and recombination neutrino processes. *Astrophysical Journal Supplement v. 102, p. 411, 102*, 411.
- Itoh, N., & Kohyama, Y. (1983). Neutrino-pair bremsstrahlung in dense stars. i-liquid metal case. *Astrophysical Journal, Part 1 (ISSN 0004-637X), vol. 275, Dec. 15, 1983, p. 858-866. Sponsorship: Ministry of Education., 275*, 858–866.
- Itoh, N., Totsuji, H., Ichimaru, S., & Dewitt, H. (1979). Enhancement of thermonuclear reaction rate due to strong screening. ii-ionic mixtures. *Astrophysical Journal, Part 1, vol. 234, Dec.*

- 15, 1979, p. 1079-1084., 234, 1079–1084.
- Itoh, N., Uchida, S., Sakamoto, Y., Kohyama, Y., & Nozawa, S. (2008). The second born corrections to the electrical and thermal conductivities of dense matter in the liquid metal phase. *The Astrophysical Journal*, 677(1), 495.
- Jermyn, A. S., Bauer, E. B., Schwab, J., Farmer, R., Ball, W. H., Bellinger, E. P., ... others (2023). Modules for experiments in stellar astrophysics (mesa): Time-dependent convection, energy conservation, automatic differentiation, and infrastructure. *The Astrophysical Journal Supplement Series*, 265(1), 15.
- Jiang, Y.-F., Cantiello, M., Bildsten, L., Quataert, E., Blaes, O., & Stone, J. (2018). Outbursts of luminous blue variable stars from variations in the helium opacity. *Nature*, 561(7724), 498–501.
- Justham, S., Podsiadlowski, P., & Vink, J. S. (2014). Luminous blue variables and superluminous supernovae from binary mergers. *The Astrophysical Journal*, 796(2), 121.
- Kremer, K., Spera, M., Becker, D., Chatterjee, S., Di Carlo, U. N., Fragione, G., ... Rasio, F. A. (2020). Populating the upper black hole mass gap through stellar collisions in young star clusters. *The Astrophysical Journal*, 903(1), 45.
- Langanke, K., & Martinez-Pinedo, G. (2000). Shell-model calculations of stellar weak interaction rates: II. weak rates for nuclei in the mass range  $a=45\text{--}65$  in supernovae environments. *Nuclear Physics A*, 673(1-4), 481–508.
- Langer, N. (1998). Coupled mass and angular momentum loss of massive main sequence stars. *Astronomy and Astrophysics*, 329, 551–558.
- Ledoux, P. (1947). Stellar models with convection and with discontinuity of the mean molecular weight. *Astrophysical Journal*, 105.
- Leung, S.-C., Nomoto, K., & Blinnikov, S. (2019). Pulsational pair-instability supernovae. I. pre-collapse evolution and pulsational mass ejection. *The Astrophysical Journal*, 887(1), 72.
- Lombardi, J. C., Rasio, F. A., & Shapiro, S. L. (1995). Collisions of main-sequence stars and the formation of blue stragglers in globular clusters. *arXiv preprint astro-ph/9511074*.
- Lombardi, J. C., Thrall, A. P., Deneva, J. S., Fleming, S. W., & Grabowski, P. E. (2003). Modelling collision products of triple-star mergers. *Monthly Notices of the Royal Astronomical Society*, 345(3), 762–780.
- Lombardi Jr, J., Proulx, Z., Dooley, K., Theriault, E., Ivanova, N., & Rasio, F. (2006). Stellar collisions and ultracompact x-ray binary formation. *The Astrophysical Journal*, 640(1), 441.
- Lombardi Jr, J. C., Sills, A., Rasio, F. A., & Shapiro, S. L. (1999). Tests of spurious transport in smoothed particle hydrodynamics. *Journal of Computational Physics*, 152(2), 687–735.

- Lombardi Jr, J. C., Warren, J. S., Rasio, F. A., Sills, A., & Warren, A. R. (2002). Stellar collisions and the interior structure of blue stragglers. *The Astrophysical Journal*, 568(2), 939.
- Lovegrove, E., & Woosley, S. E. (2013). Very low energy supernovae from neutrino mass loss. *The Astrophysical Journal*, 769(2), 109.
- Lucy, L. B. (1977). A numerical approach to the testing of the fission hypothesis. *Astronomical Journal*, vol. 82, Dec. 1977, p. 1013-1024., 82, 1013–1024.
- Maeder, A. (1975). Stellar evolution. iii-the overshooting from convective cores. *Astronomy and Astrophysics*, vol. 40, no. 3, May 1975, p. 303-310., 40, 303–310.
- Maeder, A., & Meynet, G. (2000). The evolution of rotating stars. *Annual Review of Astronomy and Astrophysics*, 38(1), 143–190.
- Mapelli, M., Bouffanais, Y., Santoliquido, F., Arca Sedda, M., & Artale, M. C. (2022). The cosmic evolution of binary black holes in young, globular, and nuclear star clusters: rates, masses, spins, and mixing fractions. *Monthly Notices of the Royal Astronomical Society*, 511(4), 5797–5816.
- Mapelli, M., Dall'Amico, M., Bouffanais, Y., Giacobbo, N., Arca Sedda, M., Artale, M. C., ... others (2021). Hierarchical black hole mergers in young, globular and nuclear star clusters: the effect of metallicity, spin and cluster properties. *Monthly Notices of the Royal Astronomical Society*, 505(1), 339–358.
- Marchant, P., & Moriya, T. J. (2020). The impact of stellar rotation on the black hole mass-gap from pair-instability supernovae. *Astronomy & Astrophysics*, 640, L18.
- Marchant, P., Renzo, M., Farmer, R., Pappas, K. M., Taam, R. E., De Mink, S. E., & Kalogera, V. (2019). Pulsational pair-instability supernovae in very close binaries. *The Astrophysical Journal*, 882(1), 36.
- Marigo, P., & Aringer, B. (2009). Low-temperature gas opacity-æsopus: a versatile and quick computational tool. *Astronomy & Astrophysics*, 508(3), 1539–1569.
- Marigo, P., Girardi, L., Chiosi, C., & Wood, P. R. (2001). Zero-metallicity stars-i. evolution at constant mass. *Astronomy & Astrophysics*, 371(1), 152–173.
- Mauron, N., & Josselin, E. (2011). The mass-loss rates of red supergiants and the de jager prescription. *Astronomy & Astrophysics*, 526, A156.
- McKernan, B., Ford, K., Lyra, W., & Perets, H. (2012). Intermediate mass black holes in agn discs-i. production and growth. *Monthly Notices of the Royal Astronomical Society*, 425(1), 460–469.
- McKernan, B., Ford, K. S., Bellovary, J., Leigh, N., Haiman, Z., Kocsis, B., ... others (2018). Constraining stellar-mass black hole mergers in agn disks detectable with ligo. *The Astrophysical Journal*, 866(1), 66.

- Mehta, A. K., Buonanno, A., Gair, J., Miller, M. C., Farag, E., DeBoer, R., ... Timmes, F. (2022). Observing intermediate-mass black holes and the upper stellar-mass gap with ligo and virgo. *The Astrophysical Journal*, 924(1), 39.
- Monaghan, J. J. (1992). Smoothed particle hydrodynamics. *Annual review of astronomy and astrophysics*, 30(1), 543–574.
- Monaghan, J. J. (1997). Sph and riemann solvers. *Journal of Computational Physics*, 136(2), 298–307.
- Monaghan, J. J. (2002). Sph compressible turbulence. *Monthly Notices of the Royal Astronomical Society*, 335(3), 843–852.
- Monaghan, J. J. (2005). Smoothed particle hydrodynamics. *Reports on progress in physics*, 68(8), 1703.
- Monaghan, J. J., & Lattanzio, J. C. (1985). A refined particle method for astrophysical problems. *Astronomy and Astrophysics (ISSN 0004-6361)*, vol. 149, no. 1, Aug. 1985, p. 135-143., 149, 135–143.
- Munakata, H., Kohyama, Y., & Itoh, N. (1985). Neutrino energy loss in stellar interiors. *Astrophysical Journal, Part 1 (ISSN 0004-637X)*, vol. 296, Sept. 1, 1985, p. 197-203., 296, 197–203.
- Nadezhin, D. (1980). Ap&ss, 69, 115, doi: 10.1007/BF00638971.
- Nitz, A. H., Capano, C. D., Kumar, S., Wang, Y.-F., Kastha, S., Schäfer, M., ... Cabero, M. (2021). 3-ogc: Catalog of gravitational waves from compact-binary mergers. *The Astrophysical Journal*, 922(1), 76.
- Oda, T., Hino, M., Muto, K., Takahara, M., & Sato, K. (1994). Rate tables for the weak processes of sd-shell nuclei in stellar matter. *Atomic Data and Nuclear Data Tables*, 56(2), 231–403.
- Paxton, B., Bildsten, L., Dotter, A., Herwig, F., Lesaffre, P., & Timmes, F. (2010). Modules for experiments in stellar astrophysics (mesa). *The Astrophysical Journal Supplement Series*, 192(1), 3.
- Paxton, B., Cantiello, M., Arras, P., Bildsten, L., Brown, E. F., Dotter, A., ... others (2013). Modules for experiments in stellar astrophysics (mesa): planets, oscillations, rotation, and massive stars. *The Astrophysical Journal Supplement Series*, 208(1), 4.
- Paxton, B., Marchant, P., Schwab, J., Bauer, E. B., Bildsten, L., Cantiello, M., ... others (2015). Modules for experiments in stellar astrophysics (mesa): binaries, pulsations, and explosions. *The Astrophysical Journal Supplement Series*, 220(1), 15.
- Paxton, B., Schwab, J., Bauer, E. B., Bildsten, L., Blinnikov, S., Duffell, P., ... others (2018). Modules for experiments in stellar astrophysics (): Convective boundaries, element diffusion, and massive star explosions. *The Astrophysical Journal Supplement Series*, 234(2), 34.

- Paxton, B., Smolec, R., Schwab, J., Gautschy, A., Bildsten, L., Cantiello, M., ... others (2019). Modules for experiments in stellar astrophysics (mesa): pulsating variable stars, rotation, convective boundaries, and energy conservation. *The Astrophysical Journal Supplement Series*, 243(1), 10.
- Potekhin, A. (2010). Doctor of science thesis (in russian) <http://www.ioffe.ru/astro/dta/palex/disser.pdf> and a. y. potekhin, g. chabrier. *Contrib. Plasma Physics*, 50, 82.
- Rahman, N., Janka, H.-T., Stockinger, G., & Woosley, S. (2022). Pulsational pair-instability supernovae: gravitational collapse, black hole formation, and beyond. *Monthly Notices of the Royal Astronomical Society*, 512(3), 4503–4540.
- Rakavy, G., & Shaviv, G. (1967). Instabilities in highly evolved stellar models. *The Astrophysical Journal*, 148, 803.
- Rasio, F. A. (1991). *Hydrodynamical calculations of stellar interactions*. Cornell University.
- Rastello, S., Mapelli, M., Di Carlo, U. N., Iorio, G., Ballone, A., Giacobbo, N., ... Torniamenti, S. (2021). Dynamics of binary black holes in low-mass young star clusters. *Monthly Notices of the Royal Astronomical Society*, 507(3), 3612–3625.
- Rauscher, T., & Thielemann, F.-K. (2000). Astrophysical reaction rates from statistical model calculations. *arXiv preprint astro-ph/0004059*.
- Renzo, M., Cantiello, M., Metzger, B., & Jiang, Y.-F. (2020). The stellar merger scenario for black holes in the pair-instability gap. *The Astrophysical Journal Letters*, 904(2), L13.
- Rizzuto, F. P., Naab, T., Spurzem, R., Arca-Sedda, M., Giersz, M., Ostriker, J. P., & Banerjee, S. (2022). Black hole mergers in compact star clusters and massive black hole formation beyond the mass gap. *Monthly Notices of the Royal Astronomical Society*, 512(1), 884–898.
- Rizzuto, F. P., Naab, T., Spurzem, R., Giersz, M., Ostriker, J., Stone, N., ... Rampp, M. (2021). Intermediate mass black hole formation in compact young massive star clusters. *Monthly Notices of the Royal Astronomical Society*, 501(4), 5257–5273.
- Rodriguez, C. L., Zevin, M., Amaro-Seoane, P., Chatterjee, S., Kremer, K., Rasio, F. A., & Claire, S. Y. (2019). Black holes: The next generation—repeated mergers in dense star clusters and their gravitational-wave properties. *Physical Review D*, 100(4), 043027.
- Rogers, F., & Nayfonov, A. (2002). Updated and expanded opal equation-of-state tables: implications for helioseismology. *The Astrophysical Journal*, 576(2), 1064.
- Rosswog, S. (2009). Astrophysical smooth particle hydrodynamics. *New Astronomy Reviews*, 53(4-6), 78–104.
- Saumon, D., Chabrier, G., & van Horn, H. M. (1995). An equation of state for low-mass stars and giant planets. *Astrophysical Journal Supplement v. 99, p. 713, 99, 713*.

- Sedda, M. A., Mapelli, M., Benacquista, M., & Spera, M. (2021). Population synthesis of black hole mergers with b-pop: the impact of dynamics, natal spins, and intermediate-mass black holes on the population of gravitational wave sources. *arXiv preprint arXiv:2109.12119*.
- Sedda, M. A., Mapelli, M., Spera, M., Benacquista, M., & Giacobbo, N. (2020). Fingerprints of binary black hole formation channels encoded in the mass and spin of merger remnants. *The Astrophysical Journal*, 894(2), 133.
- Siegel, D. M., Agarwal, A., Barnes, J., Metzger, B. D., Renzo, M., & Villar, V. A. (2022). “super-kilonovae” from massive collapsars as signatures of black hole birth in the pair-instability mass gap. *The Astrophysical Journal*, 941(1), 100.
- Sills, A., Faber, J. A., Lombardi Jr, J. C., Rasio, F. A., & Warren, A. R. (2001). Evolution of stellar collision products in globular clusters. ii. off-axis collisions. *The Astrophysical Journal*, 548(1), 323.
- Spera, M., & Mapelli, M. (2017). Very massive stars, pair-instability supernovae and intermediate-mass black holes with the sevn code. *Monthly Notices of the Royal Astronomical Society*, 470(4), 4739–4749.
- Spera, M., Mapelli, M., Giacobbo, N., Trani, A. A., Bressan, A., & Costa, G. (2019). Merging black hole binaries with the sevn code. *Monthly Notices of the Royal Astronomical Society*, 485(1), 889–907.
- Springel, V. (2005). The cosmological simulation code gadget-2. *Monthly notices of the royal astronomical society*, 364(4), 1105–1134.
- Stevenson, S., Sampson, M., Powell, J., Vigna-Gómez, A., Neijssel, C. J., Szécsi, D., & Mandel, I. (2019). The impact of pair-instability mass loss on the binary black hole mass distribution. *The Astrophysical Journal*, 882(2), 121.
- Stone, N. C., Metzger, B. D., & Haiman, Z. (2017). Assisted inspirals of stellar mass black holes embedded in agn discs: solving the ‘final au problem’. *Monthly Notices of the Royal Astronomical Society*, 464(1), 946–954.
- Strittmatter, P. (n.d.). Schwarzschild, m.(1958). structure and evolution of the stars. princeton: Princeton university press. slettebak, a.(1976). in be and shell stars, iau symp. no. a. slettebak, pp. 123-36. dordrecht: D. reidel. smith, rc (1971a). mon. not. r. astr. soc, 151, 463-83.
- Tagawa, H., Haiman, Z., & Kocsis, B. (2020). Formation and evolution of compact-object binaries in agn disks. *The Astrophysical Journal*, 898(1), 25.
- Tagawa, H., Kocsis, B., Haiman, Z., Bartos, I., Omukai, K., & Samsing, J. (2021). Mass-gap mergers in active galactic nuclei. *The Astrophysical Journal*, 908(2), 194.
- Tanikawa, A., Susa, H., Yoshida, T., Trani, A. A., & Kinugawa, T. (2021). Merger rate density of population iii binary black holes below, above, and in the pair-instability mass gap. *The Astrophysical Journal*, 910(1), 30.

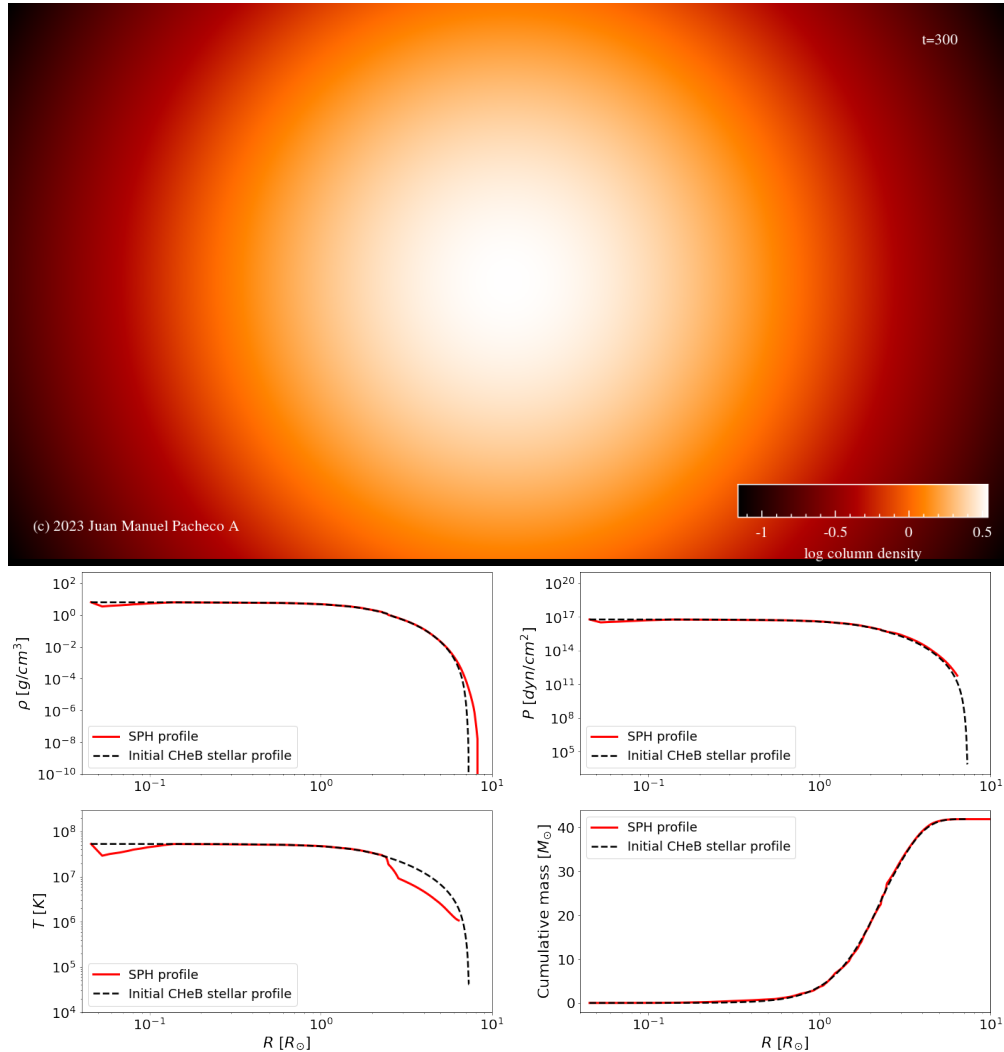
- Thiele, R. (1991). *Stillwell, j., mathematics and its history. berlin. etc., springer-verlag 1989. x, 371 pp., 163 figs., dm 98, 00. isbn 3-540-96981-0 (undergraduate texts in mathematics).* Wiley Online Library.
- Thoul, A. A., Bahcall, J. N., & Loeb, A. (1993). Element diffusion in the solar interior. *arXiv preprint astro-ph/9304005*.
- Timmes, F., & Arnett, D. (1999). The accuracy, consistency, and speed of five equations of state for stellar hydrodynamics. *The Astrophysical Journal Supplement Series*, 125(1), 277.
- Timmes, F. X., & Sweaty, F. D. (2000). The accuracy, consistency, and speed of an electron-positron equation of state based on table interpolation of the helmholtz free energy. *The Astrophysical Journal Supplement Series*, 126(2), 501.
- Vigna-Gómez, A., Justham, S., Mandel, I., De Mink, S. E., & Podsiadlowski, P. (2019). Massive stellar mergers as precursors of hydrogen-rich pulsational pair instability supernovae. *The Astrophysical Journal Letters*, 876(2), L29.
- Vink, J. S., de Koter, A., & Lamers, H. (2001). Mass-loss predictions for o and b stars as a function of metallicity. *Astronomy & Astrophysics*, 369(2), 574–588.
- Vink, J. S., Higgins, E. R., Sander, A. A., & Sabhahit, G. N. (2021). Maximum black hole mass across cosmic time. *Monthly Notices of the Royal Astronomical Society*, 504(1), 146–154.
- VonNeumann, J., & Richtmyer, R. D. (1950). A method for the numerical calculation of hydrodynamic shocks. *Journal of applied physics*, 21(3), 232–237.
- Woosley, S. (2017). Pulsational pair-instability supernovae. *The Astrophysical Journal*, 836(2), 244.
- Woosley, S., & Heger, A. (2021). The pair-instability mass gap for black holes. *The Astrophysical Journal Letters*, 912(2), L31.
- Woosley, S. E., Blinnikov, S., & Heger, A. (2007). Pulsational pair instability as an explanation for the most luminous supernovae. *Nature*, 450(7168), 390–392.
- Yakovlev, D., & Urpin, V. (1980). Thermal and electrical conductivity in white dwarfs and neutron stars. *Soviet Astronomy*, 24, 303.
- Yang, Y., Bartos, I., Haiman, Z., Kocsis, B., Márka, Z., Stone, N., & Márka, S. (2019). Agn disks harden the mass distribution of stellar-mass binary black hole mergers. *The Astrophysical Journal*, 876(2), 122.
- Zhao, X., & Fuller, J. (2020). Centrifugally driven mass-loss and outbursts of massive stars. *Monthly Notices of the Royal Astronomical Society*, 495(1), 249–265.



## Appendix

**Figure 4.1**

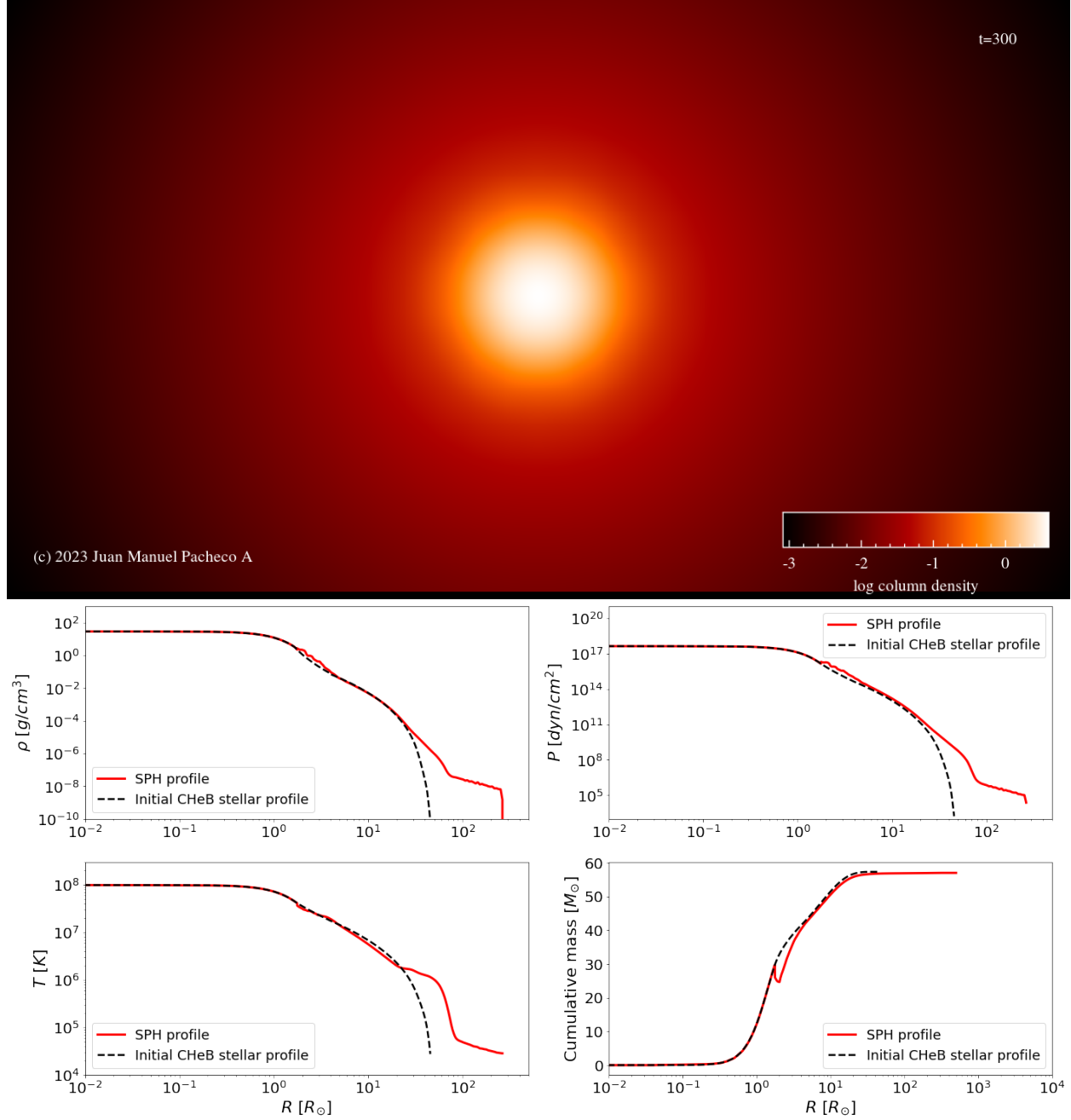
*STARSMASHER relaxation simulation for the MS PARSEC profile of  $42 M_{\odot}$ .*



*Note.* Top panel: 2D logarithmic density map for the last output file (out0300.sph) of the STARSMASHER relaxation routine. The  $x$  and  $y$  axis range from  $-3$  to  $3 R_{\odot}$ , with the densest particle in the simulation as the origin. This image was generated using SPLASH. Middle panel from left to right: density profile in  $g/cm^3$  and pressure profile in  $dyn/cm^2$  along the stellar radius in  $R_{\odot}$ . Bottom panel from left to right: temperature profile in  $K$  and cumulative mass profile in  $M_{\odot}$  along the stellar radius. The red solid lines represents the SPH profile obtained after interpolating the average values obtained in the radial binning of all the particles in the simulation. The dashed black lines represents the input stellar profile MS produced by PARSEC and described in section 2.1.1.

**Figure 4.2**

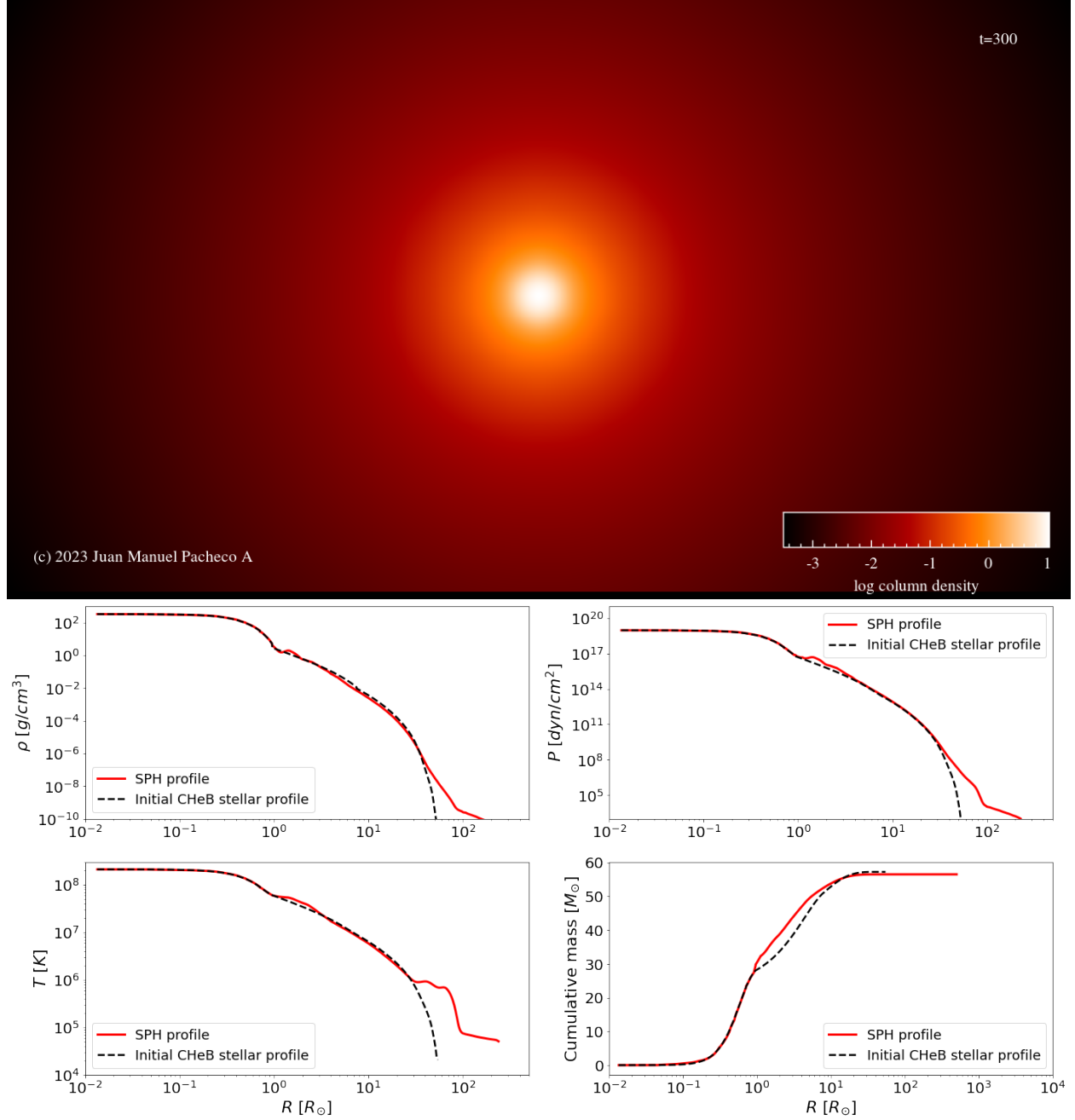
*STARSMASHER relaxation simulation for the TAMS PARSEC profile of  $58 M_{\odot}$ .*



*Note.* Top panel: 2D logarithmic density map for the last output file (`out0300.sph`) of the STARSMASHER relaxation routine. The  $x$  and  $y$  axis range from  $-10$  to  $10 R_{\odot}$ , with the densest particle in the simulation as the origin. This image was generated using SPLASH. Middle panel from left to right: density profile in  $g/cm^3$  and pressure profile in  $dyn/cm^2$  along the stellar radius in  $R_{\odot}$ . Bottom panel from left to right: temperature profile in  $K$  and cumulative mass profile in  $M_{\odot}$  along the stellar radius. The red solid lines represent the SPH profile obtained after interpolating the average values obtained in the radial binning of all the particles in the simulation. The dashed black lines represent the input stellar profile TAMS produced by PARSEC and described in section 2.1.1.

**Figure 4.3**

*STARSMASHER low resolution relaxation simulation for the CHeB PARSEC profile of  $58 M_{\odot}$ .*



*Note.* Top panel: 2D logarithmic density map for the last output file (`out0300.sph`) of the STARSMASHER relaxation routine. The  $x$  and  $y$  axis range from  $-10$  to  $10 R_{\odot}$ , with the densest particle in the simulation as the origin. This image was generated using SPLASH. Middle panel from left to right: density profile in  $g/cm^3$  and pressure profile in  $dyn/cm^2$  along the stellar radius in  $R_{\odot}$ . Bottom panel from left to right: temperature profile in  $K$  and cumulative mass profile in  $M_{\odot}$  along the stellar radius. The red solid lines represents the SPH profile obtained after interpolating the average values obtained in the radial binning of all the particles in the simulation. The dashed black lines represents the input stellar profile CHeB produced by PARSEC and described in section 2.1.1.